2011-07-19

Direct Numerical Simulation of Transonic Wake Flow in the Presence of an Adverse Pressure Gradient and Streamline Curvature

Jeffrey Reed Gibson
Brigham Young University - Provo

BYU ScholarsArchive Citation

Gibson, Jeffrey Reed, "Direct Numerical Simulation of Transonic Wake Flow in the Presence of an Adverse Pressure Gradient and Streamline Curvature" (2011). *All Theses and Dissertations*. 2795.
https://scholarsarchive.byu.edu/etd/2795

Direct Numerical Simulation of Transonic Wake Flow in the Presence of an Adverse Pressure Gradient and Streamline Curvature

Jeffrey R. Gibson

A thesis submitted to the faculty of
Brigham Young University
in partial fulfillment of the requirements for the degree of

Master of Science

Steven E. Gorrell, Chair
R. Daniel Maynes
Julie C. Vanderhoff

Department of Mechanical Engineering

Brigham Young University

December 2011

ABSTRACT

Direct Numerical Simulation of Transonic Wake Flow in the Presence of an Adverse Pressure Gradient and Streamline Curvature

Jeffrey R. Gibson
Department of Mechanical Engineering, BYU
Master of Science

Wakes are present in many engineering flows. These flows include internal flows such as mixing chambers and turbomachinery as well as external flows like flow over high-lift or multi-element airfoils. Many times these wakes are exposed to flow conditions such as adverse pressure gradients and streamline curvature that alter the mean flow and turbulent structure of the wake. The ability to understand how pressure gradients and streamline curvature affects the structure of the wake is essential to predicting how the wake will affect the performance of the application in which it is found. The effects of pressure gradients and curvature of low-speed wakes has been extensively documented. As the transonic flow regime is becoming of more interest as gas speeds in turbomachinery increase this work fills a void in the body of wake knowledge pertaining to curved wakes in high speed flows. An under-resolved direct numerical simulation of transonic wake flow being shed by a cambered airfoil in the presence of adverse pressure gradients and streamline curvature is therefore presented here. It was observed that the turbulence characteristics arising from the cambered airfoil that generates the wake dominate the evolution of the wake for different distances downstream depending on the component of the Reynolds stresses that is being considered. These characteristics dissipated the most quickly in the shear stresses and endured the longest in the tangential normal stresses. Previous work in low-speed wakes has indicated that curvature creates new production terms that translate into asymmetry in the profiles of the wake. Curvature was observed to have limited influence on the evolution of the streamwise normal stresses and an extensive impact on the tangential normal stresses. The transport of the Reynolds shear stresses indicate that the asymmetry in this stress is caused indeed by curvature but through turbulent diffusion and not production. The k-ε turbulence model overpredicted the effect of curvature on the turbulence stresses in the wake. This led to accelerated wake decay and spread compared to the UDNS data.

Keywords: direct numerical simulation, curvature, wakes, cfd, pressure gradients

ACKNOWLEDGMENTS

The achievements in our lives are rarely the product of us alone; but are the concerted effort of us and the good people with whom we surround ourselves. My gratitude then to my sweet wife Melanie for her support and inspiration and to Dr. Steven Gorrell for his mentoring and direct support of this work. The author would also like to acknowledge the support of the Fulton Supercomputing Lab at Brigham Young University and AFRL DSRC for computing resources. Additionally the partial support from the Air Force Office of Scientific Research is gratefully acknowledged.

TABLE OF CONTENTS

LIST OF FIGURES

NOMENCLATURE

$\overline{u}$	Velocity component in the streamwise direction
$\overline{v}$	Velocity component normal to the streamwise direction
$\overline{u'v'}$	Reynolds shear stress
$\frac{1}{2}(\overline{u'^2}+\overline{v'^2})$	Turbulent kinetic energy
ε_1	Tangential vector of the wake centerline path
ε_2	Normal vector of the wake centerline path
c	Chord length of wake generating blade
R	Local radius of streamline curvature
b	Wake width
Supercript	
$'$	Fluctuating component
$^{-}$	Time averaged quantity

CHAPTER 1. INTRODUCTION

1.1 Wake Flow

Wakes are common fluid phenomena that can have a profound impact on engineering processes. A wake is an area which is found downstream of a body that is immersed in a flow. This area is characterized by lower momentum and increased turbulence relative to the freestream. These two conditions are the result of the no slip condition at the fluid-body interface. The structure of a wake is defined through the use of several parameters. These parameters describe the wake width, the magnitude of the momentum defect, and the wake's turbulent nature. Figure 1.1 illustrates three of the more basic wake parameters: the wake width, the wake depth, and the wake centerline. The manner in which the wake parameters vary perpendicular to the streamwise direction is known as the wake profile. Due to the diffusion and convection of momentum, the wake profile's shape and magnitude evolves as the wake propagates downstream. The rate at which the profile changes and the manner in which it changes depend on the nature of the flow through which it propagates.

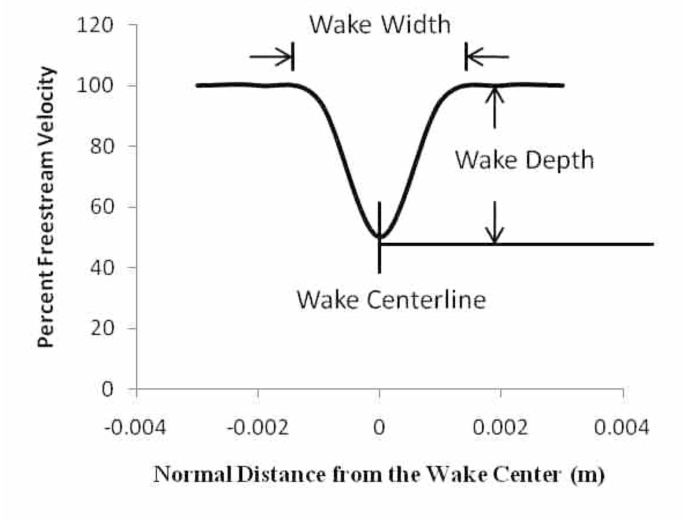

Figure 1.1: Basic Wake Parameters

Wakes are very susceptible to the flow environment in which they propagate. Changes in flow parameters such as pressure gradients and streamline curvature change the structure and profile of the wakes. Pressure gradients can be caused by expansions or contractions in internal flows, diffusion in turbomachinery blading, or where flows approach an immersed body. The effects of pressure gradients on wake structure are generally observed as changes in the rate at which the wake spreads and evolves as it travels downstream. Streamline curvature is caused by a change in the direction of the flow. Under normal flow conditions, wake profiles are symmetric about the wake centerline. When propagating in the presence of streamline curvature however, an asymmetry develops in the profile of the wake parameters.

1.2 Motivation

Wakes can have a great impact on the flow downstream of its origin and therefore influence a variety of engineering processes. For an example, they can affect heat transfer in mixing chambers by altering the turbulence field. Wakes also interact with the boundary layers on turbomachinery blading downstream as well as interact with shock waves and other phenomena found in turbomachinery flow fields; leading to an altered stress field on those downstream blades. This change in drag directly affects the efficiency of the component. Additionally, the lift created by high-lift multi-element airfoils is limited by adverse pressure gradients in the wake. As wakes can have a great effect on these processes it is essential to be able to model what these effects will be. In order to accurately predict the effects that wakes have on these processes, the manner in which pressure gradients and curvature change the wake profile needs be understood.

Extensive work has been conducted regarding the effects of adverse pressure gradients and streamline curvature on low speed wakes and their propagation [1, 2, 4, 5]. Several studies documented the the effect of a pressure gradient alone. Others documented well the results of the combination of the two parameters. One study identified the individual effects of each separate condition as well as that of the combination of the two. In regards to turbulent quantities, the focus of these previous works were the Reynolds shear stresses.

The influence of curvature and pressure gradients on wakes in compressible flows, specifically in the transonic regime, appear to be unexplored. The transonic regime refers to flows where the freestream Mach number is between 0.8 and 1.2. An understanding of the combination of these parameters will improve predictions of key design parameters, like Reynolds stress fields, in high speed flows such as those found in turbomachinery. A Direct Numerical Simulation (DNS) was created to provide time averaged and unsteady data for analysis. Such a simulation will provide the resolution required for an accurate portrayal of the wake development. The numerical simulation will study wakes which are shed from an airfoil and then pass through a blade passage bounded tangentially by two other airfoils.

Turbulence models, especially two-equation models, are commonly used to represent the effects of turbulence in engineering flows. These models are required to close the set of governing equations. This is necessary due to the creation of new correlations that results from the Reynolds averaging of the Navier-Stokes. The accuracy of these models is related to the values of the closure coefficients used in the respective model. By varying the values of these coefficients, a model may be ’tuned’ for specific flows. To evaluate the appropriateness of the behavior the model and the appropriateness of these coefficients, it is necessary to compare data from the turbulence model to a validation data set that is independent of the use of turbulence modeling. A DNS data set serves well as a validation data set for turbulence models. By understanding the limitations or behavior of the turbulence model used, a design engineer can better tune the values of the closure coefficients as well as understand how to interpret the results generated by using a turbulence model.

1.3 Objective

This work focuses on using DNS to create a model of transonic wake flow under the influence of an adverse pressure gradient and streamline curvature. This will fill a void in the existing body of knowledge as to the effects of these flow conditions on high speed, compressible wakes. Data describing the evolution of mean-value and turbulence structure of the wake is analyzed in order to identify how the wake changes when exposed to these flow field phenomena and to identify the driving forces behind that evolution. These results include wake parameters such as velocity defect, wake width, Reynolds Stresses, the Turbulence Kinetic Energy, and the manner in which these parameters change as the flow propagates downstream. The data from the DNS data set is compared to a data set using of the k-ε turbulence model to understand the behavior of this model in predicting transonic curved wake flow. The understanding of the behavior of the turbulence model will indicate what aspect of the model needs modification to improve its performance in modeling turbulence in transonic curved wake flow.

CHAPTER 2. LITERATURE REVIEW

Extensive work has been done to document the effects of pressure gradients and streamline curvature on low speed wakes. The effects of these phenomena were observed in many parameters and characteristics of the wake flow. These characteristics include the rate at which the velocity defect decays, the Reynolds stress distribution, and the turbulent kinetic energy. It has been observed that adverse pressure gradients tend to slow the decay of the wake. Streamline curvature creates an asymmetry in the profiles of the wake parameters.

2.1 The Effects of an Adverse Pressure Gradient on Wake Development

Adverse pressure gradients have been observed to alter the rate at which, for low Mach numbers, wake parameters evolve. Adverse pressure gradients cause the maximum velocity defect to decay less rapidly. John and Schobeiri [1] studied hot-film probe data from a two-dimensional wake being shed off a cylinder. It was noted that the maximum velocity defect decays exponentially as a function of streamwise position. It was concluded that the maximum velocity defect decays more slowly in the presence of an adverse pressure gradient, a power law fit exponent of -0.51, than the nominal pressure case which had an exponent of -0.71. The relationship for the adverse pressure case is shown in Equation 2.1. In that relationship the streamwise distance variable, ε_1 is nondimensionalized with the cylinder diameter and the maximum velocity defect with the potential velocity at the wake center. Using pressure measurements Hill, Schuab, and Senoo [4] observed a two-dimensional wake in the presence of an adverse pressure gradient. If the rate of pressure rise is large enough it was observed that the velocity defect ceases to decay but begins to grow. This can lead to areas of stagnant flow or flow reversal near the centerline of the wake. Flow reversal was also documented by Driver and Mateer [6].

$$\frac{\overline{U}_{lm}}{\overline{U}_{po}} \sim \frac{\varepsilon_1}{d}^{-0.51} \tag{2.1}$$

The rate at which the wake width increases is also affected by the pressure gradient of the flow. John and Schobeiri [1] noted that the wake width grew slightly faster in an adverse pressure gradient than the nominal pressure case. This trend was also observed by Tulapurkara, Ramjee, and George [2] using numerical and experimental data of a wake from a NACA 0012 airfoil.

2.2 The Effects of Streamline Curvature on Wake Development

Curvature is measured in the radius of curvature of the streamlines in the flow. As a flow is turned, a pressure gradient in the direction normal to the flow is created. John and Schobeiri [1] explained how the turbulence in a curved shear flow is suppressed if there is a positive velocity gradient in the positive radial direction. Conversely, a negative velocity gradient in the radial direction increases the level of turbulence. This suppression and enhancement of turbulence results in an asymmetry that is observed in the time averaged velocity profiles as well as the profiles of the turbulence aspects of the wake. The mean velocity defect was observed to not be affected by curvature. Nakayama [5] added that mean vorticity in external wakes was not greatly affected by curvature either, leading to the conclusion that the distortions in the mean vorticity are irrotational.

Through the existing body of work it has been documented that the wake width is consistently larger on the concave side of the wake centerline [1,2,5,7]. The enhanced turbulence on that side of the wake centerline speeds the momentum transfer from the high momentum freestream into the low momentum region of the wake. The rate of momentum transfer is dependent on the magnitudes of the turbulent stresses. The unequal distribution of turbulent stresses translates into a larger wake width on the concave side of the wake.

Previous work has indicated a large asymmetry in the Reynolds stresses, illustrating the sensitivity of these parameters to streamline curvature. The maximum magnitude of the streamwise and tangential turbulence intensities as well as the Reynolds shear stresses were observed through the body of literature to occur on the concave side of the wake [1,2,5,7]. Figure 2.1 shows the shear component of the Reynolds stresses in a curved wake behind a cylinder as analyzed by John and Schobeiri [1]. It was observed that the shear stress was nonzero at the wake centerline when the wake was exposed to curvature. This non-zero centerline value of the shear stress is also supported by the theoretical and experimental work of Schobeiri [7] where it was shown that the shear stress component of the Reynolds stresses must be nonzero at the wake centerline as well as the edges unless the radius of curvature is infinite, which corresponds to straight wake flow. The top half of Figure 2.1 shows the shear stresses before the flow is subjected to curvature. A symmetric profile is observed. The lower half illustrates the results of curvature. The magnitude of the peak on the concave side is more than twice of that on the convex side. These peaks were located at a value of $\varepsilon_2/b = 0.3$ which is the normal distance from the wake centerline normalized by the wake width, b. Nakayama [5] noted that the shear stresses showed the highest degree of asymmetry and therefore are the most sensitive to the effects of curvature. The development of the Reynolds stress profiles illustrated the interdependence of the effects of curvature and pressure gradients. In an adverse pressure gradient the symmetry appeared quickly and dissipated quickly whereas the asymmetry appeared later and was more long lived in the favorable pressure gradient.

John and Schobeiri also considered the evolution of the distribution of the normal components of the Reynolds stresses in the presence of curvature. The streamwise Reynolds stress is shown in Figure 2.2(a) and the tangential normal Reynolds stress in Figure 2.2(b), both are normalized by their respective values located at the wake centerline in order to assess the magnitude of the asymmetry in the stresses. The streamwise component is originally symmetric about the wake centerline with a maximum on each side, as seen in the top half of Figure 2.2(a). As the wake is exposed to streamline curvature the turbulence intensity becomes asymmetric with the peak value occurring near the location of the maximum shear stress on the concave side. The ratio of the peak value to the centerline value is approximately 1.15. Similar behavior is documented in the tangential stresses as well, see Figure 2.2(b). Curvature causes the location of the peak value to shift to the concave side of the wake near the location of maximum shear stress. The ratio of the peak value to the centerline value is 1.20 and is therefore larger than the value of the streamwise stresses.

Nakayama outlined the turbulent structure of fully developed, two-dimensional, incompressible, and turbulent wake subject to curvature. The curvature in this study was categorized as mild as the radius of curvature is significantly larger than the wake width. The consideration of the triple products of the turbulent flow, which represent the transport of Reynolds stresses, demonstrate the rate and the timing at which these stresses evolve in the flow. The onset of asymmetry in the triple products was observed to occur later than the onset in the Reynolds stresses themselves. This asymmetry described the transport of stress from the concave side of the wake trajectory to

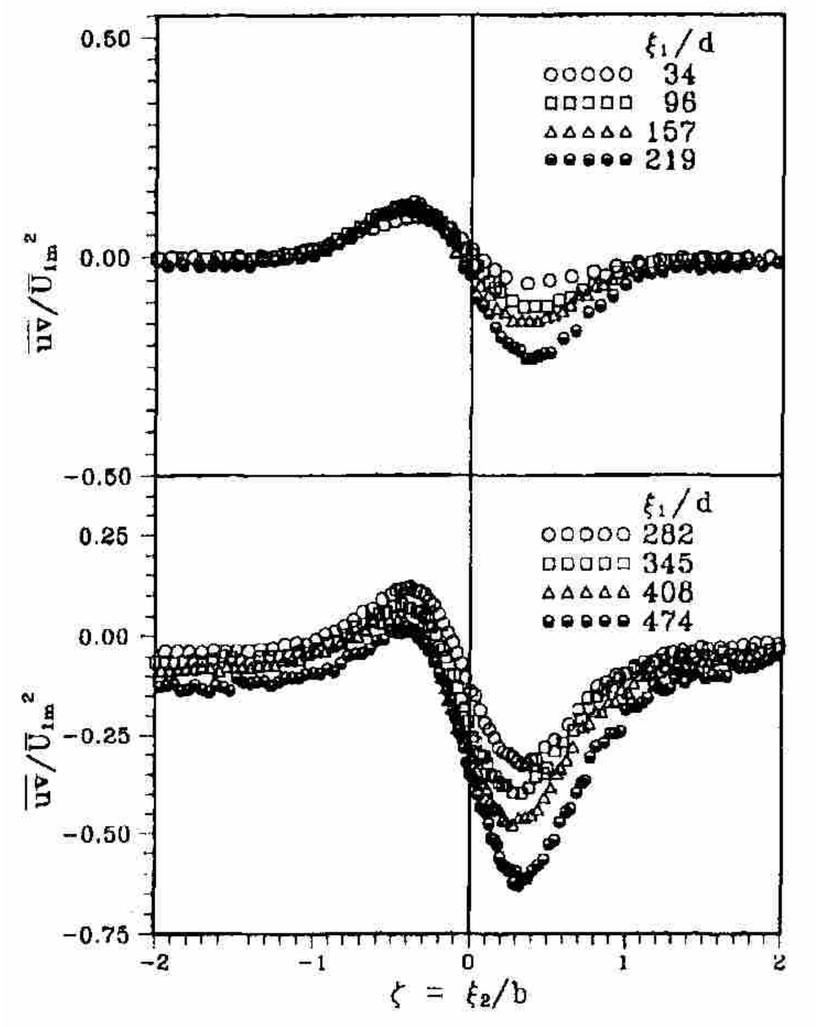

Figure 2.1: Profile of the Reynolds Shear Stresses from John and Schobeiri [1]

the convex side. The triple products continued to show asymmetry at a downstream location where the Reynolds stresses had almost recovered their symmetry. This suggests that the transport of Reynolds stresses continues after the the flow was no longer subjected to curvature.

2.3 Review of Turbulence Modeling and the k-ε Model in Particular

An introduction to turbulence modeling is available in Nichols [8] and Wilcox [9] and is summarized in this section. In order to use numerical methods to directly calculate the effect that turbulence has on a flow, an extremely large number of grid points is required, this will be discussed further in section 3.2 which describes DNS. To avoid this large computational cost, turbulence

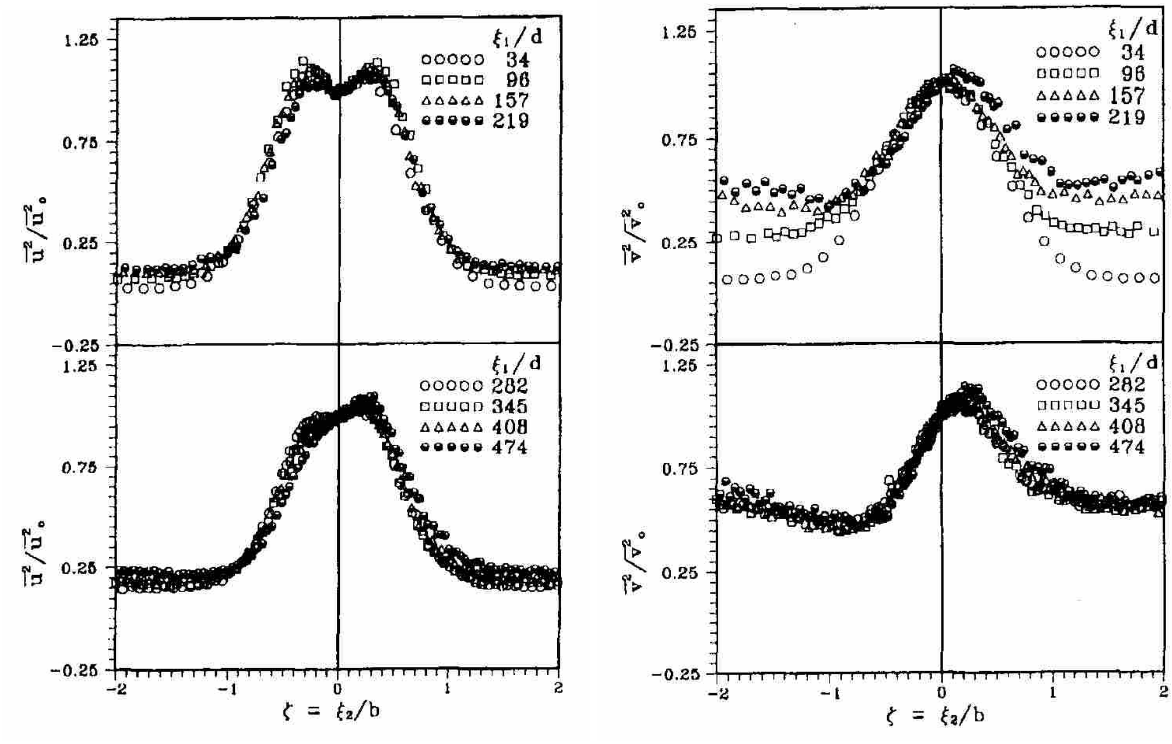

(a)

(b)

Figure 2.2: Profiles of the (a) Streamwise Component and the (b) Tangential Component of the Normal Reynolds Stresses from John and Schobeiri [1]

models have been developed to account for the effects of turbulence while using far fewer grid points. A common way that these models simplify the Navier-Stokes equations is through the use of Reynolds averaging. Through this method the instantaneous velocity value may be expressed as the combination of a mean component and a fluctuating component. This greatly simplifies the Navier-Stokes equation but also introduces a number of new terms, namely the Reynolds Stress tensor, but no new equations. Obtaining values for these new terms or correlations is at the heart of the closure problem in turbulence modeling. The wide spectrum of turbulence models available represent the numerous ways that attempt to solve the closure problem. Some models use algebraic equations that are derived from experimental data sets while some use the transport equations of various flow variables to provide the values for these correlations. This refers to the division of turbulence models known as one-equation and two-equation models (depending on the number of transport equations used). These models rely on the Boussinesq approximation which relates the strain tensor and the Reynolds stress tensor through a parameter called the eddy viscosity.

This concept mirrors the use of viscosity to relate the stress and strain tensors in laminar flow. The output of a turbulence model is the value of eddy viscosity. A formula to calculate the eddy viscosity is required to connect the transport equations and the Boussinesq approximation and is unique for each of the various turbulence models.

The k-ε model is a two equation model that uses the transport equation of turbulence kinetic energy, k, and that of dissipation ε (see Equations 2.2 and 2.3). In Equation 2.2 the terms are identified from left to right: the temporal term, the advection term, the shear production term, the dissipation, and the viscous term. Equation 2.3 shows the terms involved with the transport of dissipation and has similar terms as Equation 2.2. Note that the production and dissipation terms in Equation 2.3 are the product of the production and dissipation terms respectively from Equation 2.2 and empirically determined coefficients and wall damping functions [8]. The coefficients $C_{\varepsilon 1}$, $C_{\varepsilon 2}$, and C_μ in Equation 2.3 are empirically determined coefficients. In the standard k-ε model the value of C_μ is approximately 0.09. In an attempt to tune this turbulence model or specific flows, say turbomachinery flows for example, alternate methods of calculating this coefficient have been developed. The standard k-ε model has been observed to perform well in the boundary layers and areas near the wall while the accuracy decreases in the freestream [9].

$$\frac{\partial k}{\partial t} + U_i \frac{\partial k}{\partial x_j} = -\frac{\partial}{\partial x_j}\left[\overline{u'_i\left(\frac{u'_j\,u'_j}{2}+\frac{p'}{\rho}\right)}\right] - \overline{u'_i u'_j}\frac{\partial U_i}{\partial x_j} - \nu\,\overline{\frac{\partial u'_i}{\partial x_j}\frac{\partial u'_i}{\partial x_j}} \tag{2.2}$$

$$\frac{\partial \varepsilon}{\partial t} + U_i \frac{\partial \varepsilon}{\partial x_i} = \frac{\partial}{\partial x_i}\left[\left(\nu + \frac{\nu_t}{\sigma_\varepsilon}\right)\frac{\partial \varepsilon}{\partial x_i}\right] + C_{\varepsilon 1} f_{\varepsilon 1}\frac{\varepsilon}{k}P_k - C_{\varepsilon 2} f_{\varepsilon 2}\frac{\varepsilon^2}{k} + R \tag{2.3}$$

2.4 Comparison of k-ε and Experimental Wake data in Pressure Gradients and Streamline Curvature

The performance of the k-ε turbulence model in capturing the effects of adverse pressure gradients and streamline curvature on low speed wake has been considered by Tulapurkara, Ramjee, and George [2]. Experimental and numerical data were compared for low speed wake flow (the freestream velocity was approximately 15 m/s) that is exposed to an adverse pressure gradient, streamline curvature, and the combination of the two. C_μ with a constant as well as a variable value were considered. The turbulence model captured the velocity defect decay rate for the case of combined pressure gradient and curvature, but slightly underpredicts the decay rate for the case of streamline curvature alone. The profiles of turbulent kinetic energy (TKE), shown in Figure 2.3, demonstrate this trend. The k-ε model overpredicted the asymmetry in the TKE profiles for the case of combined streamline curvature and pressure gradient.

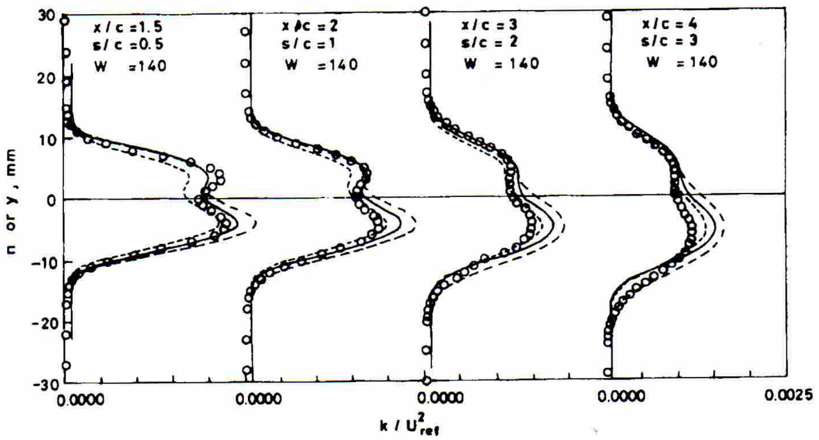

Figure 5(b). Profiles of turbulent kinetic energy, k/U^2_{ref}— Flow B; ○, experiment; ————, prediction with C_μ constant; — — —, prediction with C_μ variable (Leschziner and Rodi); --------, prediction with C_μ variable (Humphrey and Pourahmadi)

Figure 2.3: Profile of Turbulence Kinetic Energy from Tulapurkara, Ramjee, and George [2]

2.5 Wakes Behind Cambered Airfoils

Wakes generated by cambered airfoils differ from those of symmetric bodies in mean value and turbulent structure. Raj and Lakshminarayana [10] studied the low-speed wake behind a cascade of cambered airfoils that experienced an adverse pressure gradient but no streamline curvature. The profiles of mean streamwise velocity were asymmetric with a larger wake width on the suction side of the wake. The profiles of the streamwise and tangential Reynolds stresses showed a single peak at or near the wake center line; indicating that the dominant source of stresses near the wake centerline was the presence of the wake generating airfoil in the flow. The location of this peak was observed to be a function of the thickness to chord length of the airfoil generating the wake. The single peak in the profile is in contrast to the wakes referenced previously where the sources of the Reynolds stresses are either the shear in the flow or the result from streamline curvature. The turbulence resulting from the cambered airfoil diminishes quickly so that by three quarters of a chord length downstream, the turbulence intensities were only 30% of their initial magnitudes.

Zhang and Ligrani [11] studied the transonic wake behind a cambered airfoil without adverse pressure gradient nor streamline curvature. The profiles of the mean velocity defect in similarity variables show an asymmetric profile with a larger width on the suction side. This deviates from similar plots in the incompressible wake studies using symmetric bodies as well as a cambered airfoil, which show a symmetric profile of velocity defect when cast in similarity variables. Zhang and Ligrani also noted that the turbulence intensity was larger behind a cambered airfoil than behind a symmetric airfoil.

CHAPTER 3. METHODOLOGY

3.1 Overview

The methodology used in the current work focuses on creating a numerical, or CFD, model to generate the necessary data to describe the flow through the study geometry. A wide spectrum of flow parameters were analyzed to describe the structure of a transonic wake that is propagating through an adverse pressure gradient and streamline curvature. These parameters include the time-averaged values such as the velocity defect and wake width as well as various turbulent parameters such as the various turbulence intensities, the turbulence kinetic energy, and the Reynolds shear stress were analyzed.

The process of developing a CFD simulation consists of three main efforts: developing the grid, running the simulation, and postprocessing the generated data. The grid development phase is very important as the design of the grid directly affects the results of the simulation. This is especially true in a DNS since it solves the governing equations directly without the use of a turbulence model. A grid with an insufficient number of grid points, either overall or in a specific region of the flow, will reduce the accuracy of the results. The results generated using a well designed grid may still be erroneous if the simulation has not been run long enough. This condition of sufficiently iterated is referred to as being converged. The effort to run the simulation therefore focuses on producing a converged solution. The application of proper convergence criteria to an adequate solver yields such a solution. Once a converged solution is arrived at and a data set is generated, that data set must be postprocessed. Postprocessing is the effort to extract useful and intelligible information from the body of data. This effort is complicated even more when working with a DNS as it produces an enormous amount of data. Postprocessing that quantity of data poses a very large challenge.

Two separate CFD methods were used in the current study. The first is Direct Numerical Simulation (DNS). DNS was selected due to the high accuracy it produces and the fact that those results are independent of experimental validation. Since the DNS is not dependent on experimental validation a proper numerical set-up is necessary to generate useful data. The method of Reynolds-Averaged Navier-Stokes simulation (RANS), employing the k-ε turbulence model, was also used to create a comparison data set. The comparison of the DNS and RANS data sets will contribute to the evaluation of the success of the application of the k-ε turbulence model to transonic wake-flow with pressure gradients and curvature.

3.2 Introduction to Direct Numerical Simulation

This section will discuss the numerical methods used in this work and the design specifics associated with each method. Numerical modeling refers to the discretization of a set of equations and then solving those equations with the appropriate boundary conditions. The methods of modeling may vary, especially in the context of CFD. A key differential between various modeling methods in CFD is the smallest scales of turbulence that the method resolves. Turbulence scales are the length and time scales that describe the turbulent nature of the flow. The largest scale, or integral scale, is the maximum scale at which the flow features are correlated. The physical parallel to this scale is the size of the largest eddies in the flow. The smallest turbulence scale, the Kolmogorov scale, is the minimum length scale below which fluid motion becomes random; or the size of the smallest eddies in the flow. Through the Taylor hypothesis each length scale is associated with a corresponding time scale through the mean freestream velocity. As shown in Figure 3.1, a fully-resolved DNS does not use a turbulence model and therefore resolves even the smallest, or Kolmogorov, scale of a flow. The RANS method however uses turbulence models to approximate almost the entire range of turbulence scales and resolves only the large flow features.

Direct Numerical Simulation differs from all other CFD methods. This difference lies in the approach taken to solve the governing equations. Other CFD methods such as RANS and even Large Eddy Simulation (LES) do not resolve the smallest scale of the turbulence structures of the flow; but use turbulence models to imitate small-scale turbulence behavior. DNS however, as the name implies, solves the conservation of mass, momentum, and energy equations directly, and therefore resolves structures as small as the Kolmogorov scale of the flow. This allows for very high accuracy at the expense of computational requirements. DNS results are so accurate they serve many similar roles as experimental results. For example, DNS results can be used to

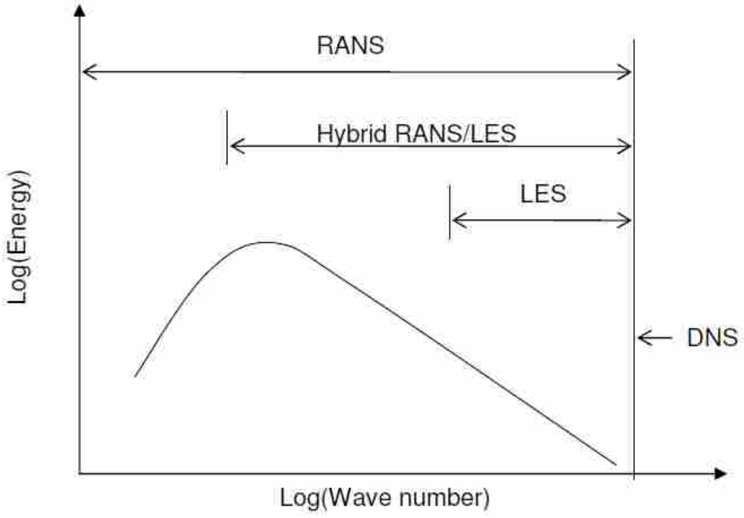

Figure 3.1: The Range of Turbulence Scales That are Modeled by Various Turbulence Models

validate turbulence models in RANS simulations. DNS results are advantageous to experimental results as they are not limited by instrumentation constraints nor are they complicated by the effects which accompany the presence instrumentation in experimental flows. Therefore the cost-benefit relationship associated with DNS makes it useful when the flow domain is relatively small and when sufficient computational resources are available.

3.3 Description of the Numerical Domain

The geometry of the simulation centers on one blade passage of the first two blade rows of the Blade Row Interaction (BRI) rig [12]. The first blade row consists of airfoils with a NACA 0065 thickness distribution. This blade row generates the wake that will be studied as it propagates downstream through the passage between the second blade row. As the flow passes through the second blade row it is turned approximately 28 degrees. The local Mach number in the wake region varied between 0.7 and 0.8 which translates into the lower transonic regime. The Reynolds number, based on the freestream axial velocity and the chord length of the first blade row, is 700,000. The blade geometry is bounded radially by the hub and case surfaces, see Figure 3.2. The grid extends 1.5 chord lengths in front of the leading edge of the first blade row and 1 chord length downstream of the second blade row trailing edge. These extra lengths serve to isolate the flow field in the second blade passage from the effects of the inlet and exit boundary conditions.

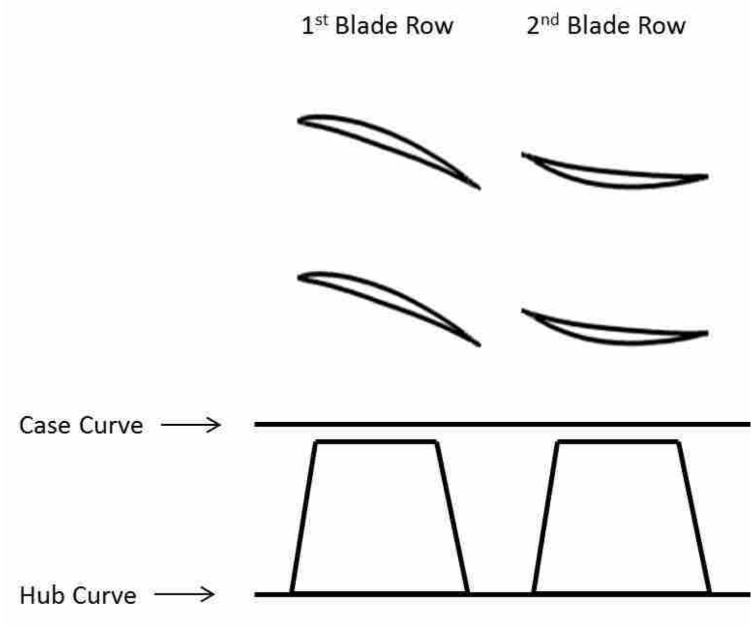

Figure 3.2: Profile and Span Views, at Approximately 50 Percent Span, of the Study Geometry

The boundary conditions, as indicated in Figure 3.3, were designed to simulate one blade passage of the BRI rig. The inlet was designated as an isentropic inlet with defined profiles of inlet total pressure and total temperature. The outlet boundary condition was fixed mass flow rate. The exit mass flow rate was 15.1 kg/s. Periodic conditions were applied to the tangential boundaries except at the blade surfaces. A no slip condition was applied to the hub, case, and blading surfaces. The boundary between each blade row was modeled as a stationary sliding plane. Values are interpolated across this plane based on any offset in the location of the nodes on the edge of the grid of the first and second blade rows. The input values for the DNS and k-ε simulations are found in Appendices A and B.

3.4 Grid Generation for Computational Fluid Dynamics

Turbomachinery Gridding System [13] (TGS) was used to generate the grid for the DNS and the RANS simulation. To the knowledge of the author the current study was one the first applications of TGS to generating DNS grids. TGS generates a structured hexahedral grid which is elliptically smoothed in the blade to blade plane. The smoothing process provides better definition for the leading and trailing edges of the blade. This also eliminates the high aspect ratio cells which

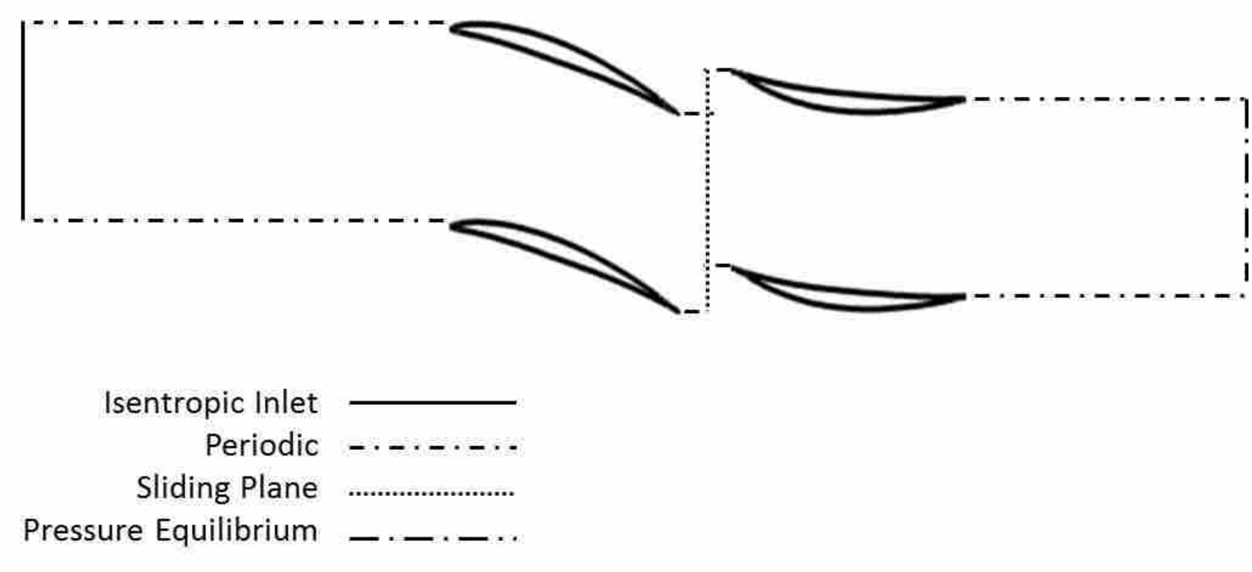

Figure 3.3: Boundary Conditions Depicted with Geometry at Approximately Mid-Span

normally accompany hexahedral or ”H” grids. TGS was selected due to previous experience with this program and its disposition to control grid parameters in the context of turbomachinery flows.

The grid of a CFD simulation refers to the distribution of grid points throughout the flow domain. Each node represents a spatial location at which the governing equations are solved. A well designed grid is essential for an accurate CFD simulation. The design of a grid consists of the number and location of those nodes. A sufficient overall node density throughout the flow domain is required for accurate results. Node distribution in the flow domain is far from uniform. Areas of the flow domain where large gradients in the flow parameters are expected require a greater node density than the freestream region. There are several guidelines that are used to produce a quality grid. One is that the nodes should be equally spaced in relationship to their neighbors. This is referred to as the aspect ratio of the cells. The cell is the three dimensional volume defined the eight bordering nodes. The ratio of the distances between a node and each of its neighbors should not exceed two.

3.5 Numerical Set-up of the DNS

A fully-resolved DNS utilizes a grid and time step that is fine enough to resolve the smallest structures in the flow. As a result, the computational cost is extremely high. In response to this high cost, grids that are too coarse to fully resolve the flow structures have been used with good results. This method is known in the literature and referred to in this work as Under-resolved Direct Numerical Simulation. A grid following this method was developed for the current work. Several parameters were used to evaluate how close to a fully-resolved DNS this work comes.

3.5.1 Estimate of Grid Parameters Parameters of a Fully-resolved DNS

A preliminary estimate of the overall grid density and temporal resolution of a fully-resolved DNS is established through published relationships. Wilcox provided such relationships for channel flow. [9] These are equations 3.1 and 3.2 and are functions of the friction velocity and provide a lower limit for the node density, N_{DNS}, to be sufficient to resolve Kolmogorov scale structures. The value of the friction Reynolds number, Re_τ, from both sides of the first blade row is 20,000. The value for the friction velocity, u_τ, that was used was generated by the RANS simulation as a time-average DNS velocity field was not calculated. As these correlations are for straight channel flow, the length scale used is the channel width H. The Wilcox relationship establishes 7.5 billion nodes per blade row as sufficient to perform a fully resolved DNS. Equation 3.2 indicates a time step of 0.15 micro-seconds. These calculations illustrate the computational cost which has limited the application of DNS to small scale flows or flows with low Reynolds numbers. They provide a lower bounds for a fully resolved DNS for the geometry being studied. The Wilcox relationships provide a lower estimate of the required grid density because channel flow lacks the pressure gradients and curvature that are found in turbomachinery blading. Due to the effects of these phenomena on the flow field, an even higher grid density would be required to resolve the small scale structures in the current flow.

$$\mathrm{N_{DNS}} = (3Re_\tau)^{\frac{9}{4}} \quad \text{where} \quad Re_\tau = \frac{u_\tau H}{2\nu} \quad u_\tau = \sqrt{\nu \frac{\delta u}{\delta y}|_{wall}} \tag{3.1}$$

$$\Delta t \approx \frac{0.003}{\sqrt{Re_\tau}} \frac{H}{u_\tau} \tag{3.2}$$

3.5.2 Under-resolved DNS

In light of the extreme computational cost of a fully-resolved DNS, effort has been invested into exploring the use of DNS methods while utilizing grids that are too coarse to be considered a fully-resolved DNS. This method has been called in the literature and in the current work under-resolved DNS (UDNS). Gross and Fasel [3] investigated the use of UDNS to model flow through a low-pressure turbine at a Reynolds number, based on chord length, of 25,000. The grid used 2,800,000 grid points. The resulting data showed that the distribution of wall pressure coefficient, see Figure 3.4, and freestream turbulence kinetic intensity agreed well with experimental data. Using the ratio of the Kolmogorov length scale of the flow, η, and the spatial resolution of the grid, Δx, it was determined that this grid was roughly 80 times too coarse to resolve the Kolmogorov scale in the wake regions of the flow. Despite being so coarse, it was observed that increases in the grid density yielded diminishing improvements in capturing the wake profile. Building on the work of Gross and Fasel, other researchers have further refined this grid to model various phenomena in low-pressure turbines [14, 15]. Kalitzin, Durbin, and Wu [16] produced good results of low-pressure turbine flow at Reynolds number of 148,000 using a grid of 85,800,000 grid points (1153 axial x 577 tangential x 129 radial). This is significant as the Reynolds number is the same order of magnitude as that of the current study. Zaki [17] used a grid of 84,700,000 grid points (1025 axial x 641 tangential x 129 radial) to simulate flow over compressor stator blade geometry at a Reynolds number of 139,000. These studies were used as benchmarks to establish the minimum requirements for the grid resolution of a successful UDNS; both for the overall number of nodes as well as the ratio of grid resolution and the Kolmogorov length scale of the flow.

3.5.3 Parameters for the Under-resolved DNS

The grid for the UDNS was constructed using the experience gained in the studies referenced above. The grids for the first and second blade rows contain 1226 x 651 x 201 and 1651 x 801 x 201 axial, tangential, and radial grid points respectively. This yields a total number of approximately 450,000,000 nodes. The number of nodes per blade row is three time higher than the benchmark created using UDNS studies of similar geometry and Reynolds numbers of similar orders of magnitude. The number of nodes in the radial direction was consistently lower by a sig-

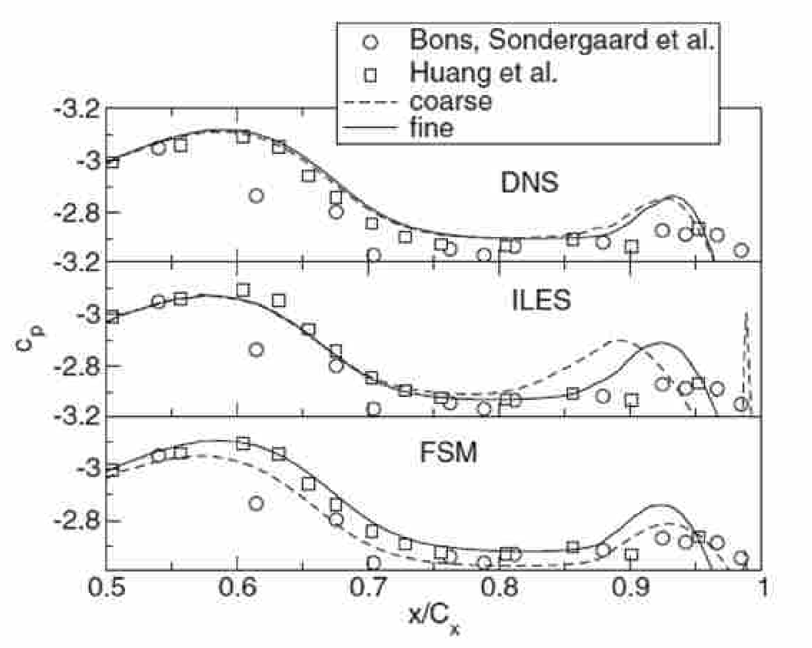

Figure 3.4: Comparison of Wall Pressure Coefficient for UDNS grids and Experimental Data [3]

nificant amount than the number of points in the axial or tangential directions. This is consistent with the existing body of work using UDNS. The increased resolution in the second blade passage was included to better resolve the wake structure as it evolved. The y^+ values for the nearest node to the wall was approximately less than 1. The grid, every tenth node shown, at approximately mid-span is shown in Figure 3.5. This grid was partitioned among 2130 processors to run the simulation.

The temporal resolution of 1,698 time steps per wake passing period was selected as it corresponds to a CFL number of approximately unity. A wake passing period is defined by the time it takes the wake to travel the chord length of the second blade row. The CFL number relates the temporal resolution and the spatial resolution through the freestream velocity as seen in Equation 3.3. The spatial resolution used was an average value, in the axial direction, taken from the area surrounding the trailing edge of the second blade row. This is an area of higher grid density and therefore provides a conservative estimate of the required temporal resolution in relation to other areas in the domain. The freestream velocity used was a blade to blade average of the axial velocity component.

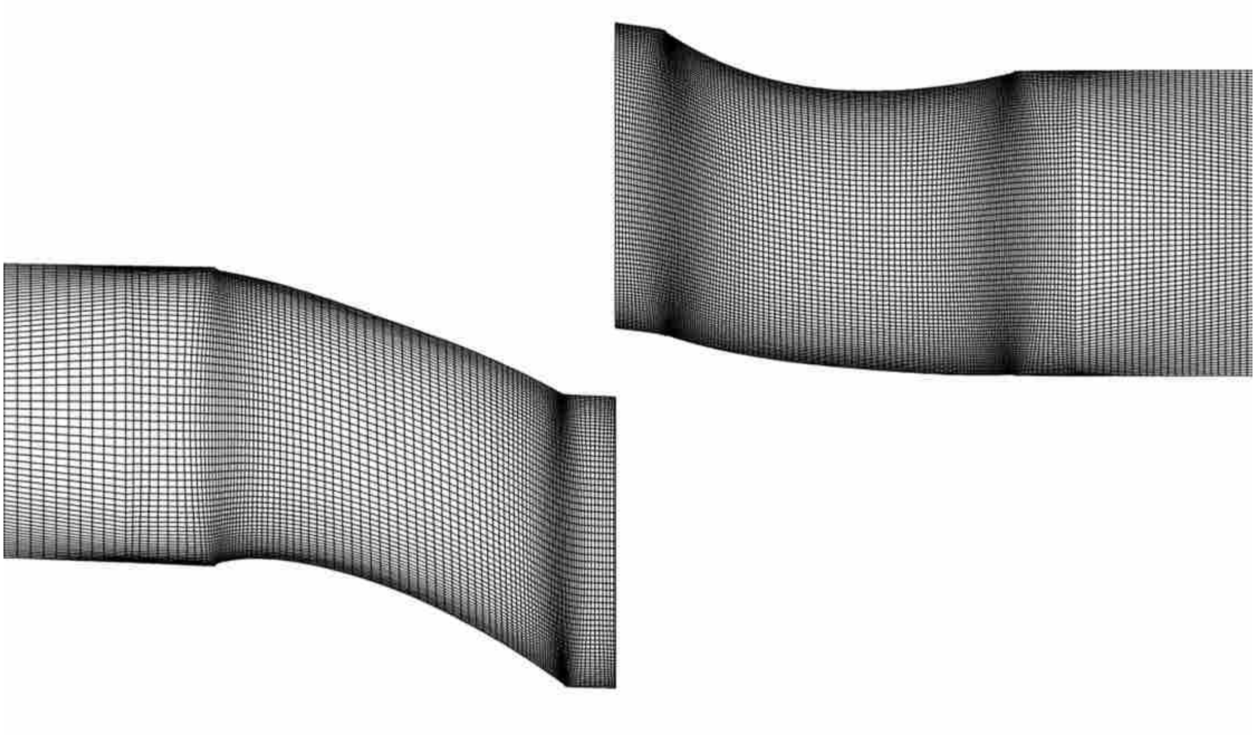

Figure 3.5: UDNS Grid Centered on the Blade Rows (Every Tenth Node Shown) at Approximately Midspan

3.5.4 Numerical Solver Used

The parallel flow solver TURBO [18] was used to solve the unsteady conservation equations using third order spatial accuracy and second order temporal accuracy. The solution algorithm is an iterative implicit time-accurate scheme with a finite-volume spatial discretization. A high order, upwind Roe scheme is employed for spatial discretization with Newton subiterations to converge the solution at every time step. With this upwind scheme there is no addition of artificial dissipation. A third-order min-mod flux limiter was used to limit any excessive oscillations in the momentum terms. An enhanced no slip condition was generated using a flux fix. This combination of solver options has been documented to be optimal for a UDNS application of PTURBO [19].

$$\mathrm{C} = \frac{U\Delta t}{\Delta x} \tag{3.3}$$

3.5.5 Evaluation of the Under-resolved DNS

It is important to gauge how close the Under-resolved Direct Numerical Simulation is to being fully-resolved. This may be achieved using a few different methods. The first method used was to analyze the grid of the UDNS by comparing the grid resolution, Δx, to the Kolmogorov length scale, η. The quality of the UDNS in the wake area is of particular interest so both parameters, Δx and η, were calculated at the nodes where the wake data was analyzed. The method used to calculate the Kolmogorov length scale is shown in Equation 3.4. The length scale, L, is the integral length scale calculated by integrating the autocorrelation function of the fluctuating velocities. The turbulent Reynolds number in Equation 3.4 uses the square root of the turbulence kinetic energy. The value of the ratio of axial grid resolution to the Kolmogorov length scale, Δx/η, ranged from six to approximately eighteen. In order to resolve a structure, i.e. Kolmogorov scale eddies, a grid resolution of a fourth of the scale of the structure is required. Subsequently, the UDNS is approximately twenty-five to seventy-two times too coarse to be fully-resolved. This ratio meets or is below the benchmark created using flows through turbomachinery geometries. The combination of the fulfillment of this benchmark and that of the overall node count lend confidence to the sufficiency of the grid.

$$\eta = \frac{L}{Re_t^{\frac{3}{4}}} \quad \text{where} \quad Re_t = \frac{\sqrt{k}L}{\nu} \tag{3.4}$$

The second method used to evaluate the quality of the UDNS is to analyze the power density spectrum of the of the turbulent energy in the wake. Figure 3.6 shows the average power density spectrum from all of the points in the flow where the wake data was analyzed. The power density spectrum shows the distribution of turbulence energy, E, across the various sizes of eddies in a turbulent flow. The horizontal axis of the figure shows the wave number, κ, of the various eddies which is inversely proportional to the size of the eddy. A grid independent DNS displays a roll-off, or rapid decay, in turbulent kinetic energy around the Kolmogorov length scale that has been documented in experimental studies [9]. The general slope of this area is represented by the red line in Figure 3.6 and has value of -7. This value is similar to the values exhibited by a variety of turbulent flows [20]. The second aspect of the power density spectrum that was considered was whether the data follows Kolmogorov's 5/3 law that has been well established in the body of knowledge regarding turbulent flow. This law refers to a region that exists between the energy bearing eddies, low wave number, and the energy dissipative eddies, high wave number, that exhibits a linear slope with a value of -5/3. This law has been so well established that numerical and experimental data are regarded with skepticism if they do not exhibit this behavior [9]. It can be observed that the average power density spectrum follows this law. The power density spectrum levels off at approximately $3x10^5$. This is the limit of the resolution of the grid and thus scales smaller than this are aliased with larger scales.

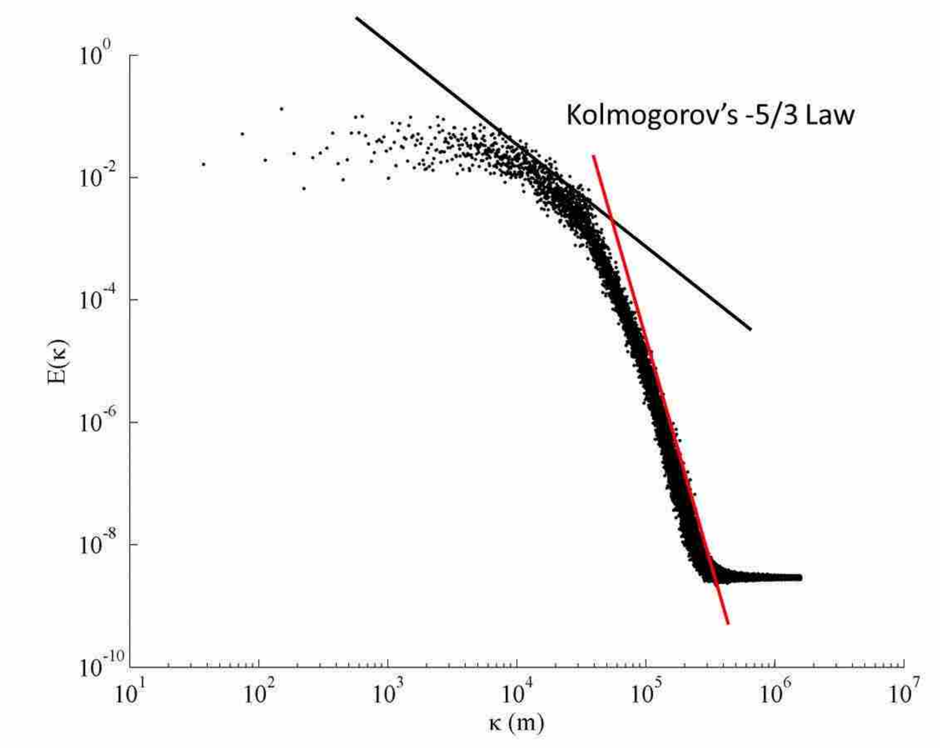

Figure 3.6: Average Power Density Spectrum from the UDNS

Good quality DNS data is observed with similar confidence as experimental data and is used for similar purposes. It is imperative therefore that confidence must be established in the data before it is accepted as accurate. The benchmarking of the UDNS data is an important step in establishing this confidence in the data set. Several parameters and aspects of the UDNS were used in this process. The first two are related to the grid used and are generated using previous experience in conducting UDNS on turbomachinery geometry. First, the overall node count used in this study exceeds those used by studies whose Reynolds number were on the same order of magnitude as the current study. Secondly, the ratio of grid resolution to Kolmogorov length scale in the current study is less than that used by a study that effectively predicted freestream turbulence parameters. Additional confidence was established by considering the spectral analysis of the turbulence calculated by the UDNS. The average power density spectrum follows the form of established classical turbulence in the inertial sub-range (Kolmogorov's -5/3 Law) as well as below the Kolmogorov length scale (established by the slope of -7 in Figure 3.6). The fact that the power density spectrum follows these established forms indicates that the UDNS has properly captured the cascade of turbulent energy from the large scale eddies to the smaller ones. Having established that the UDNS follows gridding benchmarks and properly captures the turbulence cascade, the results of the UDNS were accepted to be of the quality of experimental data. It is justifiable then that the data is used to analyze the wake structure and serve as a comparison data set for the data generated by the URANS simulation. As the spectral analysis and ratio of grid resolution to Kolmogorov length scale is based on data taken in the wake region, caution should be taken when analyzing data from outside this area.

3.6 Numerical Set-up of the URANS Simulation

The grid and numerical set-up for the Unsteady Reynolds Averaged Navier-Stokes (URANS) simulation have been extensively documented in the work of List [12]. In this work, the grid for the first blade row consists of 263 x 151 x 101 grid points and the second consists of 461 x 201 x 101. The third blade row, the rotor, in List's work was removed for the current study. This yields a total of approximately 13,300,000 nodes. The elimination of the rotor simplifies the flow physics in the domain significantly. As a result, the grid density and distribution in the two remaining blade rows were more than sufficient to resolve the simplified flow of the current work. The grid for the URANS simulation, every third node shown, is found in Figure 3.7. The temporal resolution selected corresponds to 269 time steps per wake passing period. Similar to the UDNS, PTURBO was used as the solver for this simulation with third order spatial accuracy and second order temporal resolution. The URANS grid was partitioned among 64 processors to run the simulation.

PTURBO utilizes a version of the k-ε turbulence model that has been tuned to model turbomachinery flows. As discussed in the introduction to turbulence modeling, the standard k-ε

of Launder and Spalding (1974) uses a constant value of C_μ and does not account for the rotation of coordinate axis on the evolution of turbulence [21]. The CMOTT k-ε model, that which is used by TURBO, uses a variable formulation of C_μ that is dependent on the product of the mean and turbulence time scales. This variable formulation is dependent on the rotation tensor and can therefore modify the eddy viscosity accordingly [21]. The use of wall functions are required due to the high Reynolds number of the flow. These wall functions are applied up to y^+ values of 26.

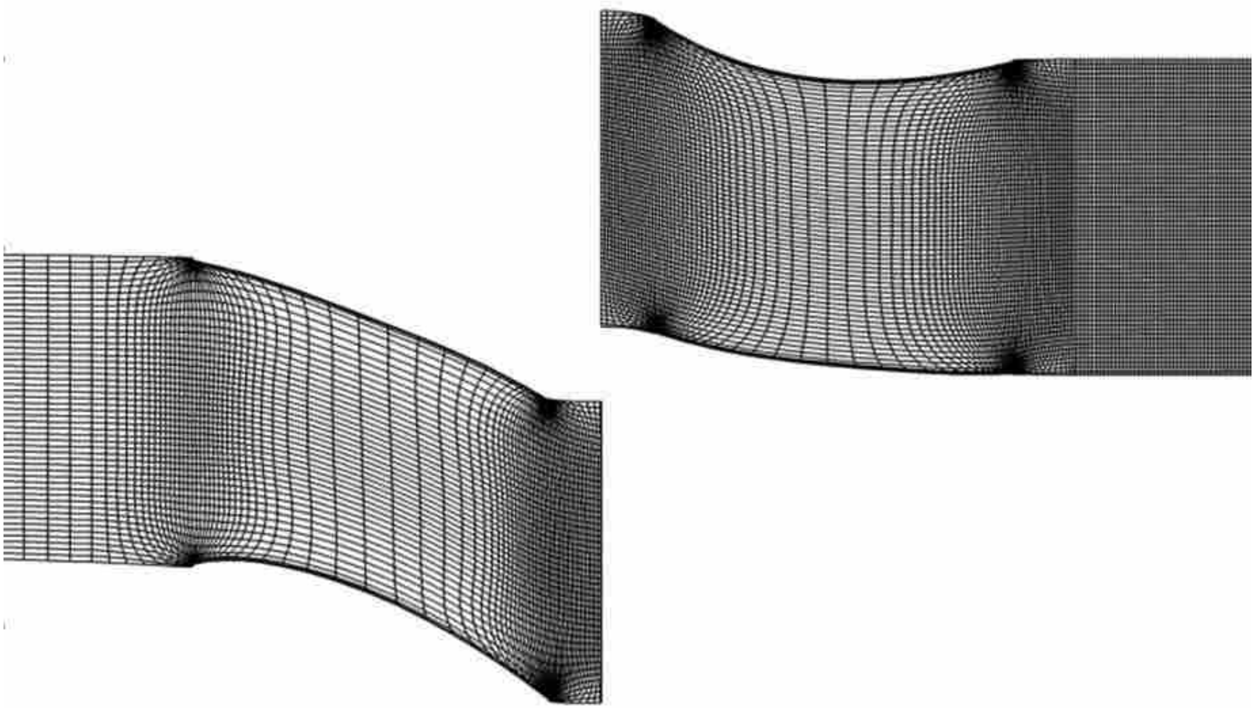

Figure 3.7: RANS Grid Centered on the Blade Rows (Every Third Node Shown) at Approximately Midspan

3.7 Convergence of the DNS and URANS Simulations

Determining proper convergence is important in establishing the validity of any CFD simulation. The selection of convergence criteria, from the wide array of possible criteria, should take into consideration the nature of the flow and the objective of the simulation. As the current study is of an internal flow, the corrected mass flow rate was selected as an appropriate convergence criteria. PTURBO tracks the corrected mass flow rate at four points in the numerical domain: the inlet

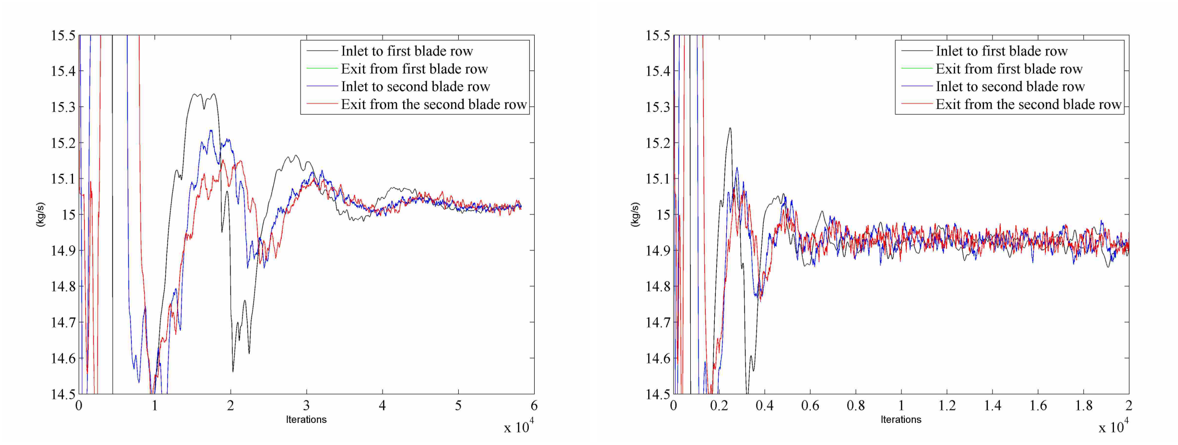

(a) (b)

Figure 3.8: The Corrected Mass Flow Histories for the (a) UDNS and (b) the RANS Simulation

and exit to each of the two blade rows. The corrected mass flow rate was considered converged when it changed only 0.1% of the inlet value.

The mass flow rate history for the DNS is shown in Figure 3.8(a). A series of large oscillations in the mass flow rates is seen in the first 10,000 iterations. These oscillations continued to diminish over the next 40,000 iterations until the convergence criteria was satisfied at approximately 50,000 iterations. The mass flow rate history of the URANS simulation, see Figure 3.8(b), demonstrates a similar pattern though convergence is achieved in a far smaller number of iterations. The initial oscillations occur during the first 1,500 iterations compared to the 10,000 iterations seen in the UDNS. The URANS simulation satisfies the convergence criteria after approximately 8,000 iterations. Each simulation required approximately 60 wake passing periods for the initial transients to dissipate. As the time step in the RANS simulation is an order of magnitude larger than that of the UDNS, the URANS converges in order of magnitude less number of iterations.

3.8 Postprocessing of the Data Sets

Postprocessing refers to the methods used to analyze the large amounts of data that are generated by CFD simulations. The focus of the postprocessing effort of the current work was the calculation of parameters of the wake profile. These parameters include the velocity defect, the streamwise and tangential turbulence intensities, the Reynolds shear stress, and the turbulence kinetic energy of the flow. The profiles of these parameters and the rates at which they change describe the flow physics occurring in the study domain. These parameters were calculated along the lines normal to the wake trajectory called rakes. Data extraction from the DNS data set proved to be a challenge due to its size.

3.8.1 Data Point Locations

A series of 8 rakes, or lines perpendicular to the wake trajectory, were used to display the wake profile at various points through the second blade row passage. Using data from the URANS simulation the wake trajectory was determined by tracking the wake center. A third order polynomial curve fit was developed for the path of the wake centerline. This polynomial was then used to calculate the end points of a line normal to the wake trajectory at various stations in the flow domain. These normal lines served to define the rakes. The curvature of the flow required a change in coordinates from an axial/tangential system to a $\varepsilon_1/\varepsilon_2$ system where ε_1 is the distance in the streamwise direction from the trailing edge of the wake generator and ε_2 in the normal direction to the wake path, see Figure 3.9. The method described in John and Schobeiri [1] was used to conduct this shift in coordinate systems. Rakes were created at ε_1/c values of 0.5, 0.66, 0.83, 0.98, 1.03, 1.13, 1.24, and 1.34. For the URANS data set each rake spanned approximately 2 cm and consisted of 30 nodes at which flow data were extracted and analyzed. The rakes used for the UDNS data set were only 1 cm long and contained 40 nodes.

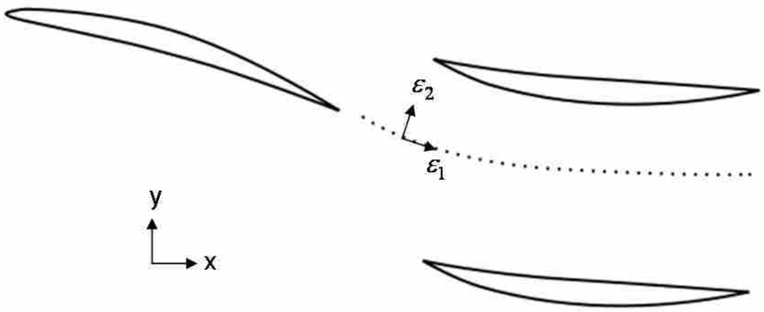

Figure 3.9: The Transformation to a Streamwise-Normal Coordinate System

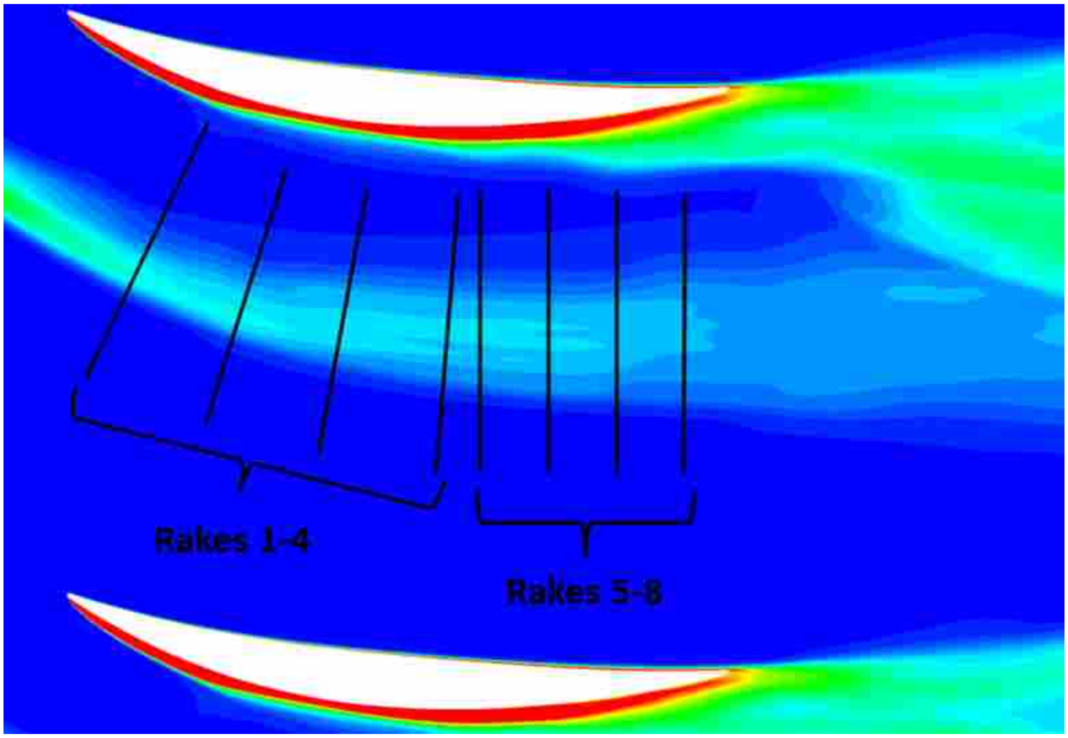

Figure 3.10: The Locations of Each Rake on a Contour of Time-Average Entropy from the URANS Data Set

The location of the rakes is illustrated in Figure 3.10. The first 4 rakes were located in a region where the wake is subjected to streamline curvature. The amount of curvature the wake passes through is quantified using a blade passage average value of the radius of curvature shown in the streamlines in the second blade row. This was calculated using streamline data from the RANS simulation. A sixth-order polynomial curve fit was created for nine various streamlines. These nine streamlines range from the entire tangential width of the domain. The equation of the polynomial curve, each yielding an R squared value of 1, was used to calculate the radius of curvature. The radius of curvature in the region where the first 4 rakes were located, $\varepsilon_1/c = 0.5$ through 0.98, had a blade passage average value of 7 cm and varied no more than 15% through the region. This curvature was considered to be mild as the radius of curvature was much greater than the calculated wake width. The rakes from $\varepsilon_1/c = 1.03$ to 1.334 had an infinite radius of curvature. The flow is exposed to an adverse pressure gradient with the static pressure increasing 15% of standard atmospheric over the eight rake locations. This gradient was calculated using blade passage average values of static pressure located at $\varepsilon_1/c = 1.03$ and $\varepsilon_1/c = 1.34$ and the axial distance between the two locations. The radius of curvature and pressure gradient was calculated from the URANS data set a time-average data set for the UDNS was not determined.

3.8.2 Statistical Condition of the Data

For a set of unsteady data to be representative of the flow, the set must contain enough data points to be statistically stable. The stability of the data was assessed by various means. First, the statistical moments (the mean, the standard deviation, the skewness, and the kurtosis) were calculated using data sets of various sizes for a given node (see Figure 3.11). The mean is the average value of the velocty signal. The standard deviation represents the amount of spread in the data signal whereas the skewness indicates whether the signal has greater values above or below the signal. The kurtosis indicates the number of values in teh signal that are located away from the mean. An indicator of stability of the set is the fact that these moments remain constant with increasing number of data points in the set. The mean and standard deviation values became constant with relatively few number of data points compared to the number required for the skewness and kurtosis to become steady. The behavior of the moments varies greatly from one end of the rake to the other. There were two types of velocity signals observed among the nodes of all 8 rakes. An example of each of these types of signals is shown below in Figure 3.12.

Figure 3.12(a) shows the axial velocity signal from the node on Rake 1 ($\varepsilon_1/c = 0.5$) that is located closest to the suction side of the second blade row. This type of signal is characterized by small deviation from a mean value except for a few large, sudden changes in velocity. This type of signal describes the unsteady separation occurring on the suction side of the second blade row. Generally, the flow at this node is relatively constant except when a separation zone passes and sudden jumps in the moments occur, (see Figure 3.11). The passing of these separation zones are embodied in the velocity signal as large sudden changes in velocity. The kurtosis values for this type of signal varied between 10 and 16 (see Figure 3.11(d)). This is compared to a Gaussian kurtosis value of 3. The skewness of this signal ranged from 1 to -1, whereas the gaussian value is 0. The unsteady passing of areas of separated flow affect the nodes on the end of the rakes that approach this side of the blade. This results in the high values of kurtosis and unsteady skewness values.

Figure 3.12(b) shows the time trace of a node in the middle of Rake 1 which illustrates the second type of signal contained in the data set. This type of signal was observed in the nodes that are located away from the separation occurring near the blade. It is characterized by a larger standard deviation from a mean value (see Figure 3.11(b)). This larger distribution is indicative of the numerous eddies of various sizes in the wake passing the node. As a result, the moments of this type of signal are more stable and has kurtosis and skewness values that are closer to that of a Gaussian distribution. The kurtosis value was observed to be 6, compared to 14 in the other signal, while the skewness value was -0.5, compared to 1 of the other signal. The moments of this type of signal is more steady than those from the previous type of signal. The fact that all of the nodes that describe the wake in the UDNS, and most that describe the wake in the URANS simulation, are those that exhibit the second type of signal indicates the nodes where the pertinent data is generated are of stable condition.

A technique of windowing was also applied to better assess the stability of the data set. In this process, outlined by Nichols [8], the entire data set for each node was divided into four distinct 'windows'. The statistical moments were calculated in each window. The stability of the data set as a whole was assessed by the difference in the values of these moments for the various windows of the same rake. An average value was calculated for each moment across the windows of each rake. The error between the moments of the individual windows and this average value was calculated. This error was presented as a percentage of the average value on that node. The maximum error value, for both skewness and kurtosis, was used to judge the stability of the data set. The mean value and standard deviation of these maximum error values was calculated for various numbers of data points in the data set. The use of the mean and standard deviation is required since some nodes exhibit the previously mention first type of signal while some exhibit the second type. For each data set, UDNS and URANS, the mean value and the standard deviation of the max error for all of the nodes approached a value of approximately 15% with increasing number of data points in the set. The mean value and standard deviation of the skewness show a similar trend with an increasing number of data points. The magnitudes of the mean and standard deviation for the skewness are less representative of the stability of the data set because they are artificially large. This arises from the fact that the average skewness value for each node is nearly zero and therefore the skewness error is devided by a very small number. As the skewness followed a similar trend as

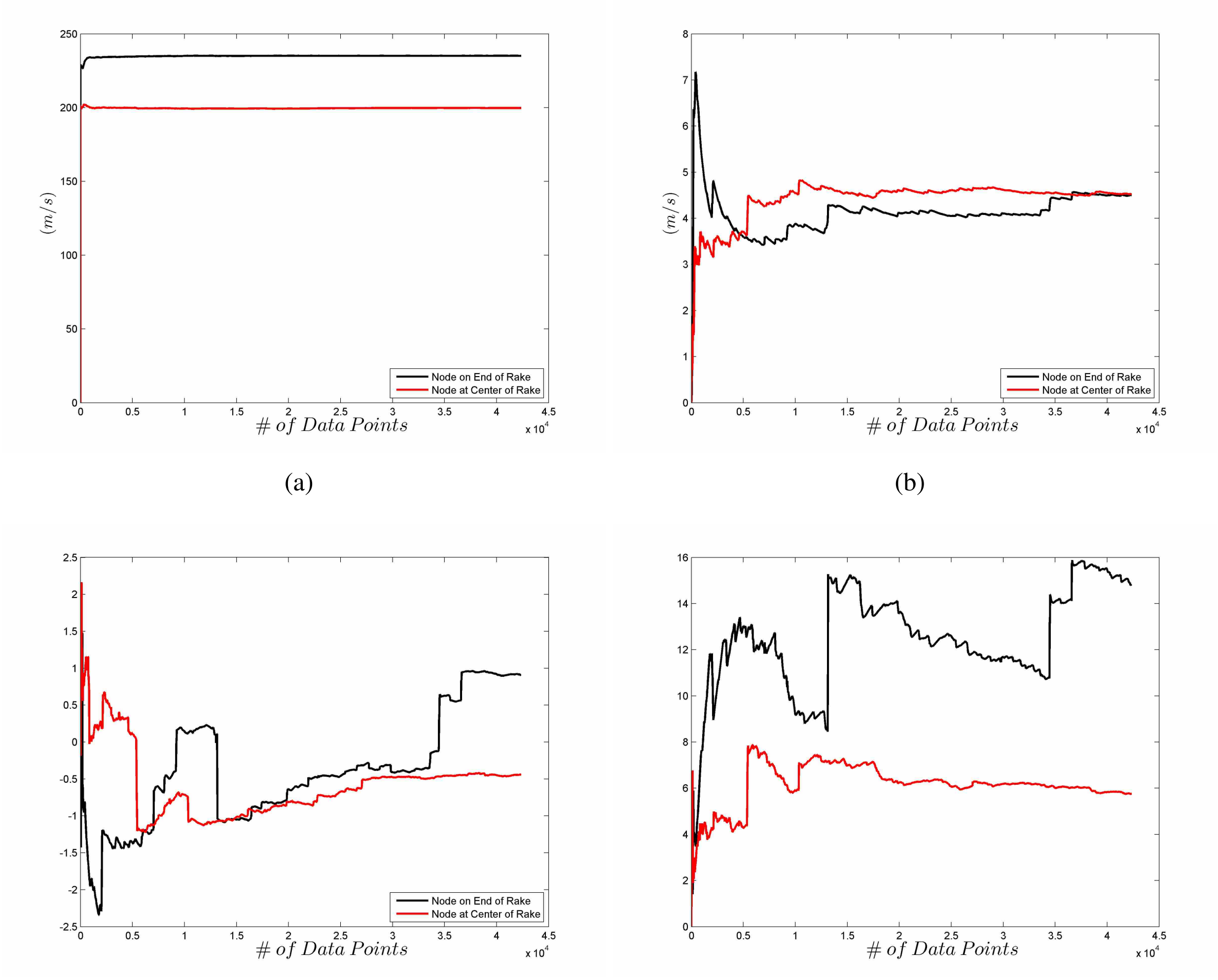

(a) (b)

(c) (d)

Figure 3.11: The First Four Statistical Moments (a) the Mean Velocity, (b) the Standard Deviation, (c) the Skewness, and (d) the Kurtosis of the Two Signals Observed in the UDNS Data

the kurtosis, it was observed that a data size set of 40,000 data points proved to be the size where gains in stability are negligible.

3.8.3 Calculation of Turbulence Transport Equation

The various terms of the transport equation of each component of the Reynolds stress (see Equations 3.5, 3.6, and 3.7) were calculated to identify the driving mechanisms behind the evolution of the turbulence structure of the wake. For each component the production, advection, and turbulent diffusion terms were calculated while the viscous diffusion, pressure gradient, and

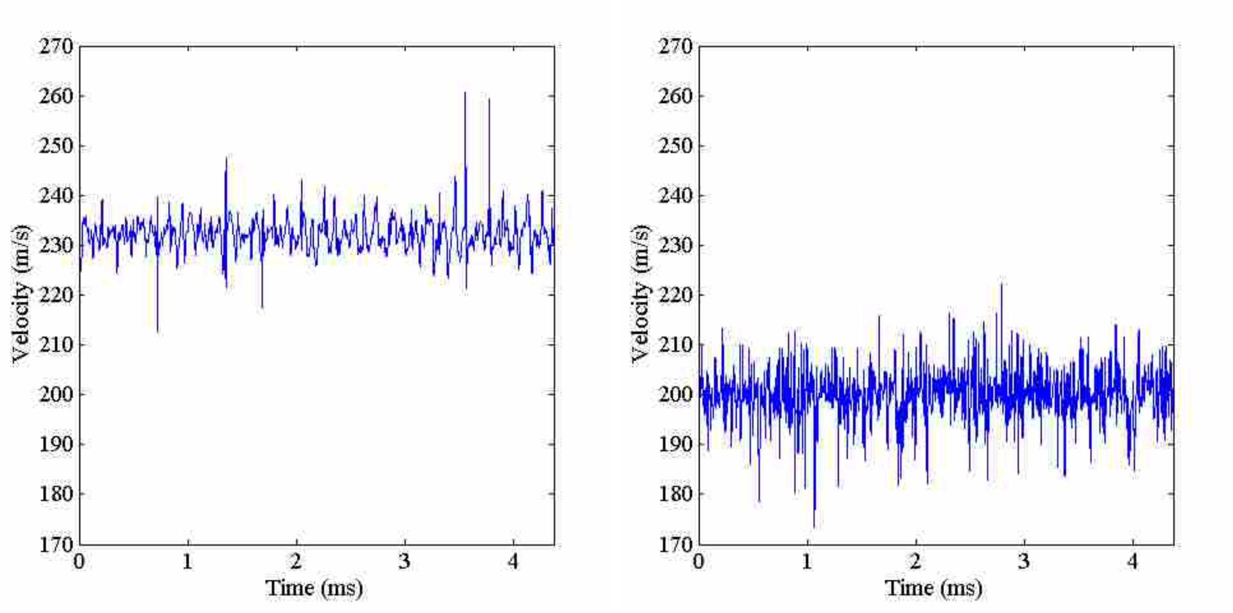

(a)

(b)

Figure 3.12: The Time Trace of Velocity of (a) a Node Near the Suction Side of the Blade and (b) a Node Away from the Suction Side of the Blade on Rake 1

dissipation terms were not. The advection term is represented by the first line in each respective equation. The production is represented by the second line and the turbulent diffusion by the third. The radius of curvature, R, in the transport equations was assumed to be a constant of 0.07 m for the first four rakes and infinite for the last four. The terms that were not calculated are listed on the fourth line. These include Π_{ii} the pressure-velocity gradient correlation, V_{ii} the viscous diffusion term, and ε_{ii} the dissipation term. Additionally, due to the two dimensional nature of the data available the terms in the z direction were not calculated. Comparison of the fluctuating components of the velocities shows that the fluctuations in the radial velocity are less than the fluctuations in the streamwise and tangential velocities. Specifically, the radial fluctuations are half to an order of magnitude smaller than the fluctuations in the other velocities. Subsequently, their contribution to the Reynolds stresses are assumed negligible. This was documented in a near wake behind a rotor [22].

The dissipation and pressure correlation terms were not calculated since the time trace data at the neighboring nodes surrounding the node where wake data were taken was not extracted. The viscous diffusion term is negligible at high Reynolds number [22]. Of these terms, dissipation is most significant and is the one that is affected by the under-resolved nature of UDNS. Dissipation is a viscous term that is dependent on the derivatives of the velocity components in all three directions. Since UDNS does not resolve the viscous length scales entirely, these derivatives are decreased and dissipation is underpredicted. The lower levels of dissipation translates into decreased turbulent transport of momentum and decreased decay rates in wake parameters. As the UDNS meets the benchmarks established by previous studies and is seen to yield good spectral analysis of the turbulence in the wake, it is assumed that the effect of using UDNS instead of DNS is minimal.

$$\begin{aligned}
\frac{\partial}{\partial t}(\overline{u'^2}) \quad = \quad & -\left[\frac{1}{h}\overline{u}\frac{\partial}{\partial s}+\overline{v}\frac{\partial}{\partial n}+\overline{w}\frac{\partial}{\partial z}\right](\overline{u'^2}) \\
& -\frac{2}{h}\overline{u'^2}\left(\frac{\partial\overline{u}}{\partial s}+\frac{\overline{v}}{R}\right)-2\overline{u'v'}\frac{\partial\overline{u}}{\partial n}-\frac{2}{h}\overline{u'v'}\frac{\overline{u}}{R}-2\overline{u'w'}\frac{\partial\overline{u}}{\partial z} \\
& -\frac{1}{h}\frac{\partial}{\partial s}(\overline{u'^3})-\frac{1}{h}\frac{\partial}{\partial n}(h\overline{v'u'^2})-\frac{2}{h}\frac{\overline{v'u'^2}}{R}-\frac{\partial}{\partial z}(\overline{w'u'^2}) \\
& +\Pi_s+V_s-\varepsilon_s
\end{aligned} \tag{3.5}$$

$$\begin{aligned}
\frac{\partial}{\partial t}(\overline{v'^2}) \quad = \quad & -\left[\frac{1}{h}\overline{u}\frac{\partial}{\partial s}+\overline{v}\frac{\partial}{\partial n}+\overline{w}\frac{\partial}{\partial z}\right](\overline{v'^2}) \\
& -2\overline{v'^2}\frac{\partial\overline{v}}{\partial n}-\frac{2}{h}\overline{u'v'}\frac{\partial\overline{v}}{\partial s}+\frac{4}{h}\overline{u'v'}\frac{\overline{u}}{R}-2\overline{v'w'}\frac{\partial\overline{v}}{\partial z} \\
& -\frac{1}{h}\frac{\partial}{\partial s}(\overline{u'v'^2})-\frac{1}{h}\frac{\partial}{\partial n}(h\overline{v'^3})+\frac{2}{h}\frac{\overline{v'u'^2}}{R}-\frac{\partial}{\partial z}(\overline{w'v'^2}) \\
& +\Pi_n+V_n-\varepsilon_n
\end{aligned} \tag{3.6}$$

$$
\begin{aligned}
\frac{\partial}{\partial t}(\overline{u'v'}) \quad = \quad & -\left[\frac{1}{h}\overline{u}\frac{\partial}{\partial s}+\overline{v}\frac{\partial}{\partial n}+\overline{w}\frac{\partial}{\partial z}\right](\overline{u'v'}) \\
& -\frac{1}{h}\overline{u'^2}\left(\frac{\partial \overline{v}}{\partial s}-\frac{\overline{u}}{R}\right)-\overline{v'^2}\frac{\partial \overline{u}}{\partial n}+\frac{1}{h}\left(\overline{u'^2}-\overline{v'^2}\right)\frac{\overline{u}}{R}-\overline{u'w'}\frac{\partial \overline{v}}{\partial z}+\overline{u'v'}\frac{\partial \overline{w}}{\partial z}-\overline{v'w'}\frac{\partial \overline{u}}{\partial z} \qquad (3.7) \\
& -\frac{1}{h}\frac{\partial}{\partial s}(\overline{u'^2 v'})-\frac{\partial}{\partial n}(\overline{v'^2 u'})-\frac{1}{h}\frac{2\overline{u'v'^2}-\overline{u'^3}}{R}-\frac{\partial}{\partial z}(\overline{w'v'u'}) \\
& +\Pi_{sn}+V_{sn}-\varepsilon_{sn}
\end{aligned}
$$

CHAPTER 4. RESULTS AND DISCUSSION

4.1 Overview

In this chapter the following will be discussed. The results of both the UDNS and the RANS simulation describe the effects of an adverse pressure gradient and streamline curvature on transonic wake flow. The mean velocity defect shows the asymmetry previously seen in the literature. The turbulence parameters show an increase in turbulence on the concave side of the wake centerline that gives rise to the asymmetry in the mean flow parameters. The transportation equations of the various components of the Reynolds stresses demonstrate that production and turbulent diffusion contribute to this asymmetry. Slight differences were observed between the profiles of turbulence kinetic energy and the normal components of the Reynolds stress tensor. Comparison of the URANS and UDNS data illustrates that the RANS simulation predicts a larger wake width and greater Reynolds stresses than the UDNS.

4.2 Results from the Under-Resolved Direct Numerical Simulation

Analysis of the data generated by the UDNS was performed to identify the characteristics of a curved wake propagating in the transonic flow regime in the presence of an adverse pressure gradient. The various sources of asymmetry and turbulence in the wake are discussed here. The transport equations of the Reynolds stresses were analyzed to identify the driving mechanisms behind the evolution of the asymmetry in those stresses.

Figure 4.1 shows the evolution of a vortical structure in the wake during one wake passing period using contours of normalized entropy flux from the UDNS. The normalized entropy flux is calculated by dividing the change in entropy for an ideal gas by the specific heat at constant pressure and then multiplying by the mass flux, or the product of the density and the axial velocity component. Entropy flux is useful in illustrating unsteady structures as areas of high entropy are shown to be zero if the velocity of the flow is negligible. Many small vortical structures were resolved due to the fine grid used for the UDNS. A pair of vortices are tracked as they propagate downstream. As these vortices propagate, one moves from being slightly behind the other to being directly above it. While both vortices grow as the wake widens, the vortex on top however appears to grow more than that on the bottom. In the later portion of the blade row the vortex on top, and the one on the bottom to an extent, begins to grow in the streamwise direction creating a 'bean' shaped vortex instead of the round shape observed in the first half of the blade row. The sources of this nonuniform spreading rate will be discussed in the section regarding the turbulence parameters of the UDNS data.

Figure 4.1 also displays significant behavior at the suction side of the second blade row. This area is located near the top of each respective image. At approximately quarter chord there is a source of entropy observed. A plot of axial velocity (see Figure 4.2) indicates that there is a discontinuous drop in velocity at the same location. This indicates a standing shock wave present in the flow. Consulting contours of total pressure, temperature, and Mach number confirm this observation. This shock wave separates the boundary layer as indicated by the separated vortical structures present downstream. This separated boundary layer appears to be located far enough as to not interfere with wake data measurements.

4.2.1 Time-Averaged Wake Parameters

Figure 4.3 shows the streamwise velocity distribution at each of the rake locations. The symbols represent the measured values while the lines depict the potential velocity, or the velocity that would exist if the wake was not present. This potential velocity is calculated by generating a third order curve fit to the data outside of the wake. A variety of types of curve fits have been used in previous studies, however a third order fit proved to fit the data of the current study best. The velocity defect is defined as the difference between the potential velocity and the measured value at a given point, or $\Delta\overline{u} = \overline{u}_p$ - $\overline{u}$. The wake width b, is defined using the velocity defect, see Equation 4.1. The normal coordinate, ε_2, is normalized by this wake width.

$$\mathrm{b} = \int_{-\infty}^{\infty} \Delta\overline{u} \,/\Delta\overline{u}_o \, d\varepsilon_2 \qquad (4.1)$$

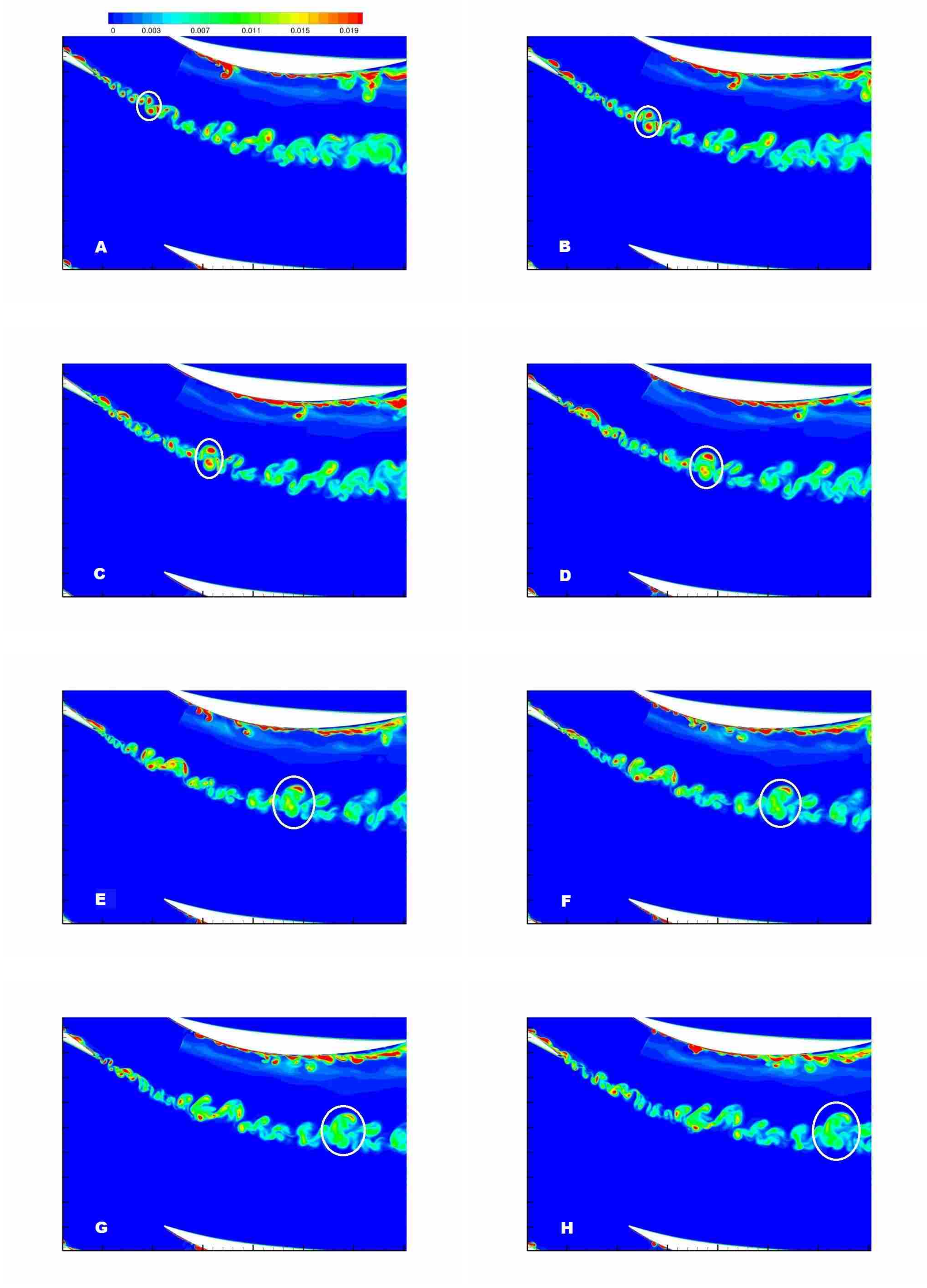

Figure 4.1: Contours of Normalized Entropy Flux from the UDNS

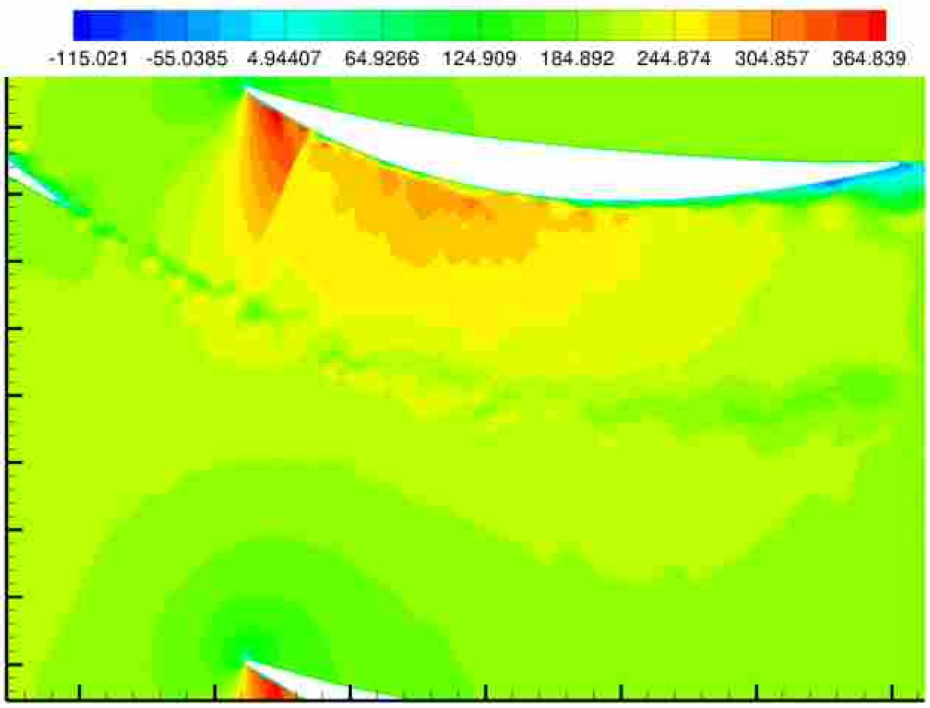

Figure 4.2: Contours of Axial Velocity (m/s) from the UDNS

The profiles of average velocity (see Figure 4.3) describe an asymmetric wake about the wake centerline. The wake width is noticeably larger on the concave side of the wake, or for $\varepsilon_2/b > 0$. This type of asymmetry has been documented if a cambered airfoil creates the wake [10, 11] or if streamline curvature is present [1, 2, 5, 7]. As both factors are present in the current study it is not readily discernible what effect each factor has on the profiles. The potential velocity increases with increasing ε_2/b. This slope in the potential velocity is explained through a review of the contours of axial velocity (see Figure 4.2). The region on the concave side of the wake is characterized by an acceleration of the flow due to flow blockage caused by the wake and the boundary layer on the suction side of the second blade row. The region on the convex side of the wake exhibits a lower velocity due to the presence of the blade. The wake borders these two regions and therefore the potential velocity shows the transition from the low speed area to the higher speed acceleration zone.

The wake width, the maximum velocity defect, and the normal Reynolds stresses are used to describe the structure of a wake as being in either the near, the intermediate, or far wake regime. A far wake is characterized by a mean velocity defect that is much smaller than the potential

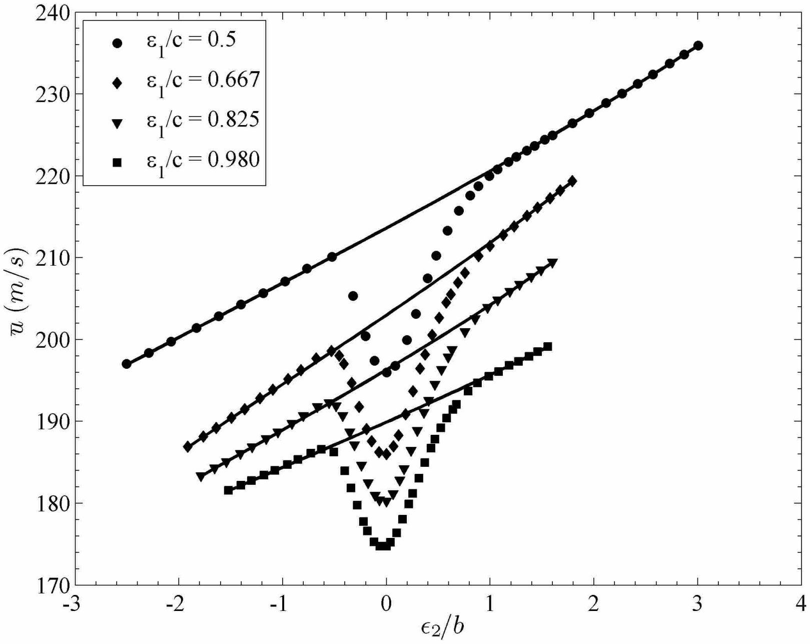

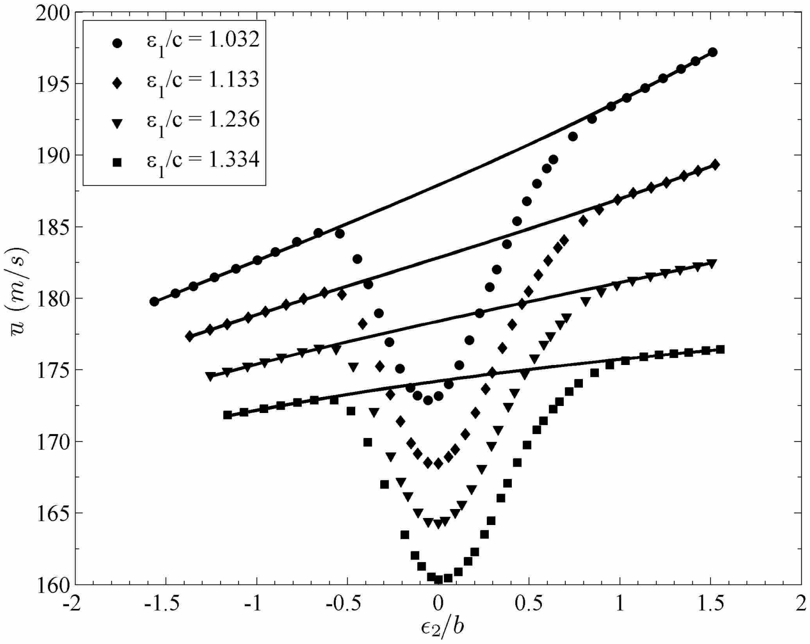

Figure 4.3: Time-Averaged Profiles of Velocity at Various Streamwise Positions

velocity at the wake center and a constant wake width. The growth of the wake width shown in Figure 4.4(a) demonstrates an increase from 2.5 mm to 4.5, or 100% of its value at ε_1/c = 0.50, in three quarters of a chord length. The wake width clearly does not demonstrate the condition of a constant value which characterizes a far wake. The maximum velocity defect at the centerline, $\Delta\overline{u}_o$, normalized by the potential velocity at the centerline $\overline{u}_{po}$ is shown in Figure 4.4(b). The velocity defect at the wake centerline is only approximately 8% of the potential velocity at the centerline and changes less than 1% over three quarters of a chord length. In a far wake the Reynolds stresses are of similar orders of magnitude. It will be shown later in this section that is the case. The behavior of the maximum velocity defect and the turbulent stresses are similar to that of a wake in the far wake region. The growth of the wake width however does not represent far wake flow as it is not observed to be relatively constant. Since two parameters, the velocity defect and turbulent stresses, characterize a far wake while another, the growth of the wake width, does not the wake studied here was categorized as an intermediate wake.

A normalized profile of velocity defect at the various rakes is show in Figure 4.5. The velocity defect was normalized by the maximum velocity defect at each rake while the normal distance from the wake center was normalized using the wake width. The profiles demonstrate the presence of similarity in the wake as they collapse onto a single curve. There is a definite asymmetry in the profiles. The normalized defect on the concave side of the wake reaches a zero value in twice the distance than the wake on the convex side. This agrees with Zhang and Ligrani's [11] observation of a wake behind a cambered airfoil in transonic flow. Wakes behind a symmetric geometry have consistently shown a symmetric profile of velocity defect when cast in similarity variables.

4.2.2 Turbulence Parameters

The profiles of the streamwise component of the normal Reynolds stresses, $\overline{u'^2}$, illustrate the transition of dominance from one source of turbulence in the wake to another. Figure 4.6 shows the profiles of these stresses normalized by the square of a reference velocity located one chord length upstream of the leading edge of the airfoil generating the wake. At ε_1/c = 0.50, the profile differs from others in that it shows a single peak near the wake center instead of two separate peaks

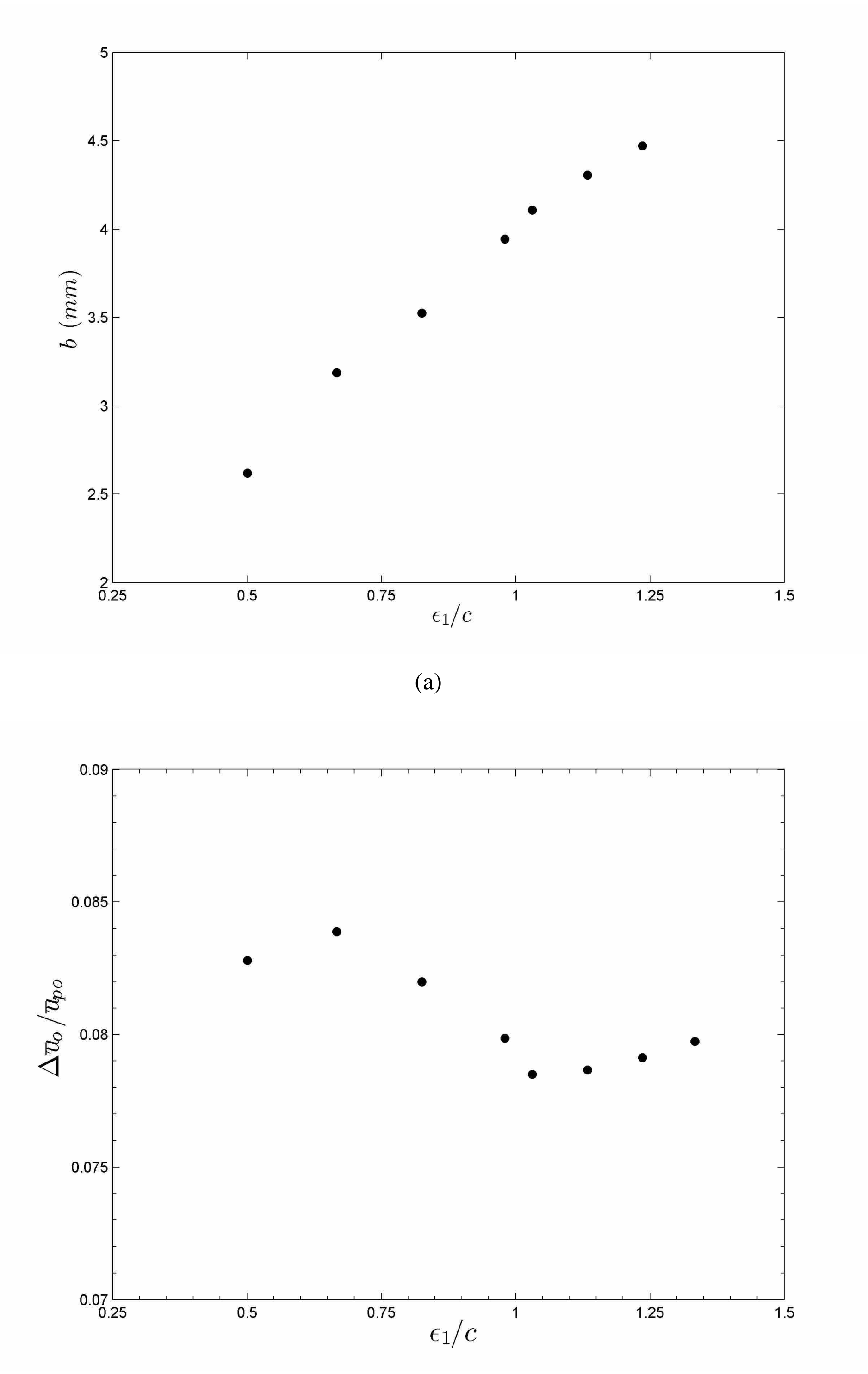

(a)

(b)

Figure 4.4: (a) The Growth of Wake Width and (b) The Decay of the Maximum Velocity Defect

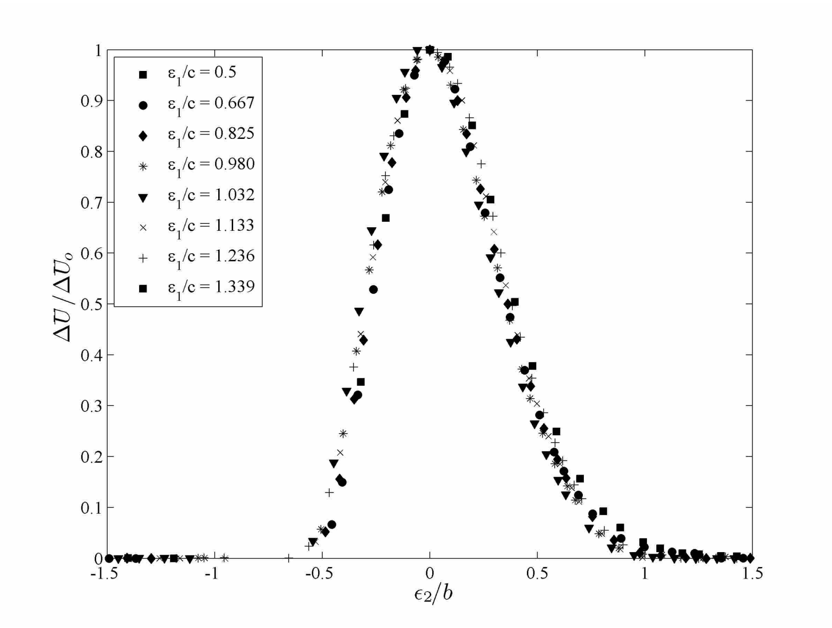

Figure 4.5: Profile of Mean Velocity Defect in Similarity Variables

near the locations of peak shear (ε_2/b = 0.2 and -0.2) as is also shown in incompressible wake studies [1,5]. This difference is explained by considering the transport equation of $\overline{u'^2}$ as in [22].

The profiles of the production, advection, and diffusion terms of $\overline{u'^2}$ are shown in Figure 4.7 and since the trends are similar only two rakes are shown here. The profile of the production of $\overline{u'^2}$ consists of two peaks, each at the location of peak shear on each side of the wake with a minimum at the wake center. The peak located on the concave side is significantly larger than that on the convex side of the wake. The region $-0.3 < \varepsilon_2/b < 0.1$ experiences large advection and turbulent diffusion terms which compete against the production term. At ε_1/c = 0.50, the production of $\overline{u'^2}$ near the wake center is overwhelmed by these large advection and turbulent diffusion terms. This indicates that the amounts of $\overline{u'^2}$ being transported away from the area of the wake center is significantly more than the amount that is produced in that area of the wake. After analysis of the flow being shed from the airfoil, it was determined that the boundary layer at the trailing edge was separated. This observation of a separated boundary layer is illustrated in Figure 4.8 where contours of unsteady entropy flux near the trailing edge of the wake generator show two separated vortices near the trailing edge. The levels of $\overline{u'^2}$ created in this separated wake dominate those created by production in the wake. This results in the single peak observed in Figure 4.6 which is similar to profiles observed in previous studies of wakes behind cambered airfoils [10,11].

Figure 4.6 shows that $\overline{u'^2}$ decays at a faster rate on the convex side of the wake center, $\varepsilon_2/b < 0$, than on the concave side. The result of this decay is an asymmetric profile with two peaks, the larger being located near ε_2/b = 0.2. Two aspects of the transport equation of $\overline{u'^2}$ (see Figure 4.7) play a driving role in this evolution. The first aspect is that the peak in production located at ε_2/b = 0.2 is between two and four times larger than the peak located at ε_2/b = -0.2, depending on streamwise position (see Figures 4.7(a) and 4.7(b)). The second factor is that the large advection and turbulent diffusion terms far surpass production near the centerline as well as the smaller peak in production located on the convex side of the wake. The advection and turbulent diffusion however affect the significantly larger peak in production on the concave side of the wake to a much lesser extent. As the advection and diffusion terms sufficiently diminish the levels of $\overline{u'^2}$ that existed originally in the wake due to the separated nature of the boundary layer; the effects of the peaks in production become the main contributors to the shape of the profile. While the large production on the concave side of the wake slows the decay on that side; the advection and diffusion terms dominate near the centerline and on the convex side of the wake causing the levels to decay much faster. The resulting asymmetric profile is very similar to those observed in a curved incompressible wake behind a cylinder [1] where the peaks in $\overline{u'^2}$ were observed to occur at ε_2/b = 0.2 and -0.2. The production of $\overline{u'^2}$ was observed to dominated by shear effect; as the effect of curvature was only 20% of that of shear at any given rake.

In an effort to quantify the magnitude of the asymmetry in the peak values of the streamwise normal stresses, Figure 4.9 presents the streamwise Reynolds stresses normalized by their value at the wake centerline. The peak value of $\overline{u'^2}$ on the concave side varies from 1.0 at ε_1/c = 0.50 to 1.32 at ε_1/c = 1.34. This is 20% more asymmetry than was observed by John and Schobeiri [1] behind a cylinder, where the peak value was observed to be 1.1. The increasing asymmetry also provides another vantage point to observe the evolution of the effects of the production terms, i.e. the peaks located away from the centerline, becoming more prominent compared to the prexisting levels of $\overline{u'^2}$ located near the wake centerline. This asymmetry in $\overline{u'^2}$ translates into increased turbulent transport of streamwise momentum in the streamwise direction on the concave side of the wake. Thus the streamwise momentum in the upper vortex in Figure 4.1 moves in the streamwise direction more than in the lower vortex creating the 'bean' shape previously observed.

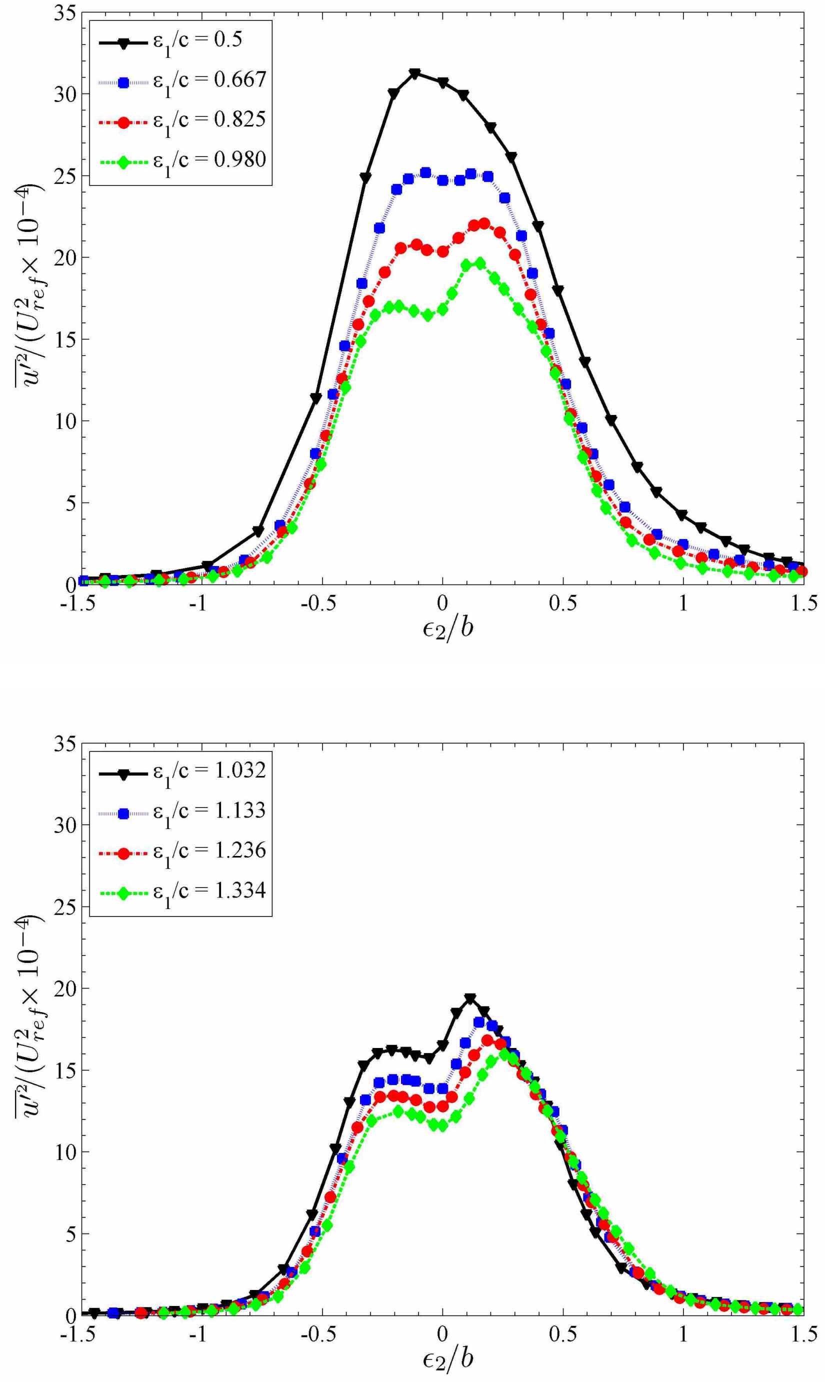

Figure 4.6: Profiles of $\overline{u'^2}$ for Various Streamwise Positions

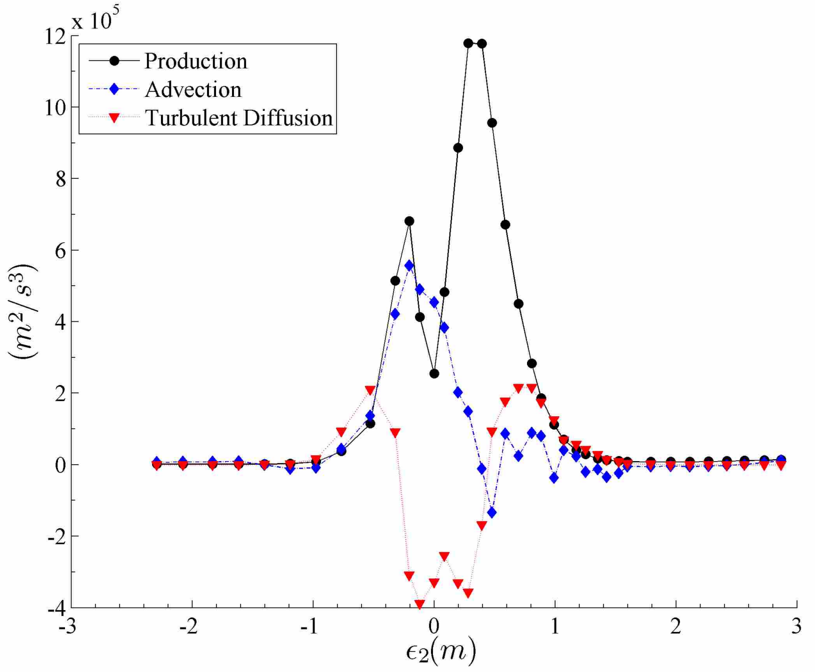

(a)

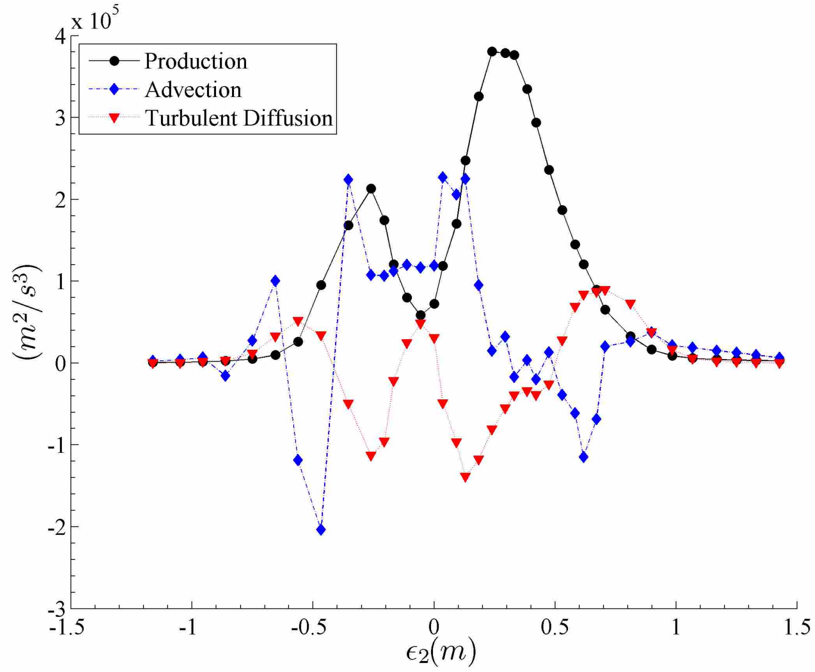

(b)

Figure 4.7: Contributing Terms to the Evolution of $\overline{u'^2}$ for (a) ε_1/c = 0.50 and (b) ε_1/c = 1.236

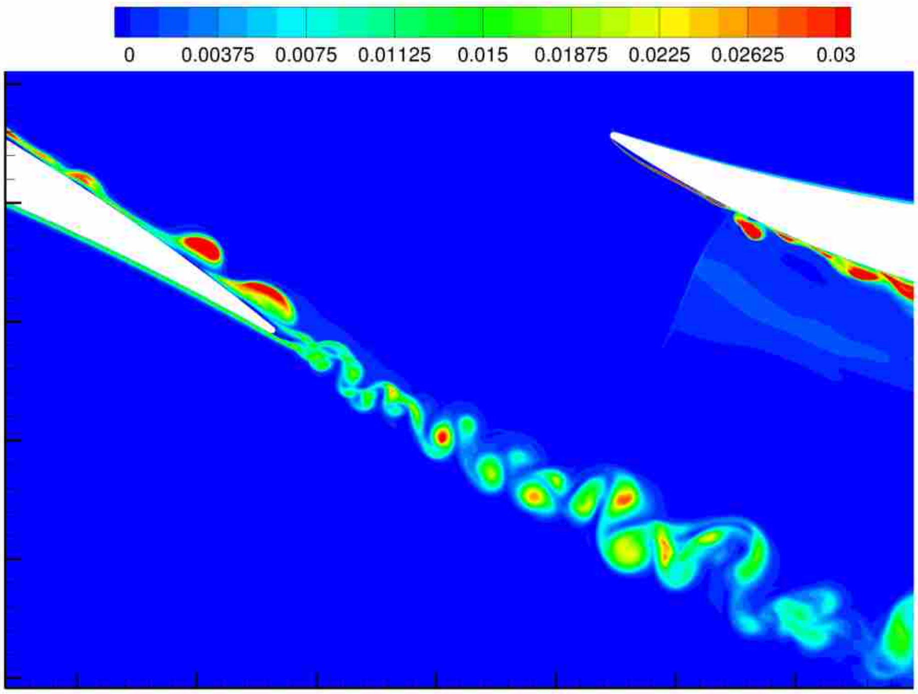

Figure 4.8: Contours of Unsteady Entropy Flux at the Trailing edge of the Wake Generator

Similar to those of the streamwise Reynolds stresses, the profiles of the tangential stresses $\overline{v'^2}$ illustrate a transition from a single peak profile in the rakes between ε_1/c = 0.50 and .980 to a different profile in the ones between ε_1/c = 1.034 and 1.334. The profile in the latter rakes consists of a peak located at ε_2/b = -0.06 connected to a smaller peak, located at ε_2/b = 0.2, by a linear slope. Analyzing the transport equation of $\overline{v'^2}$ (see Equation 3.6), whose plots are presented in Figure 4.11, provides an insight into how this transition takes place. At ε_1/c = 0.50, the advection and diffusion of $\overline{v'^2}$ are very large and are accompanied by a peak in negative production on the concave side of the wake (see Figure 4.11(a)). Since all three of these mechanisms contribute to diminish the levels of $\overline{v'^2}$ and there are no observable sources at this rake; the amount of $\overline{v'^2}$ being transported is the product of the separated boundary layer that formed the wake. At ε_1/c = 0.825 a peak in positive production begins to appear on the convex side of the wake near the wake centerline. This peak is due to a decreasing negative shear production component and a relatively stable component of positive curvature related production. This positive production competes against the advection and diffusion terms thereby slowing the decay of $\overline{v'^2}$ just left of the wake centerline in Figure 4.10. As the positive production slows the decay of $\overline{v'^2}$ on the convex side of the wake, the negative

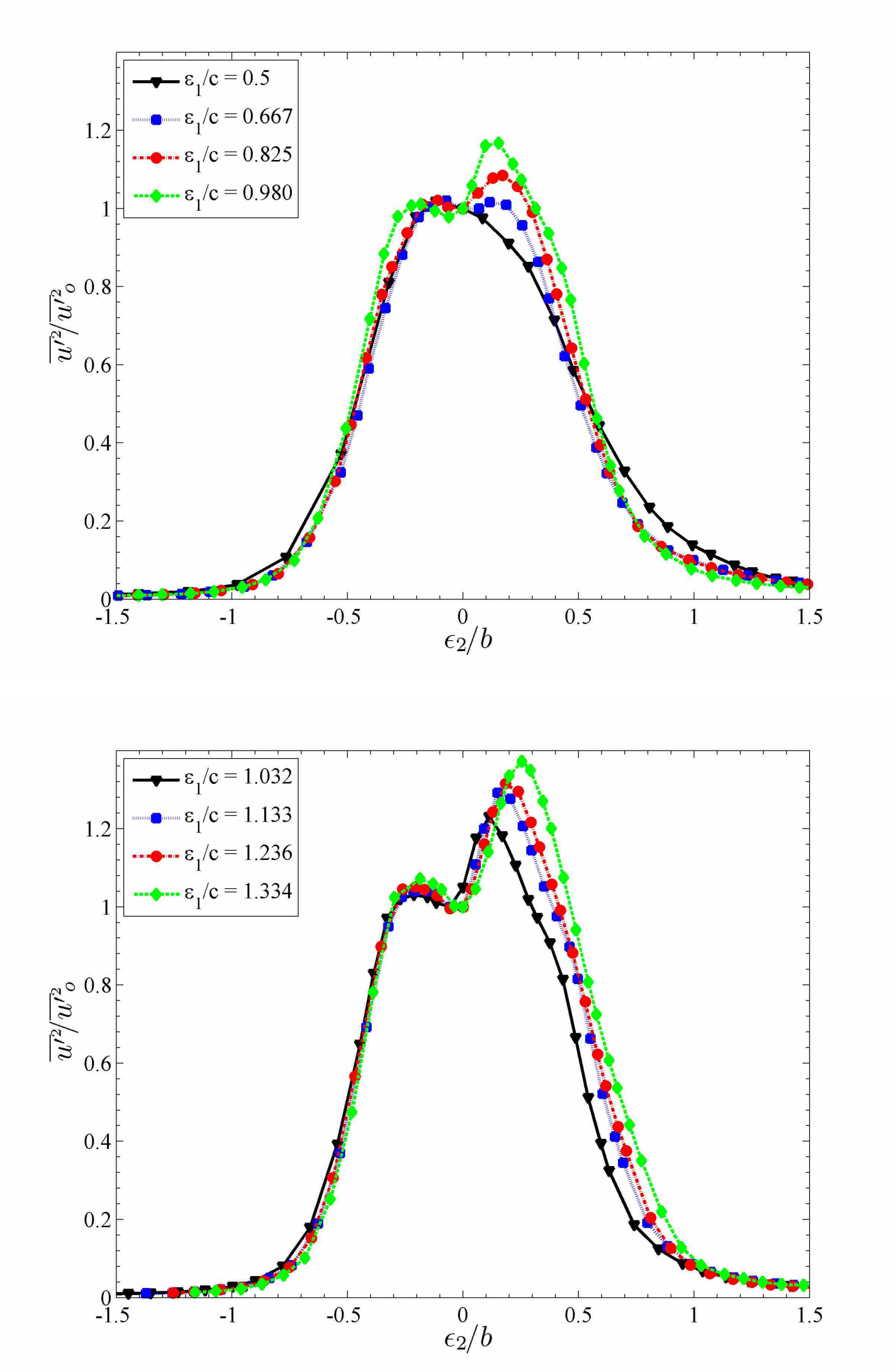

Figure 4.9: Profiles of $\overline{u'^2}$, Normalized by its Value at the Wake Center

production located on the concave side of the wake hastens it (see Figure 4.11(b)). This results in the lower peak observed at ε_2/b = 0.2. The profiles observed between ε_1/c = 0.980 and 1.34 differ somewhat from those observed by John and Schobeiri [1] for a curved wake shed by a cylinder where a single peak of $\overline{v'^2}$ occurred at ε_2/b = 0.2. The production of $\overline{v'^2}$ on the convex side of the wake is driven by the effects of curvature and to a lesser extent by those of shear. From ε_1/c = 0.980 to 1.334, the flow is no longer exposed to streamline curvature. As a result, The production is greatly diminished leaving the advection and diffusion terms dominant. The advection term is rather uniform from $-0.5 < \varepsilon_2/b < 0.5$ while the diffusion term is symmetric about the wake center. This results in the profile of $\overline{v'^2}$ being rather constant from ε_1/c = 0.980 to 1.334 (see Figure 4.10).

Figure 4.12 displays the profiles of $\overline{v'^2}$, normalized by its value at the wake center and shows a very slow change in the asymmetry of the profiles. The peak value of $\overline{v'^2}$ is shown to be 1.04 times the centerline value. This is significantly less than the asymmetry observed in the profiles of $\overline{u'^2}$. This also differs from the observations of John and Schobeiri [1] in that greater asymmetry was observed in the $\overline{v'^2}$ profiles than in those of $\overline{u'^2}$. The location of the peak in $\overline{v'^2}$ differs from those that have been documented in previous wake studies and so helps to fill the void in the current body of knowledge pertaining to the behavior of transonic curved wakes.

The profiles of the the Reynolds shear stresses, $\overline{u'v'}$, on the convex side (see Figure 4.13) differ from the trends observed in the normal stresses. Similar to the normal stresses the profile at ε_1/c = 0.50 differs from those of the following streamwise positions. The peak value on the convex side is 60% higher than those on the convex side of the following rakes. In the profiles of $\overline{u'^2}$ and $\overline{v'^2}$, deviations observed at ε_1/c = 0.50 were determined to be the result of the presence of turbulence created in the separated boundary layer that created the wake. This determination was made due to the overwhelmingly large advection and diffusion terms indicating that the turbulence transport out of peak areas was more than the turbulence produced in that area of the wake. The analysis of the transport equation of $\overline{u'v'}$ however shows that shear driven production dominates the evolution of the profile on the convex side of the wake, at ε_1/c = 0.50, and not advection and diffusion (see Figure 4.14) as in the case of the normal stresses. Since the peak value of $\overline{u'v'}$ decreases from ε_1/c = 0.50 to 0.667, a term other than advection or turbulent diffusion must eclipse the production term to yield this decrease in levels. Therefore the $\overline{u'v'}$ present in the wake from the

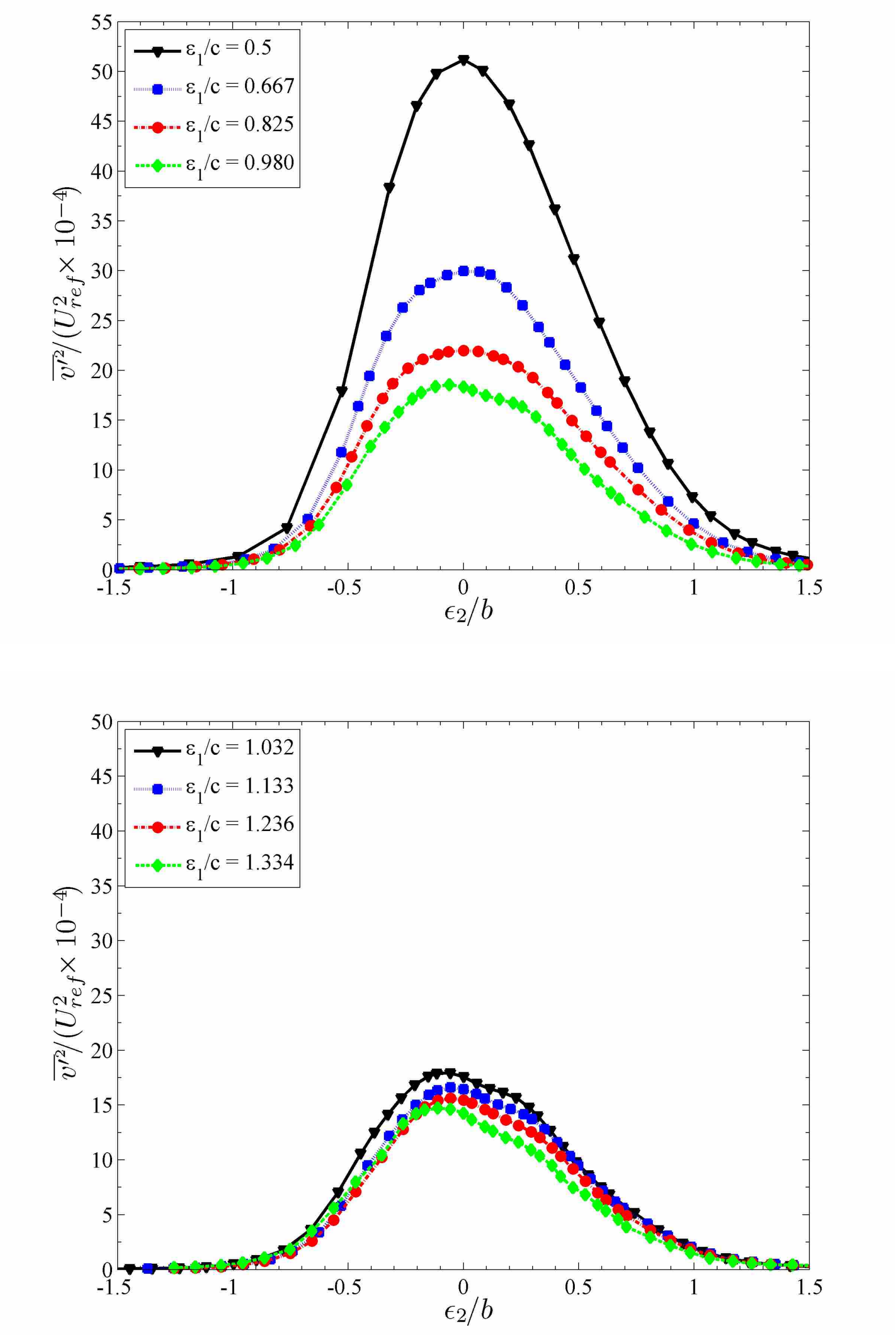

Figure 4.10: Profiles of $\overline{v'^2}$ for Various Streamwise Positions from the UDNS

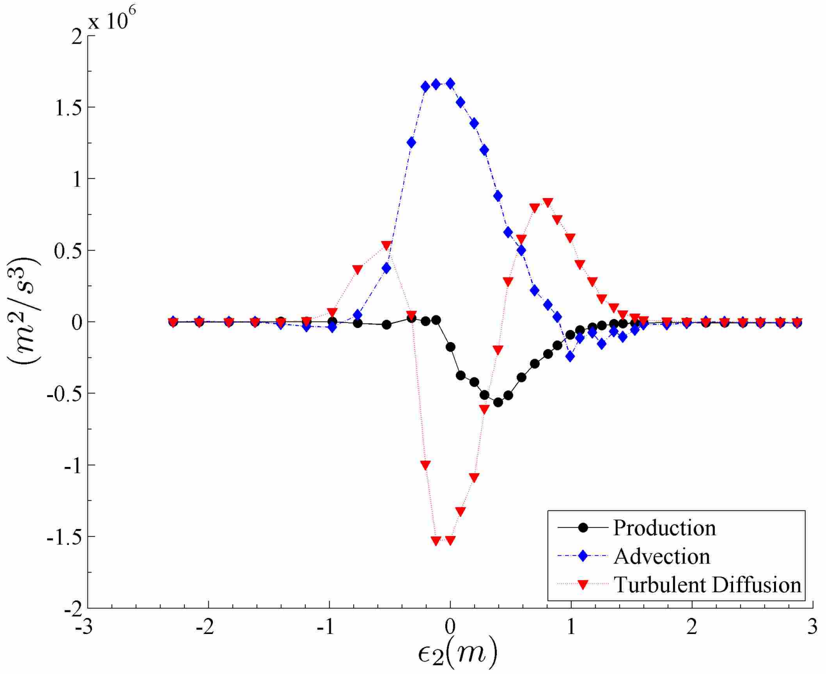

(a)

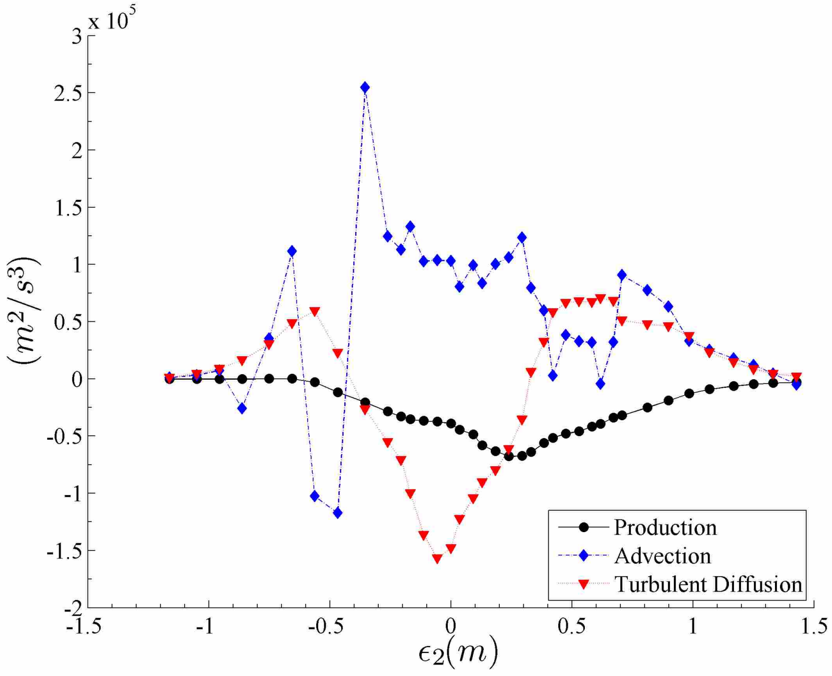

(b)

Figure 4.11: Transport Equation Terms of $\overline{v'^2}$ for (a) $\varepsilon_1/c = 0.50$ and (b) $\varepsilon_1/c = 1.236$

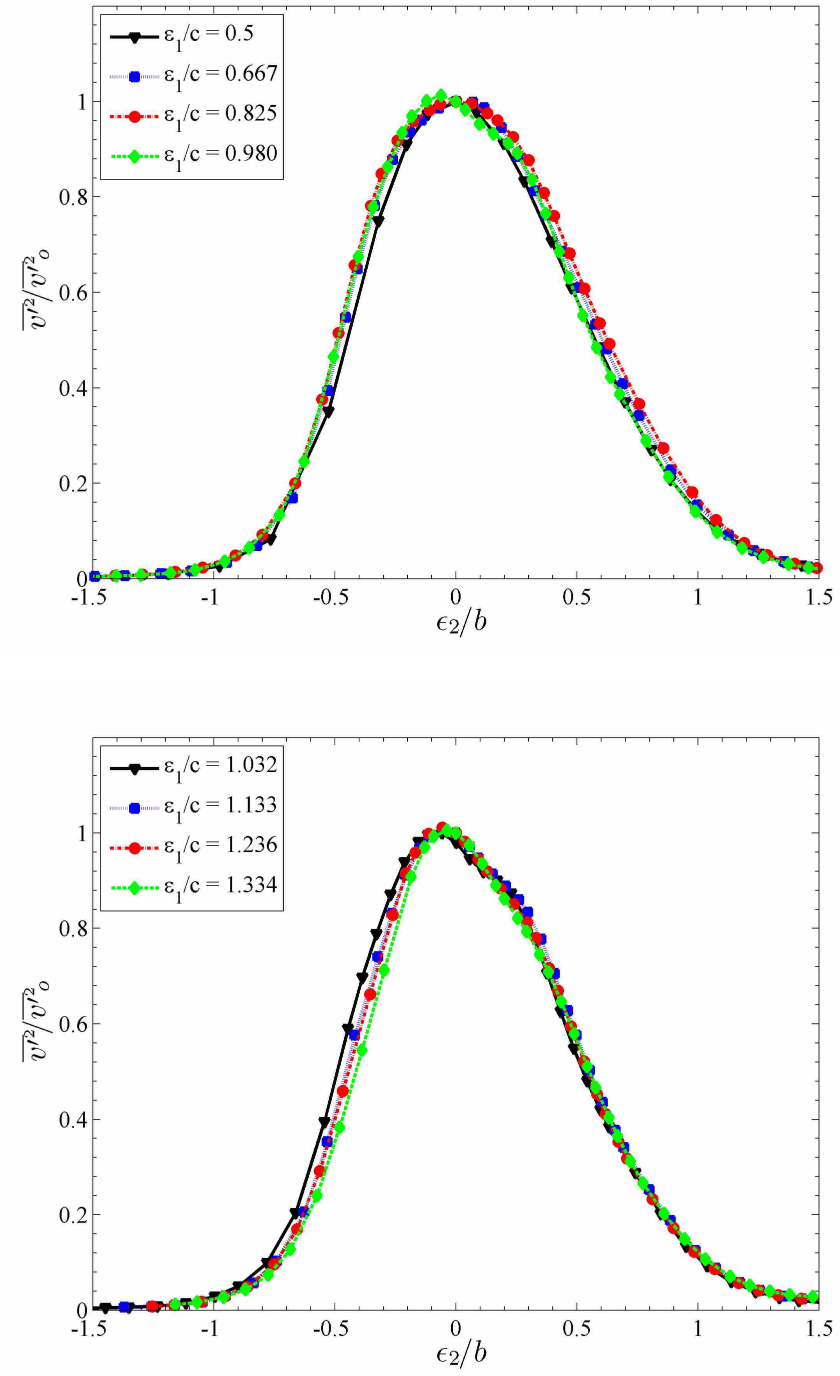

Figure 4.12: Profiles of the Tangential Normal Components of the Reynolds Stress Tensor from the UDNS

separated boundary layer must be decreased by either the velocity-pressure-gradient correlation or the viscous dissipation. Due to decay of the production term, the diffusion term soon balances this production term yielding the rather constant peak values on the convex side in Figure 4.13.

The behavior of the peak values of $\overline{u'v'}$ on the concave side of the wake is largely due to a dominant turbulent diffusion term and a contributing production term. Overall the peak value on the concave side of the wake is twice as large as the peak on the convex side of the wake. Since the shear stresses are the mechanism through which streamwise momentum is transported in the tangential direction, this asymmetry is the cause of the differing growth rates observed in the vortex pair in Figure 4.1. There is a decrease though in peak levels on the concave side from $\varepsilon_1/c = 0.50$ to 0.667, followed by a constant increase from 0.667 to 0.825. From $\varepsilon_1/c = 0.825$ to 1.334 the peak value declines by approximately 20% of the value at $\varepsilon_1/c = 0.825$. In the analysis of $\overline{u'^2}$ and $\overline{v'^2}$, the turbulent diffusion term competed against the production term. For $\overline{u'v'}$ however, the turbulent diffusion combines with a negative production term to enhance the negative values on the concave side of the wake (see Figure 4.14). This large, negative turbulent diffusion term is dominated by the diffusion term that is related to curvature (this is the third term on the third line of Equation 3.7). As the mechanisms that usually decrease levels of $\overline{u'v'}$ are either negligible or contributing to the peak values on the concave side of the wake the decrease of peak values from $\varepsilon_1/c = 0.50$ to 0.667 must arise from a large dissipation term. After $\varepsilon_1/c = 0.667$, the effects of the cambered airfoil that shed the wake diminish sufficiently so that the effects of curvature dictate the evolution of the shear stresses. Since the production and diffusion terms decay by 40% from $\varepsilon_1/c = 0.667$ to 1.032; the increase in peak levels observed in this range must arise from the dissipation term decaying faster than the the contributing factors. Once curvature no longer affects the flow, the diffusion term that was driving the asymmetry in the profiles of $\overline{u'v'}$ disappears and is replaced by a symmetric production term as the dominant factor in the evolution of the profiles (see Figure 4.14(b)). With the disappearance of the asymmetric diffusion term, the peak values on the concave side of the wake in Figure 4.13 begin to decrease between $\varepsilon_1/c = 0.825$ and 1.334 as the profiles regain their symmetry.

In low speed wake studies behind a variety of geometries, it has been observed that curvature enhances turbulence stresses on the concave side of a curved wake [1,2,5]. The shear stresses observed in this work (on transonic curved wakes behind a cambered airfoil) showed a similar

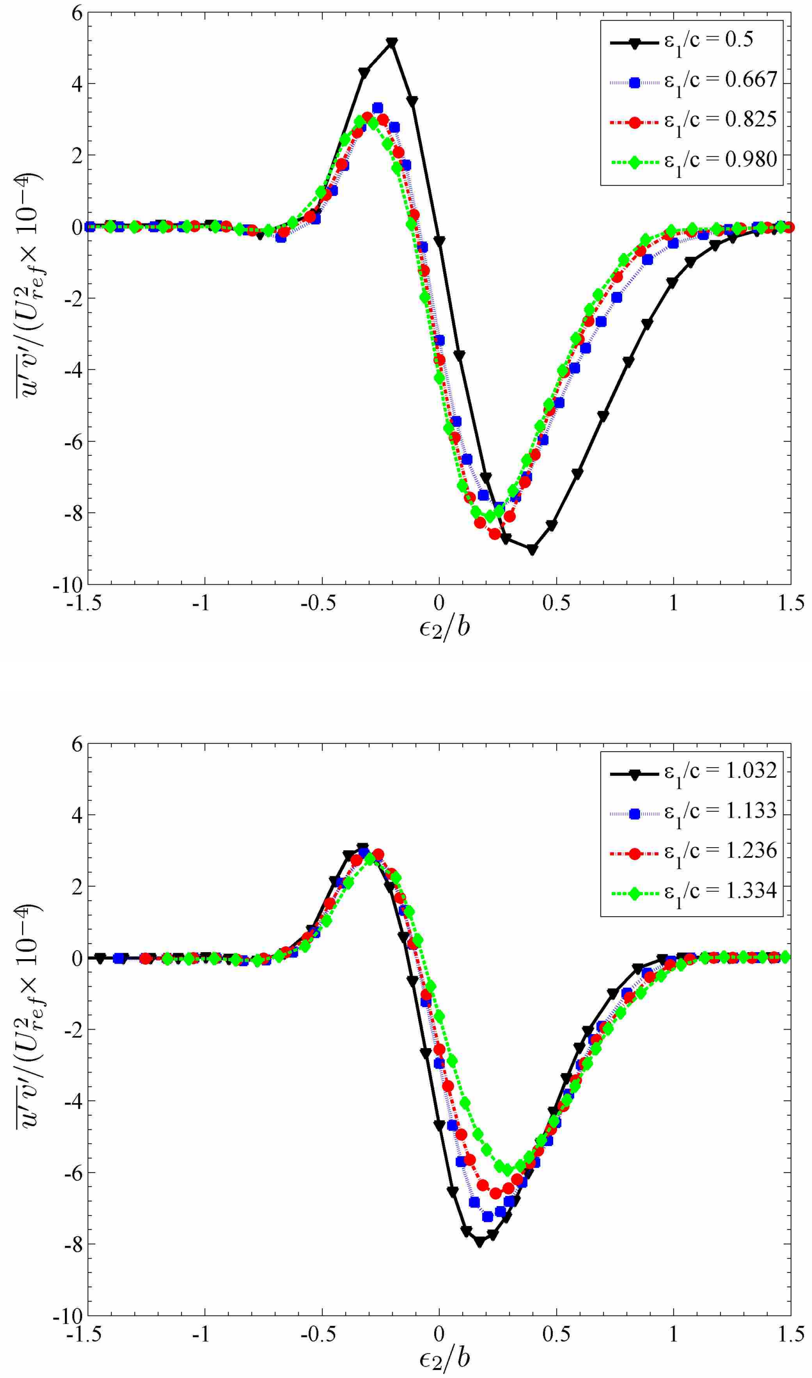

Figure 4.13: Profiles of the Reynolds Shear Stresses from the UDNS

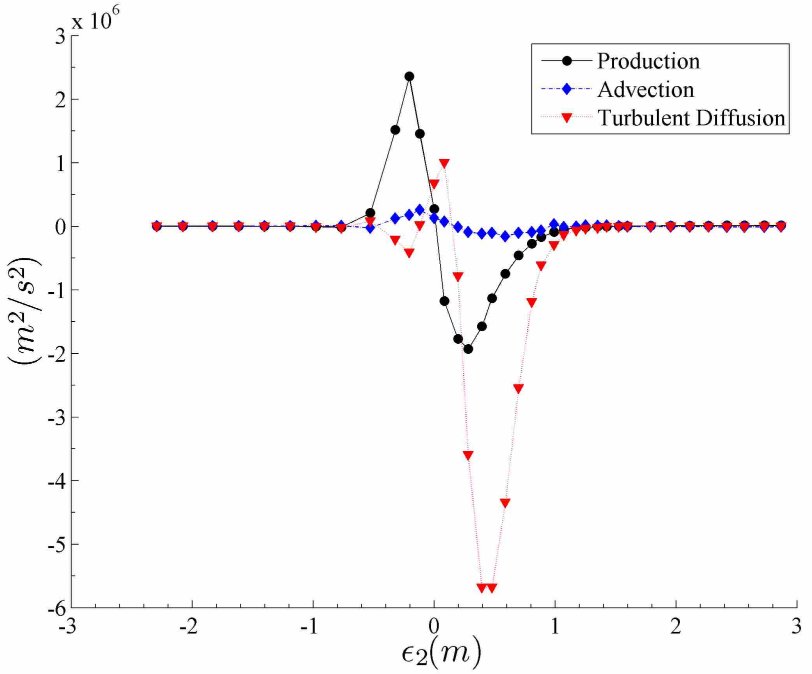

(a)

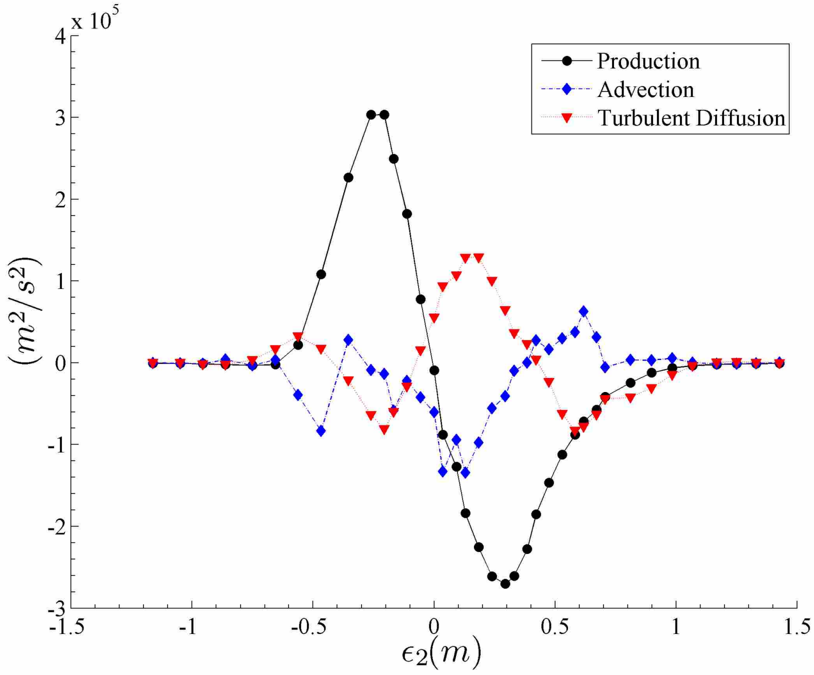

(b)

Figure 4.14: Terms of Transport Equation for $\overline{u' \, v'}$ for (a) ε_1/c = 0.50 and (b) ε_1/c = 1.236

trend. The factors driving this asymmetry in the profiles of $\overline{u'v'}$ however deviate in several ways from those observed in low speed wake research. First, the production of shear stress is dominated by shear terms and not curvature as all terms related to curvature are negligible. Additionally the production term is consistently higher on the convex side of the wake rather than on the concave side. The larger Reynolds shear stresses on the concave side of the wake are therefore not the direct result of production alone; but are driven by a turbulent diffusion term that is generated by the effects of curvature. Thus, the effects of curvature are not made manifest through the production term but that of turbulent diffusion.

The plots of Turbulence Kinetic Energy (TKE), presented in Figure 4.15, show profiles that follow the evolution of the normal stresses from which they were calculated. Comparison of Figures 4.6 and 4.10 indicates that the tangential normal stresses are 80% larger than the streamwise normal stresses at $\varepsilon_1/c = 0.50$. The magnitude of the tangential stresses decays more rapidly relative to the magnitude of the streamwise stresses until they are about equal at $\varepsilon_1/c = 0.825$ and remain so from $\varepsilon_1/c = 0.980$ on. The profiles of TKE (see Figure 4.15) show a transition from a single peak to one with a double peak from the influence of the larger tangential stresses to a two-peak distribution driven by the then dominant streamwise stresses.

Consideration of the components of the Reynolds stress tensor provides an insight into how the turbulence structure of the wake evolves from being dominated by the turbulence created in a separated boundary layer to being driven by the effects of streamline curvature. The normal stresses, $\overline{u'^2}$ and $\overline{v'^2}$, indicate that the effects of the cambered airfoil become less than those of curvature approximately around $\varepsilon_1/c = 0.825$. The shear stresses, $\overline{u'v'}$, became driven by the effects of curvature the earliest at $\varepsilon_1/c = 0.667$. This is in accordance with the observation made by Nakayama [5] that the shear stresses are most sensitive to streamline curvature. The effects of a separated boundary layer shed from a cambered airfoil remains dominant varying distances downstream depending on the turbulence parameter that is being considered.

4.3 Results of the k-ε Simulation

The results of the URANS simulation describe an asymmetric wake with a large amount of decay in mean-value and turbulence parameters as the wake propagates downstream. In the interest of specificity the data set generated using the URANS simulation will be referred to as the

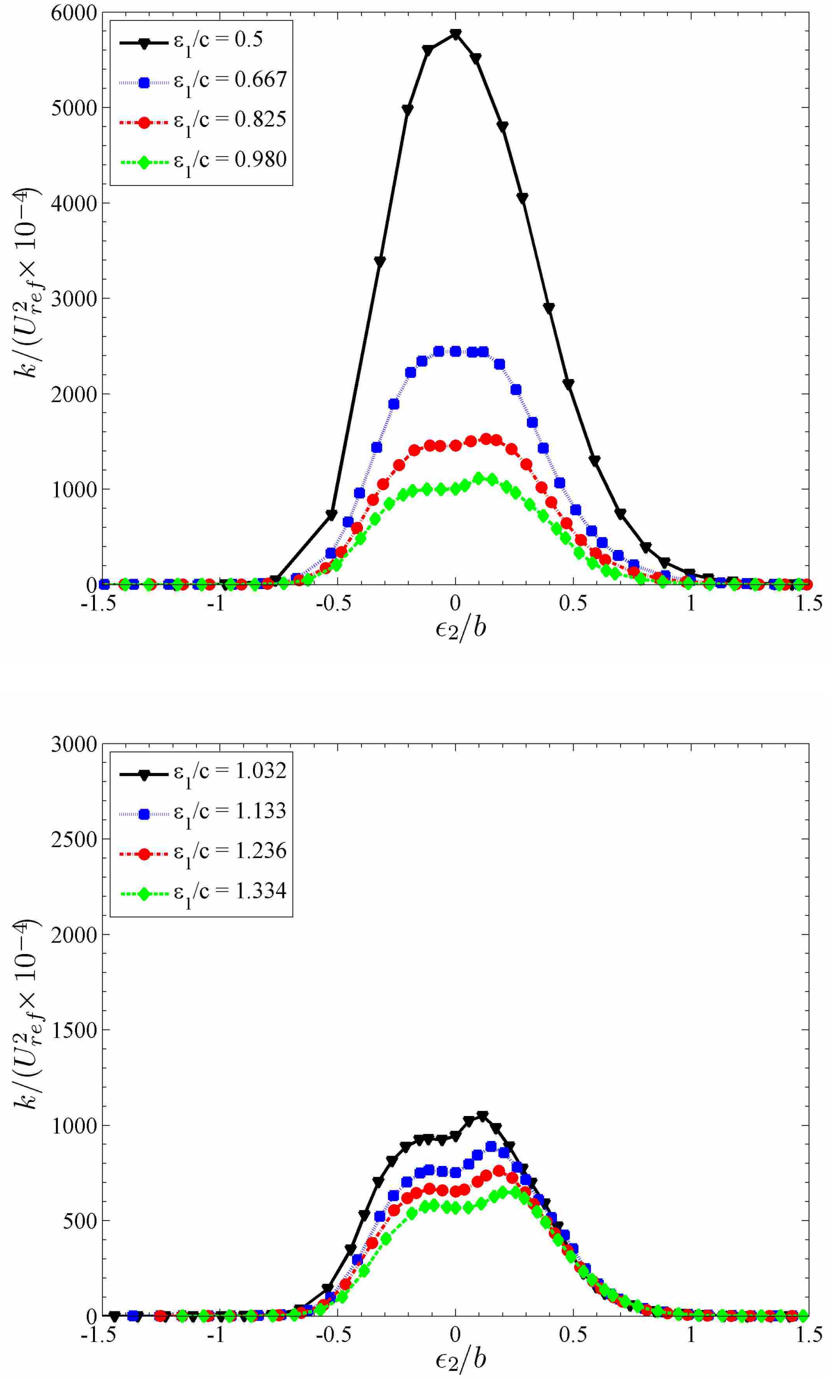

Figure 4.15: Profiles of the Turbulent Kinetic Energy

k-ε data set, as a host of turbulence models may be applied in a URANS simulation. In this section the results are merely presented with minimal discussion and analysis. As many of the results of the k-ε simulation are best understood in the context of comparison with the results of the UDNS, much of the discussion of the following results is conducted in the section where the UDNS and the k-ε data sets are compared.

4.3.1 Mean-Value Wake Parameters

The average velocity profiles vary greatly from ε_2/c = 0.5 to the ε_2/c = 1.334 (see Figure 4.16). The symbols again represent the measured values where as the lines represent the potential velocity. The velocity profile outside the wake for each rake shows a different slope for the concave side than the convex side of the wake. At the later rakes, ε_1/c = 1.032 through 1.334, there is a deceleration observed near ε_2/b = 0.15. The wake width on the concave side is twice as large as it is on the convex side. The larger wake width on the concave side of the wake displays a gradual transition, instead of a clearly defined wake edge, from the velocity profile in the wake region to that of the freestream outside the wake. These features of the velocity profiles, and their causes, will be discussed further in comparison to the UDNS data set. As expected, the wake widens and the mean velocity defect decreases as the wake propagates downstream.

The profiles of velocity defect in similarity variables are shown in Figure 4.17. The k-ε turbulence model captured the asymmetry in the profiles of the mean velocity defect caused by the cambered airfoil that generated the wake. Reflecting the asymmetric wake widths observed in the velocity profiles, the wake width on the concave side is twice as large it is on the convex side. The horizontal axis in Figure 4.17 indicates that the velocity defect is contained within 10% of the wake width b. This is not physical, with the calculated value of b suspect, and is discussed in the comparison of the k-ε and UDNS data sets.

4.3.2 Turbulence Parameters

The distribution of the tangential and streamwise components of the Reynolds stresses are shown, normalized by the square of the reference velocity, in Figures 4.18 and 4.19 respectively. Figure 4.18 shows an asymmetric distribution in the tangential normal stress about the wake cen-

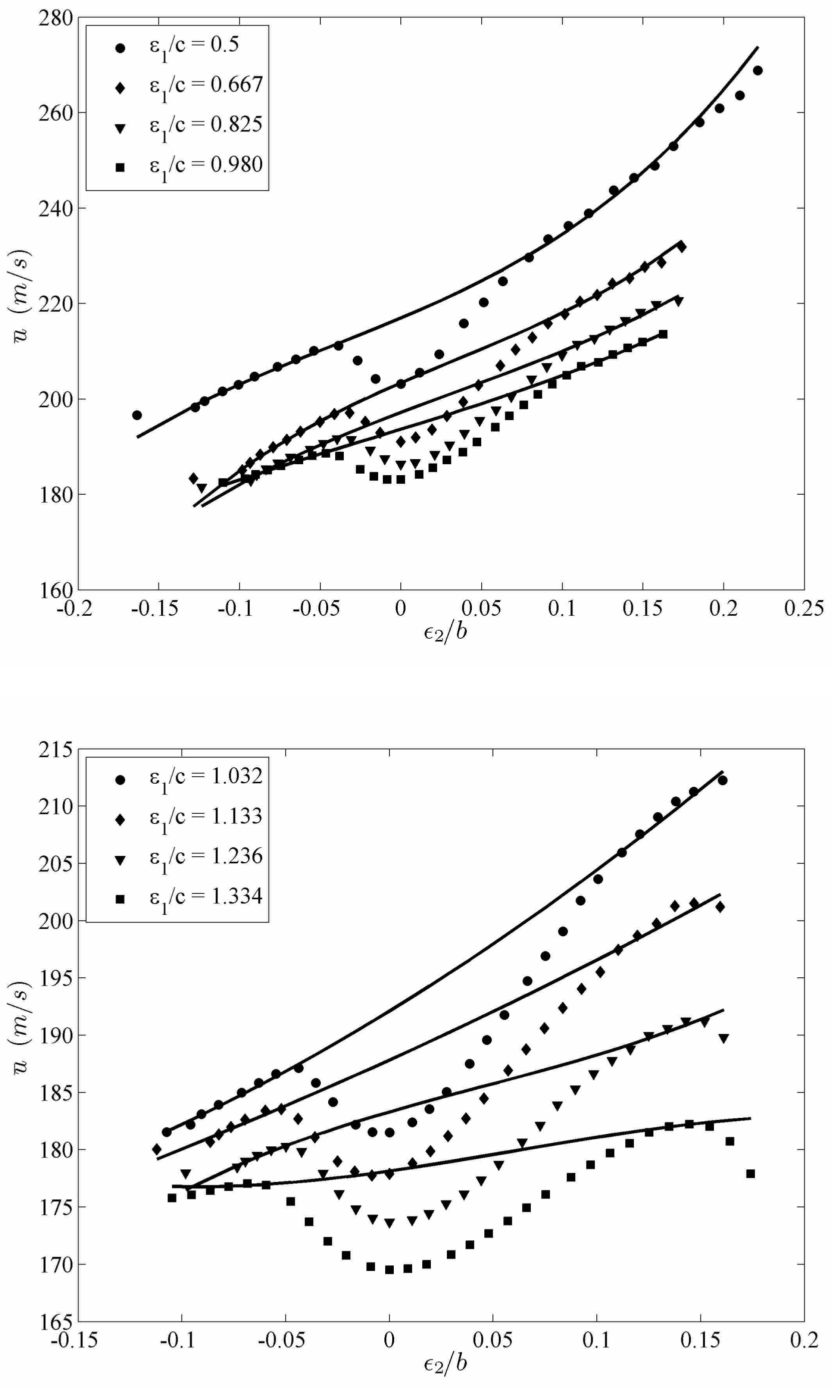

Figure 4.16: The Average Velocity Profiles in the Wake of the RANS Simulation

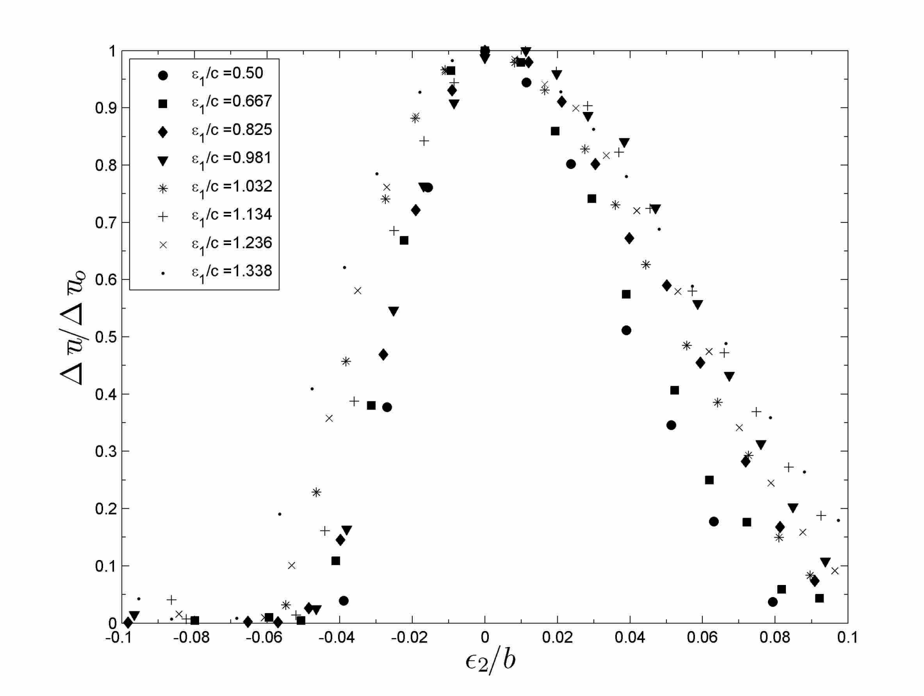

Figure 4.17: Profiles of Velocity Defect from the k-ε Data Set in Similarity Variables

terline with the maximum occurring not at the wake center but at varying distance from the wake center on the concave side from ε_2/b = 0.02 to 0.05. Figure 4.19 shows an asymmetry in the streamwise normal stresses as well about the wake center. Similar to profiles seen in wakes behind symmetric geometries [1, 2], two peaks in stress levels exist each at a maximum shear point, at ε_2/b = -0.02 and 0.05, separated by a valley located at the wake center. The largest of the peaks is located on the concave side of the wake.

An exponential increase in stress levels is observed In both Figures 4.18 and 4.19. This exponential increase does not correspond to turbulence production in the wake. It is therefore the result of an phenomenon external to the wake and will be discussed in comparison to the UDNS data set. The peak magnitudes of $\overline{v'^2}$ are 1.5 to 3 times those of $\overline{u'^2}$. This was explained in the discussion of the UDNS results and was attributed to the separated nature of the boundary layer at the trailing edge of the wake generator.

In an effort to measure the asymmetry in the profiles of the normal Reynolds stresses about the wake center, these stresses were normalized by their value at the wake centerline. Figure 4.20 shows the ratio of the peak tangential stress to be between 1.05 and 2 times the value at the wake

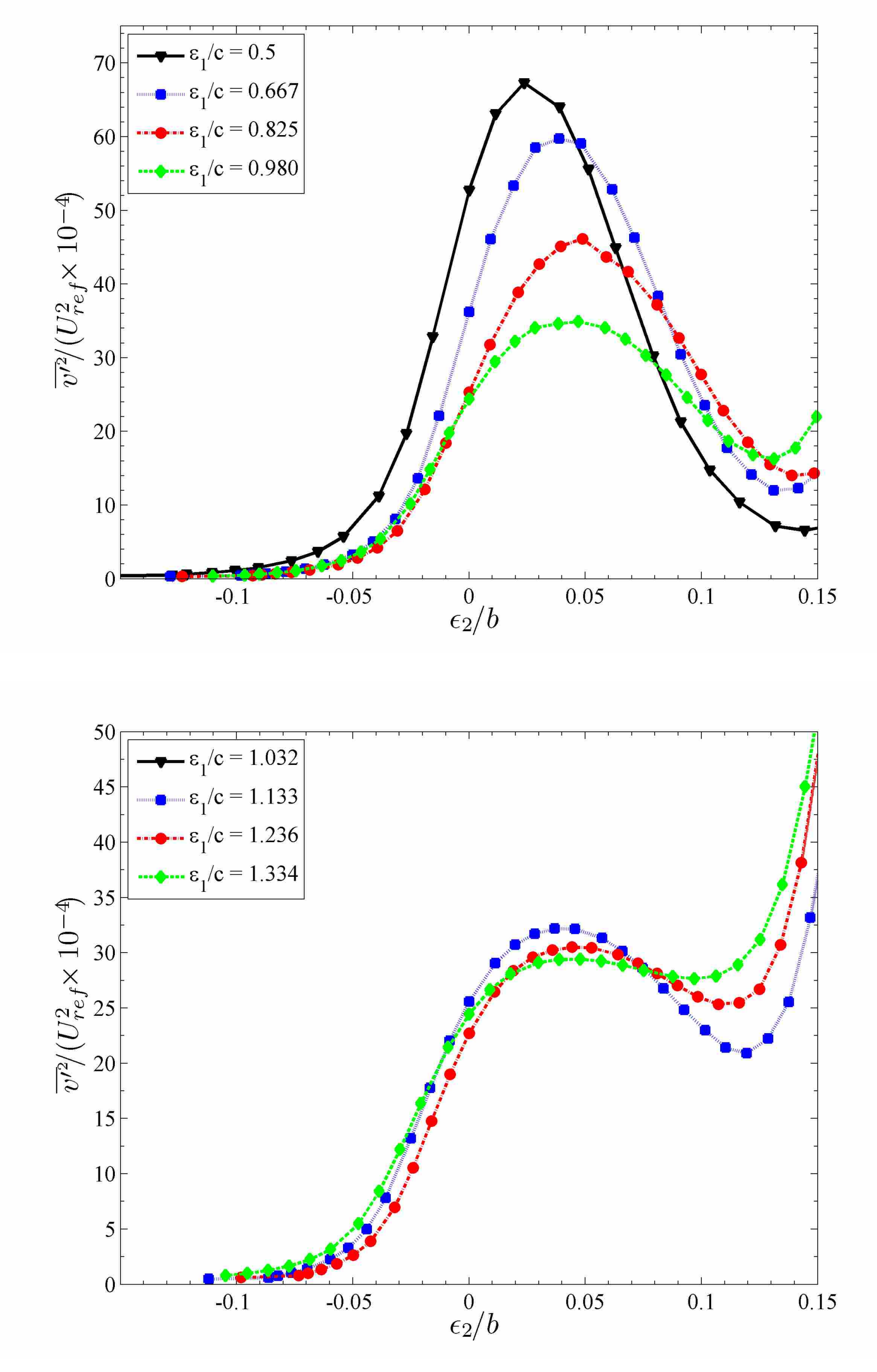

Figure 4.18: Profiles of the Tangential Component of the Reynolds Stresses Normalized by the the Square of the Reference Velocity from the k-ε Simulation

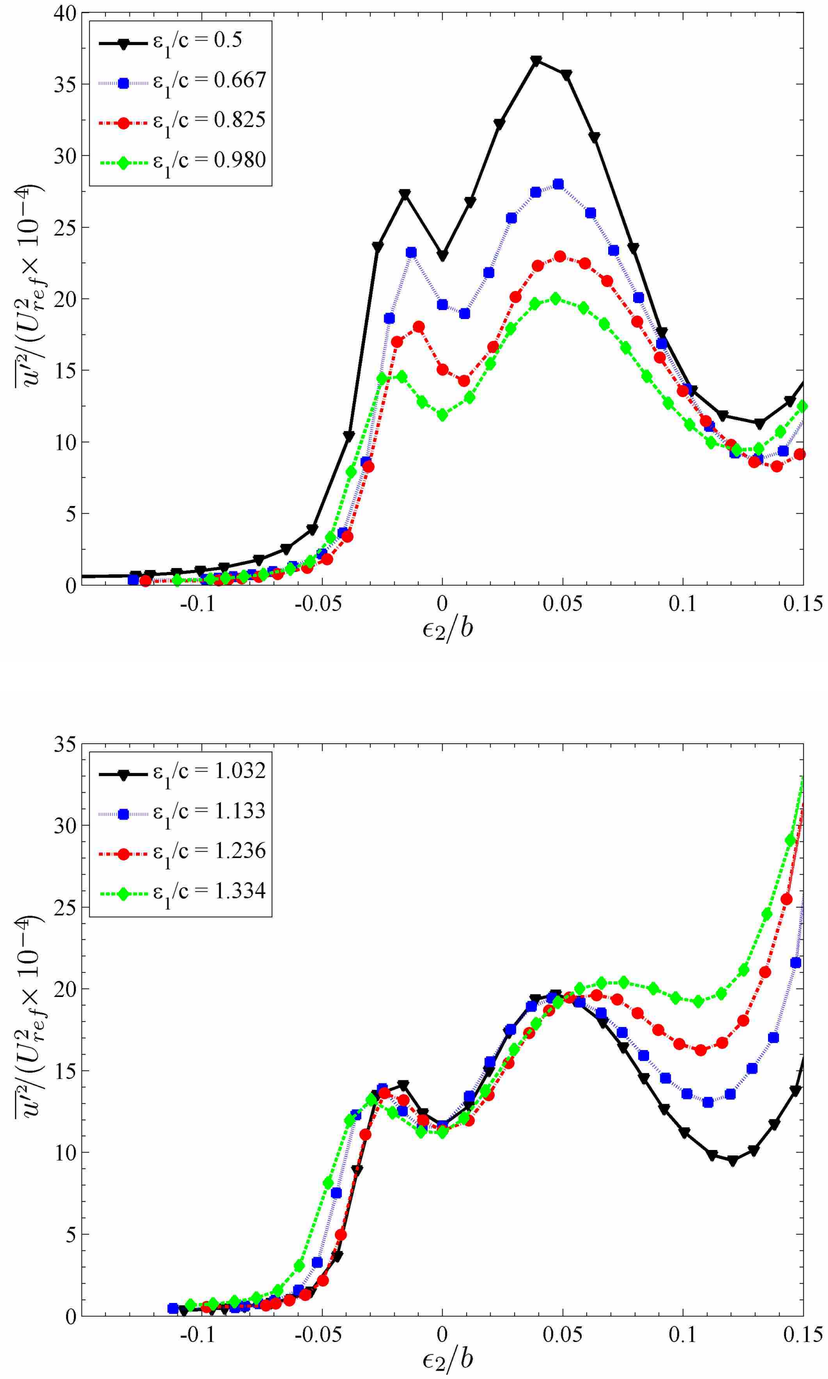

Figure 4.19: Profiles of the Streamwise Component of the Reynolds Stresses Normalized by the the Square of the Reference Velocity from the k-ε Simulation

center. This is considerably larger than the the asymmetry observed in the UDNS data whose maximum value was 1.08 as well as the values reported by John and Schobeiri [1]. The asymmetry in the streamwise stress was somewhat less (see Figure 4.21) with peak values between 1.4 and 1.8. This was also larger than the asymmetry observed in the UDNS data set where the maximum ratio was only 1.4.

The profiles of the Reynolds shear stresses calculated by the k-ε model, normalized by the square of the reference velocity, are shown in Figure 4.22. The peak magnitudes are located approximately at ε_2/b = -0.03 and 0.05. The location of the peak value on the concave side shifts from 0.03 at the first rake to 0.06 at the last. The peak magnitude on each side of the wake decay with increasing ε_1/c. There is a clear asymmetry in the profiles as the peak magnitudes on the concave side of the wake are consistently double those located on the convex.

4.4 Comparison of the UDNS and k-ε Data Sets

The comparison of the UDNS and k-ε data sets illustrates the behavior of the version of the k-ε turbulence model used in PTURBO, which has been tuned to solve turbomachinery flows, as it is applied to modeling transonic wake flow. The following will be discussed in this section. The effects of a large, separated boundary layer on the suction surface of the second blade row were observed in the k-ε data set. As a result, the accuracy with which parameters such as wake width and velocity defect are calculated was reduced. Additionally, the effects of this boundary layer mask the turbulence parameters on the side of the wake nearest to the suction surface of the blade. The turbulence parameters calculated by the k-ε turbulence model are consistently higher than those observed in the UDNS data set. The streamwise turbulence intensity from the k-ε data set was observed to decay more quickly, while the tangential intensity decayed more slowly, than those in the UDNS set. The Reynolds shear stresses are observed to be higher in the k-ε data set than in the UDNS set, though the ratio of the two extrema of the profiles in both data sets is similar.

4.4.1 Observations of the Overall Flow Field

A significant difference between the k-ε and UDNS data sets is the exponential increase observed in the profiles of the normal Reynolds stresses on the far end of the concave side of

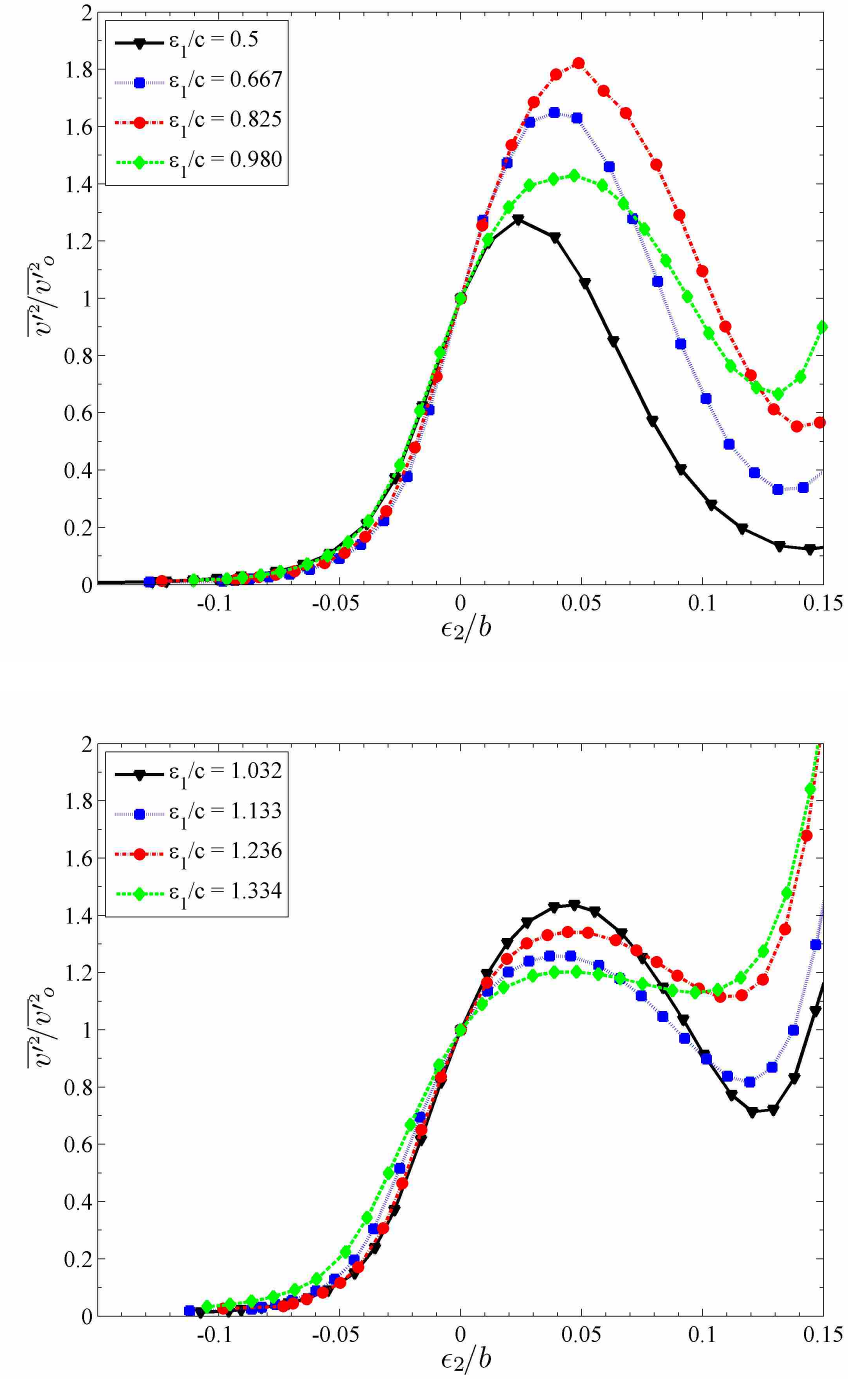

Figure 4.20: Profiles of the Tangential Component of the Reynolds Stresses Normalized by Their Value at the Wake Center from the k-ε Simulation

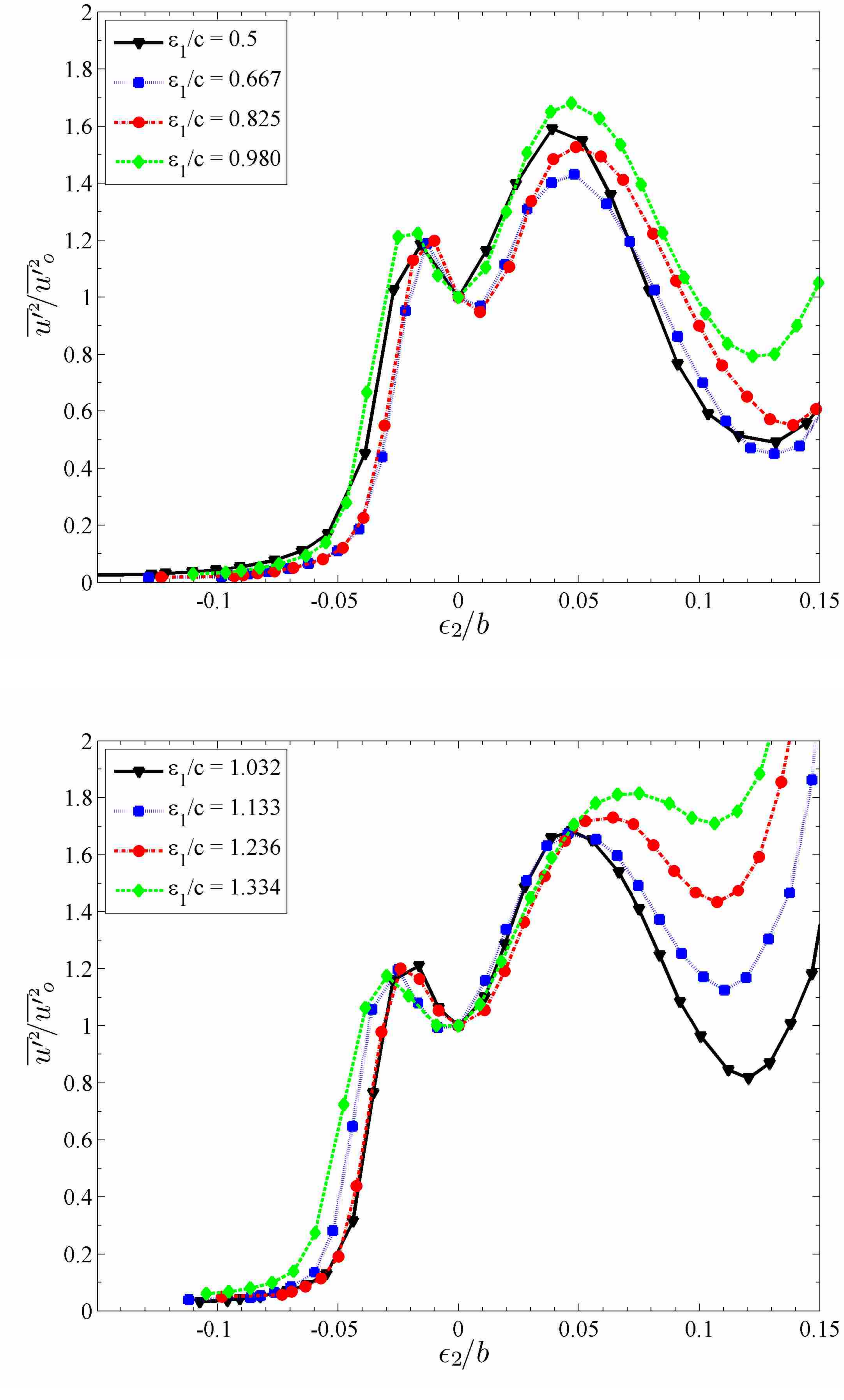

Figure 4.21: Profiles of the Streamwise Component of the Reynolds Stresses Normalized by Their Value at the Wake Center from the k-ε Simulation

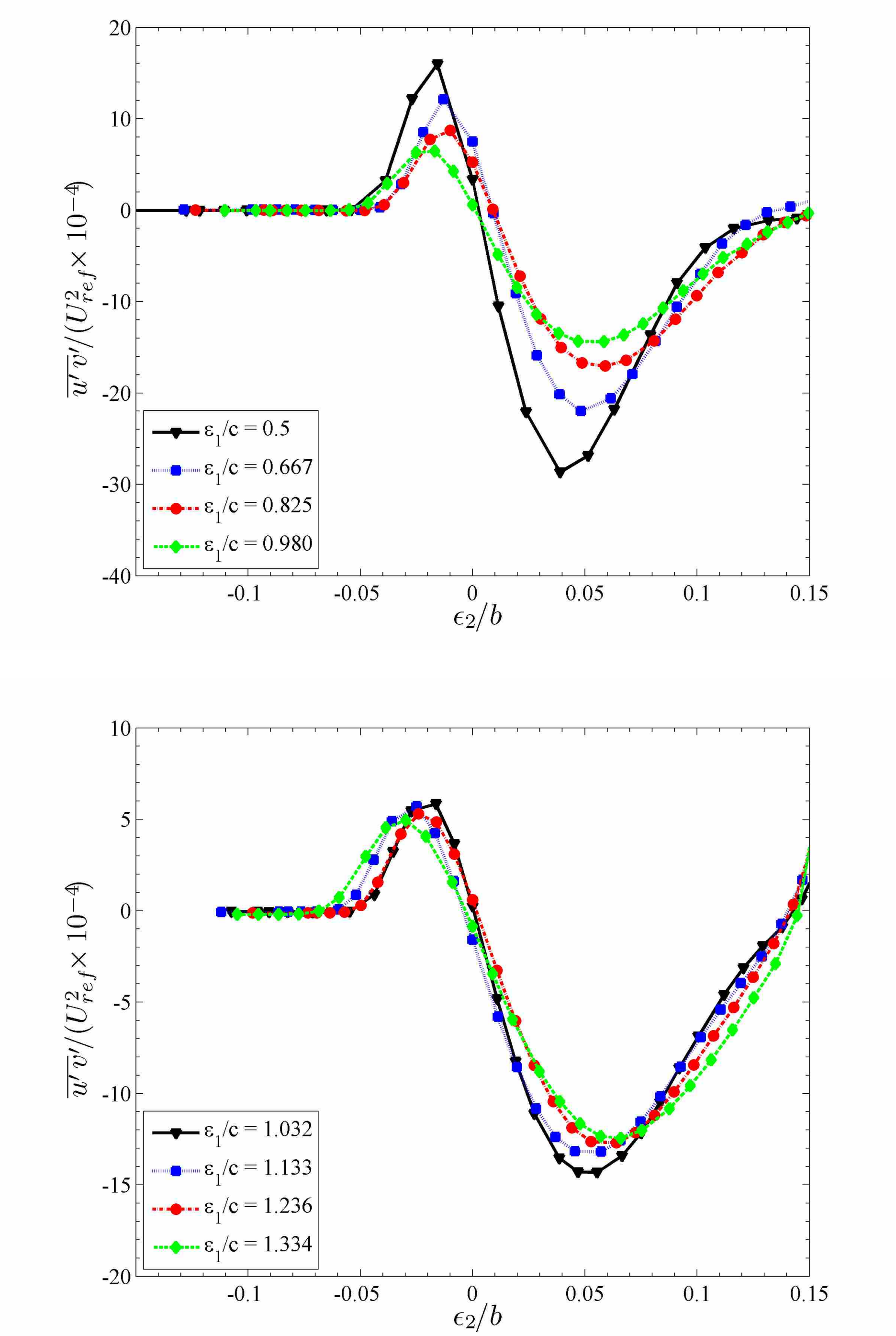

Figure 4.22: Profiles of the Reynolds Shear Stresses from the k-ε Simulation

each rake. Considering the various phenomena occurring in the flow field helps to identify the source of this exponential increase. Figure 4.23 shows instantaneous snapshots of the contours of normalized entropy flux and depicts the evolution of the structures in the flowfield during one wake passing period. Comparing the boundary layers on the suction side of the second blade row from the UDNS and that from the k-ε simulation it can be seen that the separated region in the k-ε simulation is significantly larger than the region shown in the UDNS. This large boundary layer is in close proximity to the wake in the area downstream of the throat of the blade row. The passing regions of separation cause large fluctuating velocities on that side of the wake, as shown in Figures 4.18 and 4.19 and thus acts as an external source of turbulence. This yields the higher turbulent stresses on that side of the wake. Higher turbulence intensities affect the k-ε turbulence model as the model uses the transport equation of k, which is directly related to the turbulence stresses, and that of ε to help solve the closure problem (see Equations 4.2 and 4.3). Since the turbulence stresses near the wake are increased by the passing separation zones; the turbulence stresses are affected as well through the modeling of the transport of k. The expansion of the area where the effects are seen is documented in Figure4.19. At $\varepsilon_1/c = 0.50$, the area affected by the boundary is observed to be limited to the very edge of the wake. By $\varepsilon_1/c = 1.334$ the growth of the wake width and the boundary layer cause that the effects of the boundary layer are seen very near the wake center (see Figure 4.18).

Several other useful observations may be made from Figure 4.23. At first glance, it is readily observable that the wake from the k-ε data is wider than that from the UDNS. By analyzing the evolution of the vortical structure more details regarding this difference in wake size may be gleaned. In each data set, or in each column, a single vortical structure is identified and followed as it propagates through the blade passage. This structure was circled in the images to help observe how it evolves. Both data sets show the vortical structure grows more in the concave side of the wake than in the convex. The magnitude of this growth however is significantly different. The blade to blade coordinate is shown on the left of each image. Using the edge of the vortical structures in the region where the wake is straight and horizontal in the image to define the edges of the wake the amount of growth in the convex and concave directions may be approximated. Both wakes share a similar blade to blade coordinate of 0.065 to 0.067 for their convex side. Their coordinates for the concave sides are however significantly different. The concave wake edge in

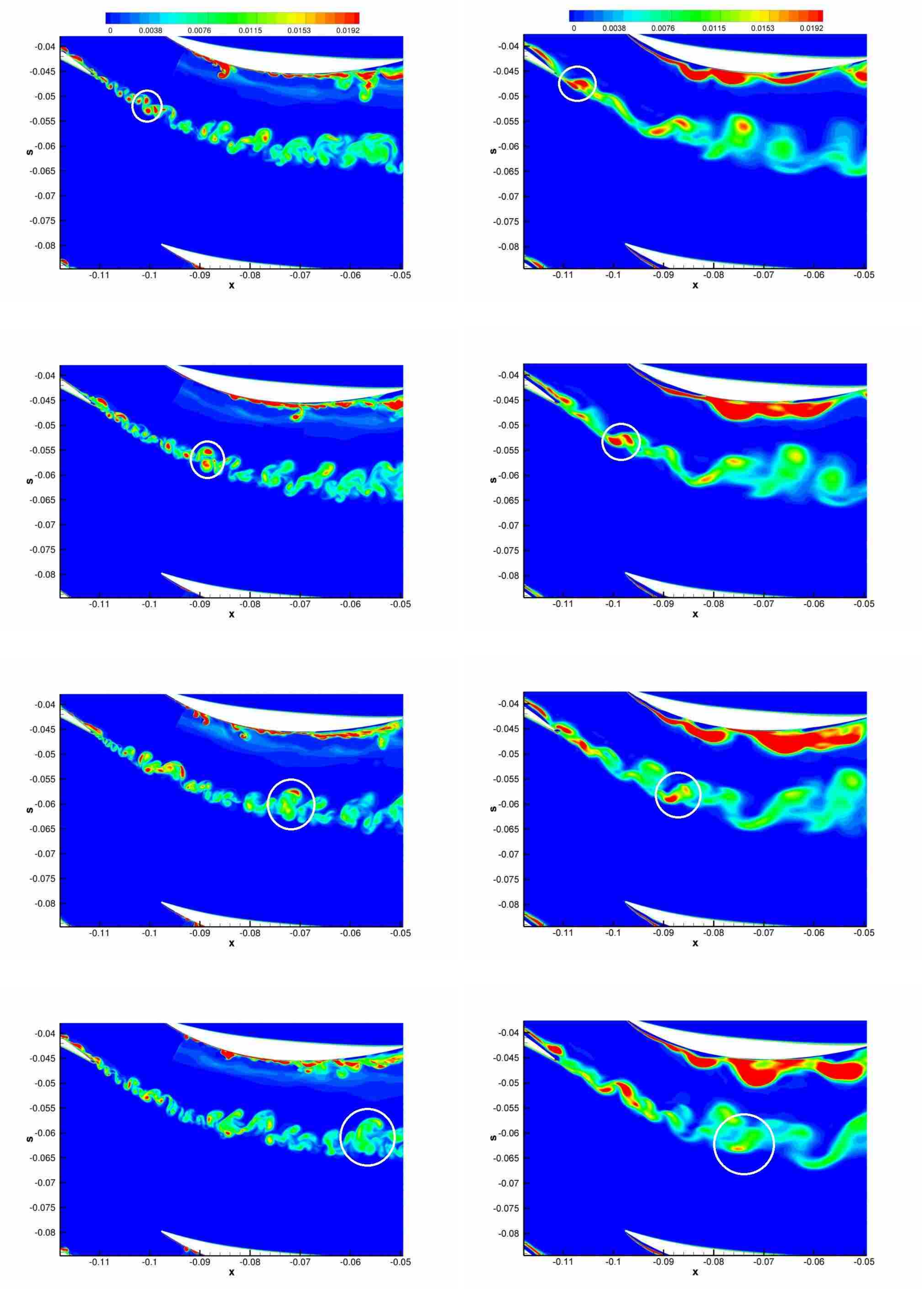

Figure 4.23: Contours of Normalized Entropy Flux from the UDNS (Left Column) and the k-ε Simulation (Right Column)

the UDNS is between s = 0.055 and 0.06 while the same wake edge in the k-ε data set is located between s = 0.05 and 0.055. This indicates that the two wakes grow similarly in the convex direction while the k-ε grows more in the concave direction than the UDNS.

$$\begin{aligned}
\frac{\partial k}{\partial t}+U_j\frac{\partial k}{\partial x_j} &= \tau_{ij}\frac{U_i}{\partial x_j}-\varepsilon+\frac{\partial}{\partial x_j}\left[(\nu+\nu_T/\sigma_k)\frac{\partial k}{\partial x_j}\right] && (4.2)\\
\frac{\partial \varepsilon}{\partial t}+U_j\frac{\partial \varepsilon}{\partial x_j} &= C_{\varepsilon 1}\frac{\varepsilon}{k}\tau_{ij}\frac{U_i}{\partial x_j}-C_{\varepsilon 2}\frac{\varepsilon^2}{k}+\frac{\partial}{\partial x_j}\left[(\nu+\nu_T/\sigma_\varepsilon)\frac{\partial \varepsilon}{\partial x_j}\right] && (4.3)
\end{aligned}$$

In order to gain insight into the behavior of the k-ε, the effects of the separated boundary layer on the second blade row must be separated. This is accomplished by determining how far into the wake they extend. Figures 4.24 and 4.25 show the terms of the transport equations for $\overline{u'^2}$ and $\overline{v'^2}$ respectively at ε_1/c = 0.980 and 1.032. Since the separated boundary layer acts as an external source of turbulence, its effects would appear as turbulence that is advected or diffused into the wake. This would take the form of large negative advection terms or large positive diffusion terms. In Figure 4.24(a), the advection and diffusion terms are both smaller than the production term. In Figure 4.24(b), an advection term that is twice as large at the production term and five times as large as its value at the previous rake is observed on the far end of the concave side of the rake. Similar behavior is observed in the tangential Reynolds stress (see Figure 4.25). These large advection terms represent the transport of Reynolds stresses in to the wake area from the separated boundary layer. These plots indicate that the boundary layer begins to influence the behavior of the k-ε turbulence model on the wake at ε_1/c = 1.032. By analyzing the rake before ε_1/c = 1.032, the behavior of the k-ε model can be observed without the effects of the separated boundary layer interfering. In order to be sure of the absence of boundary layer effects, only the first two rakes, ε_1/c = 050 and 0.667, will be considered in the comparison of the two data sets.

In a tangential note, the source of the separation occurring in the boundary layer on the suction side of the second blade row may be revealed in the contours from the UDNS (see Figure 4.1). There is a source of entropy observed close to the suction surface of the blade at approximately quarter chord. Upon verifying contours of local Mach number, density, temperature and pressure it was confirmed that this is a weak shock wave that is not fully resolved in the grid of the k-ε simulation. This shock wave causes the boundary layer in the UDNS to separate, as seen by the separated vortical structure located just downstream from it. Though this shock wave is not observed in the contours of entropy flux from the k-ε simulation it is observable in the contours of Mach number (see Figure 4.27). The contours of Mach number from the UDNS show a sharp deceleration from sonic to subsonic speeds in the same area as the source of entropy was observed in the contours of entropy flux. Though no source of entropy is observed in the k-ε contours a similar deceleration is present in the same area in the contours of Mach number for the k-ε data. This is the reason for which the boundary layer separates and grows though no entropy source is observed.

Figure 4.26 shows the average velocity profiles, at $\varepsilon_1/c = 0.50$ and 0.825, from both data sets. In the UDNS, the profile outside of the wake on the concave and convex side share a similar linear slope. The data from the k-ε set do not share this quality. In Figure 4.26 the slope of the profile outside of the convex side is less than that beyond the edge of the wake on the concave side for the k-ε data set. Considering the contours of Mach number in Figure 4.27 indicates that the source of this difference is the presence of the shock wave. In Figure 4.27(b), the area downstream of the shock wave exhibits minimal reacceleration. The UDNS rake at $\varepsilon_1/c = 0.50$ therefore sees less acceleration than the k-ε rake at the same streamwise coordinate since Figure 4.27(a) shows significant reacceleration in that area. This variability in the velocity profiles outside the wake results in a poor fit of the potential velocity. Another factor that contributed to the poor fit of the potential velocity in the k-ε data set is the lack of a clearly defined wake edge in the profiles of that data set (see Figure 4.27). The profiles from the UDNS show a clear inflection point where the wake and the freestream meet. The profiles from the k-ε data show instead a smooth transition from the wake to the freestream. The lack of this wake edge makes the decision of what data to fit the potential velocity curve through rather arbitrary. Figure 4.26 also shows that the maximum velocity defect calculated by the k-ε model is less than the defect observed in the UDNS data. This trend will be quantified in the following discussion of the decay of the velocity defect.

The calculated wake width is shown in Figure 4.28(b). The width calculated from the k-ε data varied from 53 mm to 78 mm which is 15 to 20 times the width calculated from the UDNS data. The contours of entropy in Figure 4.23 show that the wake is larger in the k-ε data than it is in the UDNS data. However, a wake width of 50 mm to 80 mm is unphysical as it implies the wake is significantly larger than the blade passage containing it which measures only 40 mm in the tangential direction. This artificially high wake width caused the horizontal axis of the figures showing the profiles of the k-ε data in this chapter to indicate that the majority of the wake occurs in less than 10% of the wake width b of the center line. This is in comparison to the UDNS where the wake is contained within a value of one wake width. This difference in the wake width appears to be scalar in nature as the similarity curve from the UDNS and that from the k-ε data sets show that the wake is twice as wide on the concave side than on the convex side. Due to the poor quality of the potential velocity, the length scale of b, is not accurate nor appropriate to use in the comparison of the two data sets. The data used to compare the two sets will thus be plotted using only the distance from the wake center (ε_2).

Figure 4.28(a) shows the decay of the maximum velocity defect for the UDNS and k-ε data sets. The observation of the k-ε yielding a lower velocity defect is confirmed in Figure 4.28(a) where the difference between the defect calculated in the UDNS and that from the k-ε is between 3.77 and 4.5 m/s, or 21 and 30% of the UDNS value at each rake. Since the difference between the maximum defect from each data set varies no more than 10%, the k-ε turbulence model accurately predicted the decay rate as was observed by Tulapurkara, Ramjee, and George [2]. The oscillating maximum velocity defect in the later rakes is a result of the quality of potential velocity curve fit.

4.4.2 Turbulence Parameters

The UDNS and k-ε data sets show different turbulence structures of the wake. These differences vary from the magnitude of the various components of the Reynolds stresses to the decay rates of these stresses. The effects of these differences in the turbulent structures are made manifest in the time average profiles of the wake. Figure 4.29 shows the profiles of $\overline{u'^2}$ from the rakes at $\varepsilon_1/c = 0.50$ and 0.667 from both data sets. A key difference noted between the profiles of the two data sets is that between the transition from a single peak distribution seen in the data from the UDNS and the consistent two-peak distribution observed in the k-ε data. As stated in the analysis of the UDNS data, the single peak distribution is the result of the turbulence created by a separated boundary layer at the trailing edge of the wake generator. Since the same geometry created the wake in the k-ε simulation as in the UDNS, it must therefore be that similar turbulence is created behind the wake generator in both data sets. This turbulence however has been transported out of the wake faster in the k-ε data than the UDNS as the profile of $\overline{u'^2}$ shows an asymmetric two-peak profile by $\varepsilon_1/c = 0.50$. This theory is confirmed by considering the decay rates of $\overline{u'^2}$ from both data sets (See Figure 4.30). For the rakes that have been identified to show wake profiles independent of the effects of the separated boundary layer on the second blade row, it can be seen that the peak values of $\overline{u'^2}$ in the k-ε data decay at a faster rate than those from the UDNS data set. A log fit to the two curves indicates that the values from the UDNS decay with an exponent of -.672 while the exponent for the k-ε curve is -0.815. Therefore, it can be observed that the k-ε model underpredicts the streamwise distance over which the effects of a cambered airfoil dominate the turbulent structure of the wake.

Figure 4.29 indicates that the magnitude of the streamwise Reynolds stresses are larger in the k-ε data set than in the UDNS data. The ratio of peak magnitude from the k-ε data to that from the UDNS indicates that the k-ε model predicts stresses 15% and 10% greater than those from the UDNS at $\varepsilon_1/c = 0.50$ and 0.667 repsectively. The decreasing trend in this ratio corresponds to the higher decay rate in the k-ε that was just discussed. Also significant is the location of the peak values on each side of the wake center. The peak values from both data sets on the convex side occur near the same distance from wake centerline. The peaks on the concave side in the k-ε data occurs at at significantly larger distance from the wake center than those from the UDNS data (3 mm compared to 1 mm to be exact).

The terms of the transport equation give insight in to the source of the differences between the two profiles of $\overline{u'^2}$. Figure 4.31 shows the production, advection, and turbulent diffusion terms for $\overline{u'^2}$ for both data sets at $\varepsilon_1/c = 0.667$. Both data sets show advection and diffusion to dominate near the wake center while not affecting a large peak in production on the concave side of the wake. The locations of the peaks in production correspond to the location of the peaks in $\overline{u'^2}$ as seen in Figure 4.29. The profiles of $\overline{u'^2}$ therefore are driven by these production terms. The peak production value on the concave side in the k-ε data is 70% greater than the peak value on the same side of the wake in the UDNS data set. On the convex side however, the k-ε predicts a peak production value that is 50% less than the same peak in the data from the UDNS. The increase of production on the concave side and the accompanying decrease on the convex side is the result of the k-ε model overpredicting the effects of curvature on production. Two components of the production term in Equation 3.5 are responsible for the profile of production. The first is the shear term which is of similar magnitudes in both data sets. The second is the term solely associated with the radius of curvature. This curvature term is four times larger in the k-ε data set than it is in the UDNS data. As a result, this term overly enhances the peak of production on the concave side while overly reducing the peak on the convex side. This is the root cause for the overprediction by the k-ε turbulence model of the effects of curvature on the profiles of $\overline{u'^2}$. Tulapurkara, Ramjee, and George [2] also documented the overprediction in asymmetry in a low-speed curved wake behind a symmetric airfoil. This overprediction of the asymmetry translates into the k-ε models predicting exaggerated mixing of the wake in the streamwise direction on the concave side.

There are several differences between the profiles of $\overline{v'^2}$ from the k-ε and the UDNS (see Figure 4.32). The first is that the k-ε model predicts peak magnitudes that are 40% and 50% greater than those from the UDNS data set at $\varepsilon_1/c = 0.50$ and 0.667 respectively. This increasing ratio indicates that $\overline{v'^2}$ decays more rapidly in the UDNS data set than in the k-ε data. This is confirmed by Figure 4.33 which shows the decay of the peak values of $\overline{v'^2}$ from both data sets. A log fit of the two curves shows that the DNS data set decays with an exponent of -1.236 while the exponent of the k-ε data is -.941. Figure 4.32 also shows that the peak value in the k-ε data shifts farther to the concave side as the wake propagates downstream. The UDNS however shows the peak to remain near the wake center. Consideration of the terms of the transport equation helps to understand the source of the shift in location of the peak value observed in the k-ε data (see Figure 4.34). Figure 4.34(a) shows that the UDNS has a symmetric profile of the diffusion term about the wake center. This profile results in the peak being located near the wake center. Figure 4.34(b) shows that the k-ε data has an asymmetric profile with a dominant peak on the concave side. This causes the peak value to occur near that peak in diffusion as all three terms collaborate to decrease the levels of $\overline{v'^2}$ located near the wake center.

The k-ε simulation predicts a higher amount of turbulence kinetic energy than the UDNS. The ratio of maximum TKE in the k-ε simulation to the UDNS ranges from 2 at $\varepsilon_1/c = 0.50$ to 3 at $\varepsilon_1/c = 1.334$. This increase the ratio of TKE from each data set arises from the increasing peak values of $\overline{v'^2}$ in the k-ε simulation that are due to the effects of the separated boundary layer that mask the turbulence of the wake.

The profiles of TKE in the UDNS and in the k-ε simulation (see Figure 4.35) reflect how the magnitudes of $\overline{u'^2}$ and $\overline{v'^2}$ relate to each other as well as the decay of each in the UDNS and the k-ε data sets. Since $\overline{v'^2}$ dominates $\overline{u'^2}$ in the UDNS at $\varepsilon_1/c = 0.50$ and since $\overline{u'^2}$ exhibits a single peak distribution, both are results of the cambered airfoil used to generate the wake, the profile of

TKE at that streamwise position shows a single peak. The profile at $\varepsilon_1/c = 0.667$ indicates that the profiles of TKE are by then being driven by $\overline{u'^2}$. This is due to the fact that $\overline{v'^2}$ decays faster than $\overline{u'^2}$ in the UDNS data set. The data set from the k-ε simulation indicate the opposite trend. The profile clearly follows the trends observed in the profiles of $\overline{v'^2}$ (see Figure 4.32). This is the result of $\overline{v'^2}$ dominating $\overline{u'^2}$ at the first rake, similar to the UDNS data set. Differing from the UDNS data however, $\overline{u'^2}$ decays more rapidly than $\overline{v'^2}$ leaving it dominant. This also deviates from the observations of Tulapurkara, Ramjee, and George [2] that several variants of the k-ε turbulence model show the profiles of TKE to be driven by $\overline{u'^2}$ in a low-speed curved wake behind a symmetric airfoil.

As the Reynolds shear stresses are mechanism by which streamwise momentum is turbulently transported in the tangential direction from the wake center, they play a significant role in forming the time-averaged profiles of the wake. Figure 4.36 illustrates two key differences between the shear stresses in the UDNS and k-ε data sets: the magnitude and location of the peaks in shear stresses. The peak values on both sides of the wake are three times larger in the k-ε data than in the UDNS data. Figure 4.37 shows the decay of the extrema of shear stress values for each rake of the UDNS as well as the k-ε data sets. The ratio of the shear stresses maintains the value of three for all the rakes considered in this comparison. The larger shear stresses observed in the k-ε profile result in a larger wake width and the lack of a clearly defined wake edge on the concave side of the wake (see Figure 4.26). The ratio of the extreme values from each side of the wake shares a similar value of two for both data sets. The shear stresses in the k-ε data are therefore scaled by a constant in relation to the values from the UDNS data set indicating that the turbulence model accurately predicted the asymmetry in the shear stresses.

The second difference observed in Figure 4.36 is the location of the peak values on each side of the wake. The profiles on the convex side of the wake show a similar location for the peak values. On the concave side however, there is a discrepancy between the k-ε data and those from the UDNS. The k-ε data set shows the peak on the concave side of the wake to be 2 mm to 3 mm away from the wake center whereas the UDNS data shows the peak to be located at 1 mm from the center. This difference between the convex and concave sides explain the previous observations made from the contours of entropy flux. The wake in both data sets share similar track for the convex side but the k-ε data shows a significantly larger wake width on the concave side. The larger shear stresses located farther away from the wake center indicate the transport of streamwise momentum occurs at greater amounts and farther away in the k-ε data than in the UDNS. Also connected to this observation are the larger levels of $\overline{u'^2}$ located farther than even the peak values of the shear stresses.

Figure 4.38 indicates the reason behind the elevated shear stress values in the k-ε data set. Turbulent diffusion is seen to be the driving mechanism for the shear stresses for both sides of the wake in the k-ε data(see Figure 4.38(b)). This differs from the profiles of the UDNS in Figure 4.38(a) where the concave side is driven by diffusion but the convex side is dominated by production. The peak diffusion term on the concave side of the k-ε data is more than an order of magnitude larger than the same peak in the UDNS data set. The similar peak in $\overline{u'v'}$ on the convex side is the result of the fact that the diffusion term in the k-ε data set shares a similar location with the production peak in the UDNS data and is only twice as large. Since curvature the term that drives the diffusion is that related to curvature, it is be observed that the k-ε model overpredicts the effect of curvature on $\overline{u'v'}$.

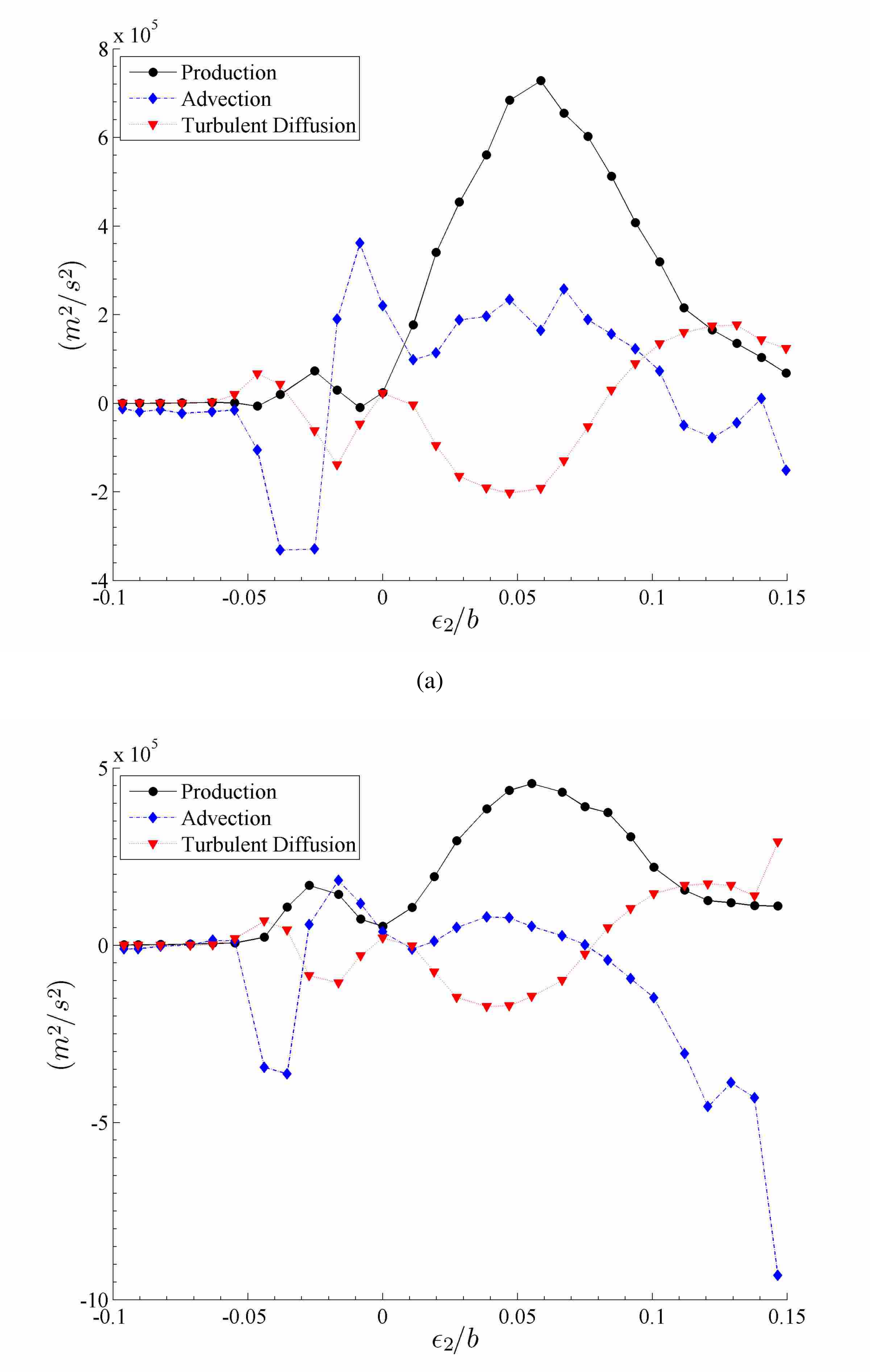

(a)

(b)

Figure 4.24: The Terms of the Transport Equation for $\overline{u'^2}$ at (a) ε_1/c = 0.980 and (b) ε_1/c = 1.032

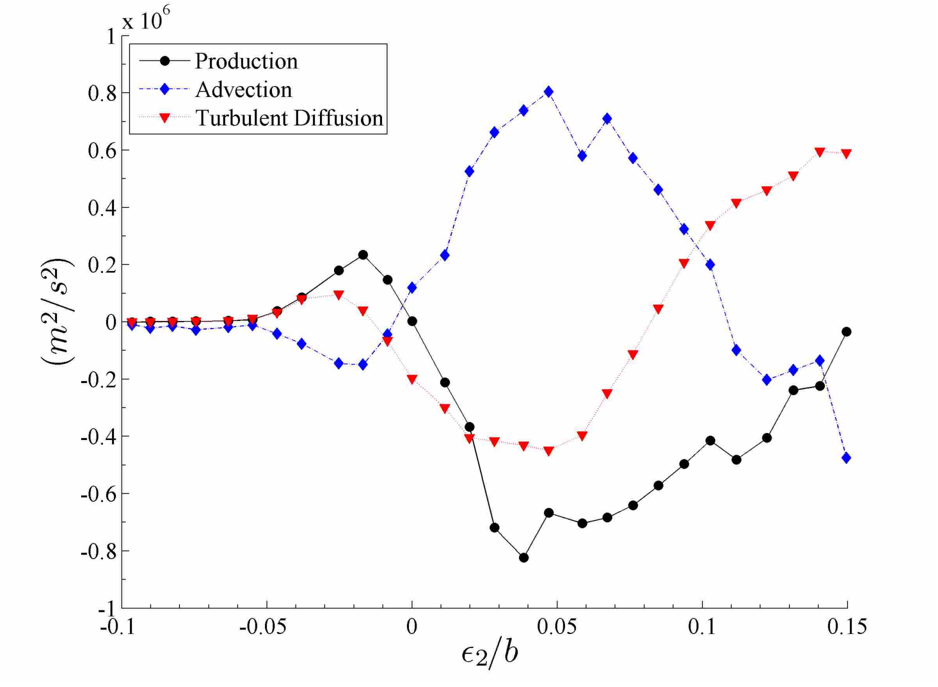

(a)

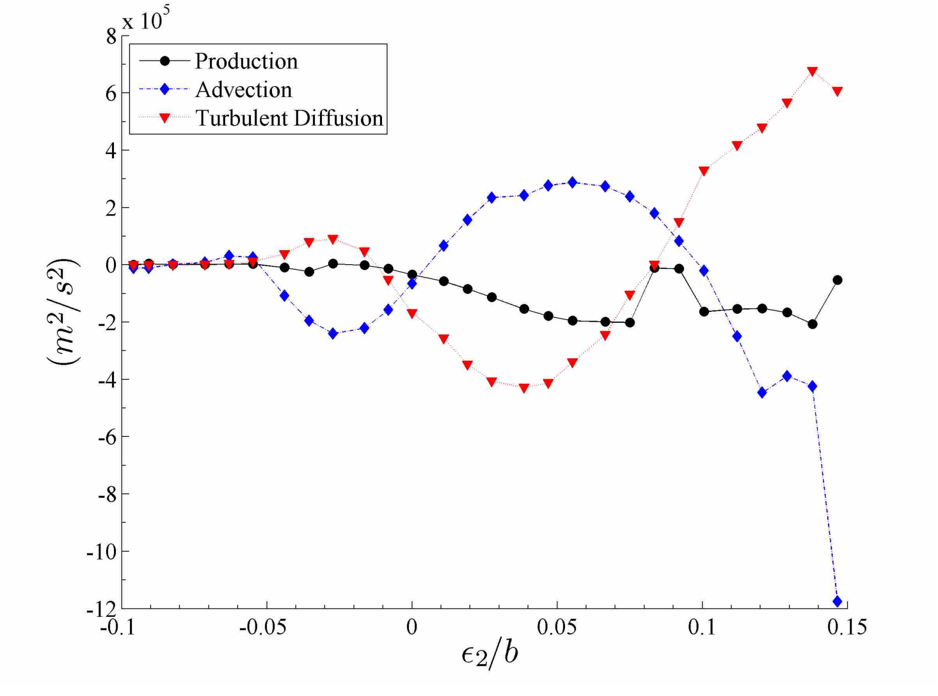

(b)

Figure 4.25: The Terms of the Transport Equation for $\overline{v'^2}$ at (a) ε_1/c = 0.980 and (b) ε_1/c = 1.032

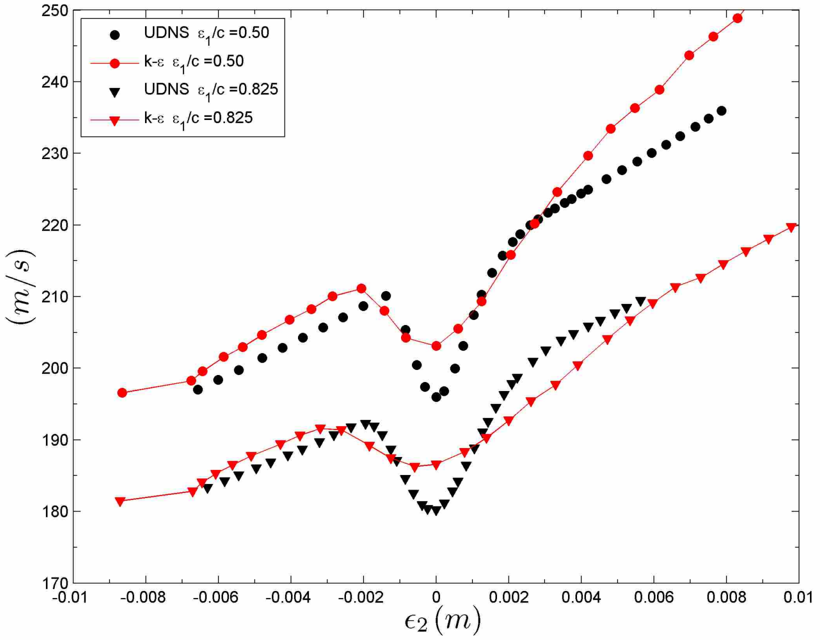

Figure 4.26: Comparison of the Average Velocity Profiles from the UDNS and k-ε Data Sets

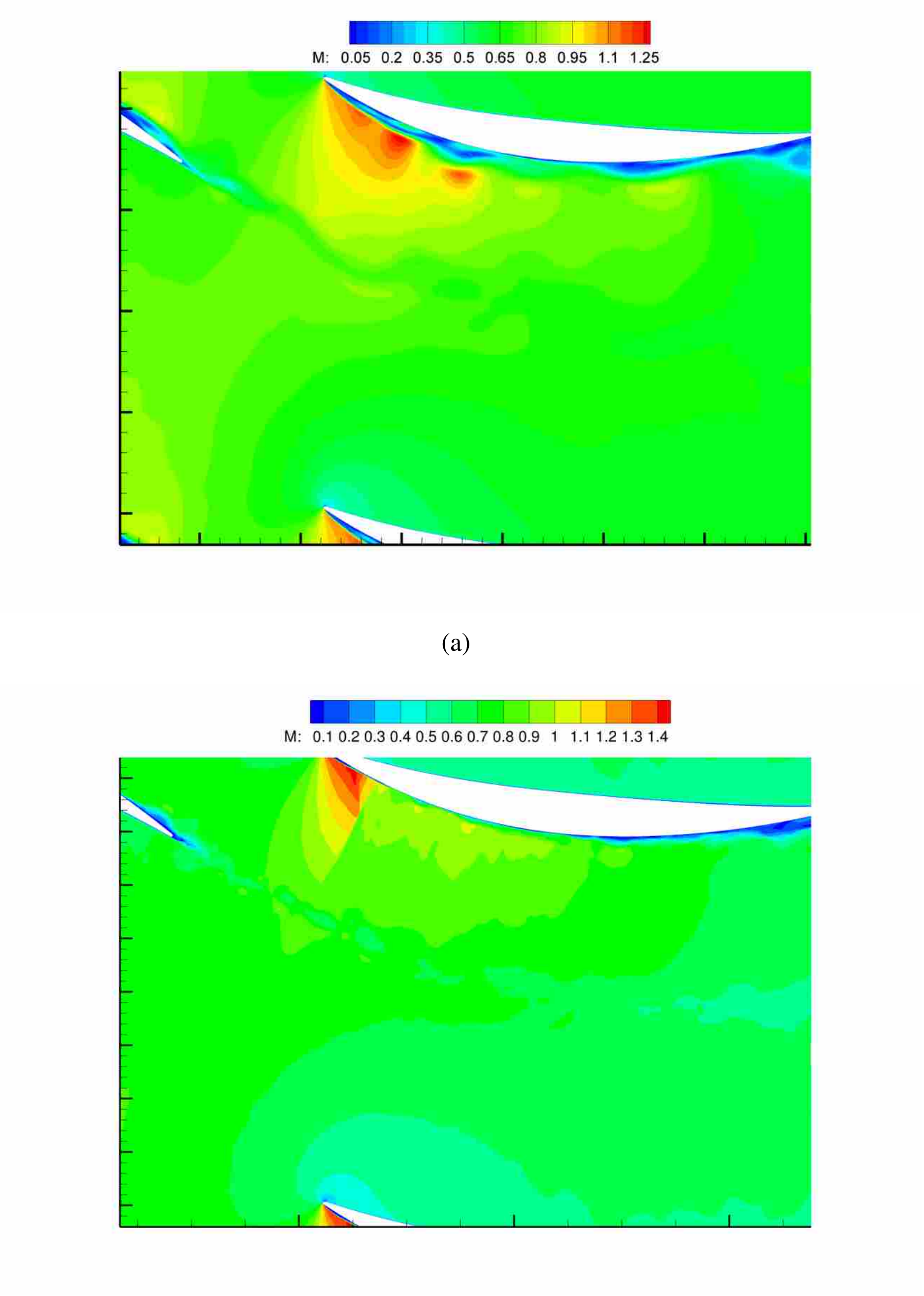

(a)

(b)

Figure 4.27: Contours of Unsteady Mach Number from (a) the k-ε Simulation and (b) the UDNS

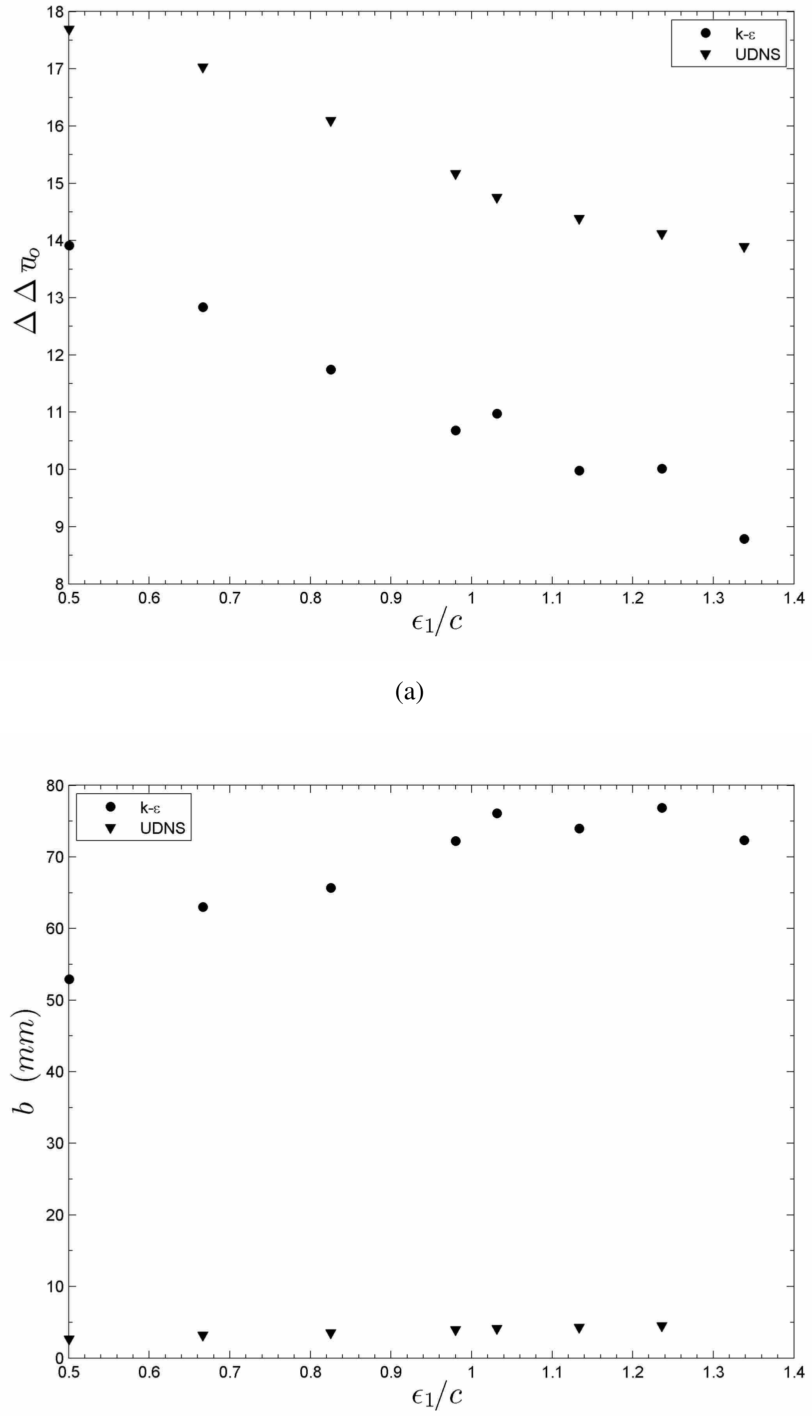

(a)

(b)

Figure 4.28: (a) The Maximum Velocity Defect and (b) the Wake Width for the UDNS and k-ε Data Sets

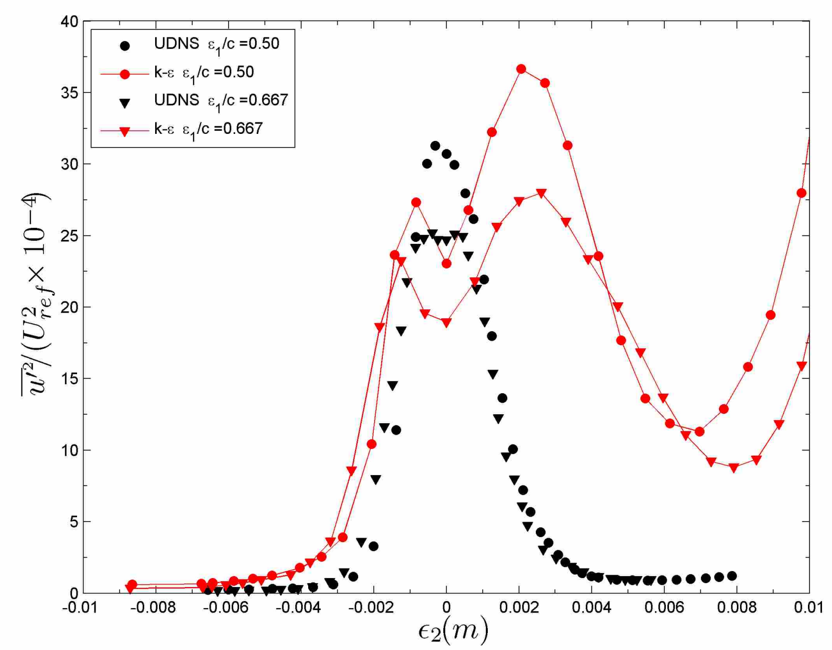

Figure 4.29: Comparison of $\overline{u'^2}$ from the UDNS and k-ε Data Sets

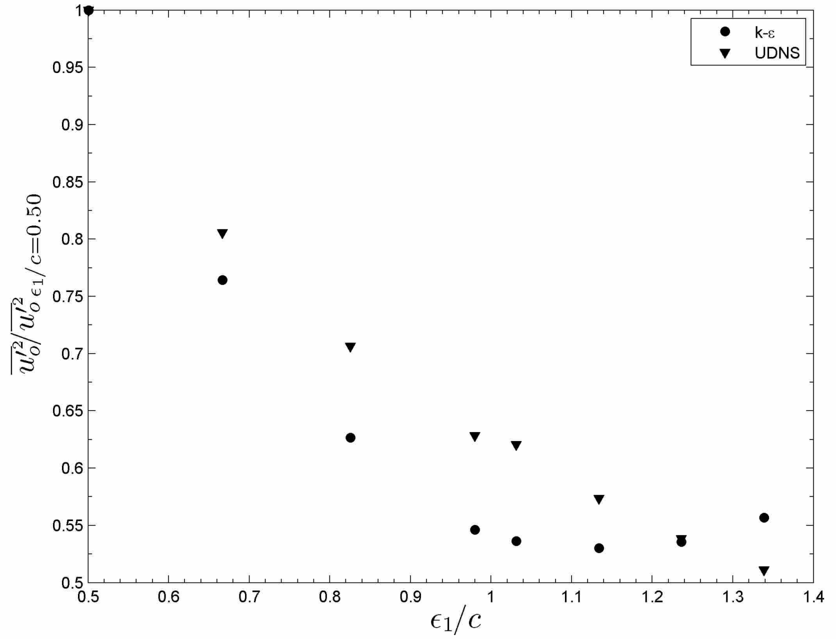

Figure 4.30: Peak Values of $\overline{u'^2}$, Normalized by Their Value at ε_1/c = 0.50 from the UDNS and k-ε Data Sets

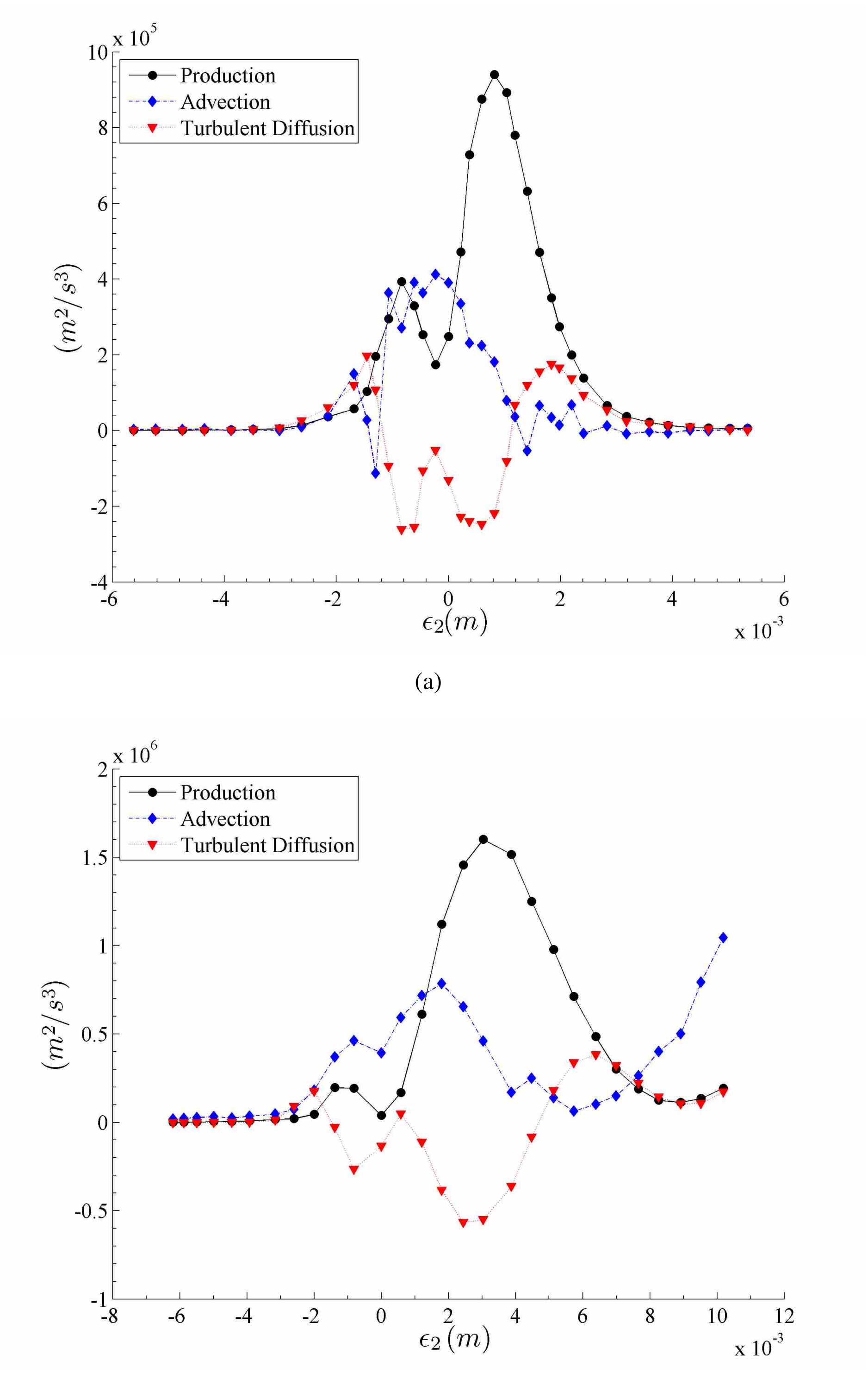

(a)

(b)

Figure 4.31: Terms from the Transport Equation for $\overline{u'^2}$ for (a) the UDNS and (b) the k-ε Data Sets at ε_1/c = 0.667

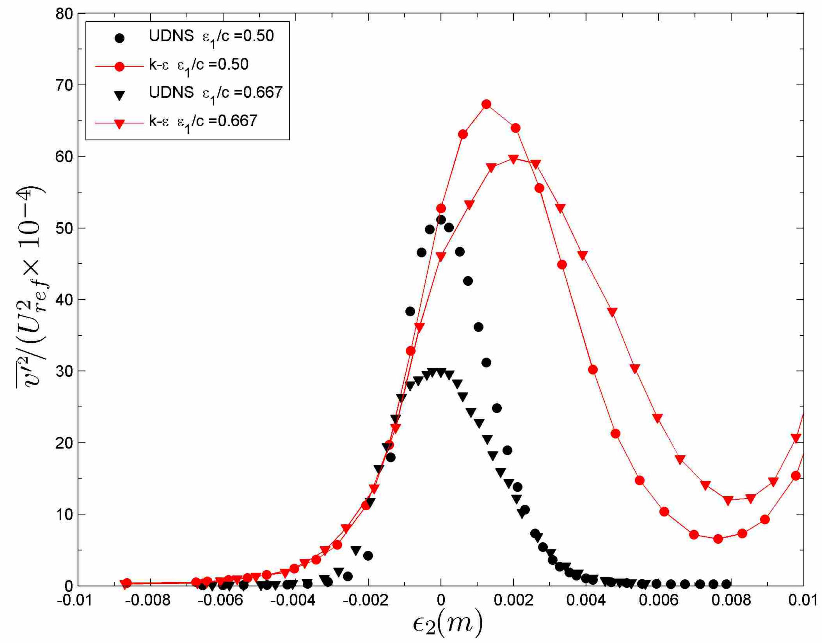

Figure 4.32: Comparison of $\overline{v'^2}$ from the UDNS and k-ε Data Sets

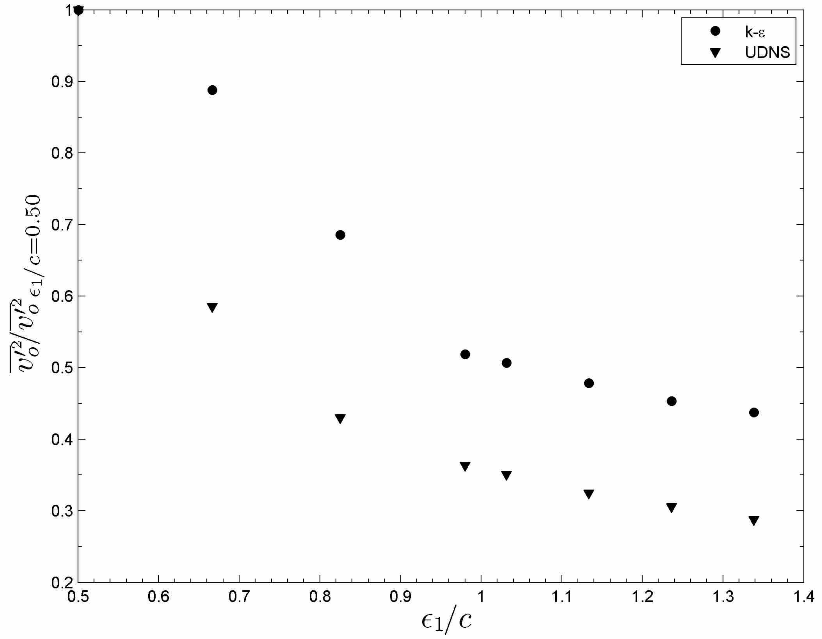

Figure 4.33: Peak Values of $\overline{v'^2}$, Normalized by Their Value at ε_1/c = 0.50 from the UDNS and k-ε Data Sets

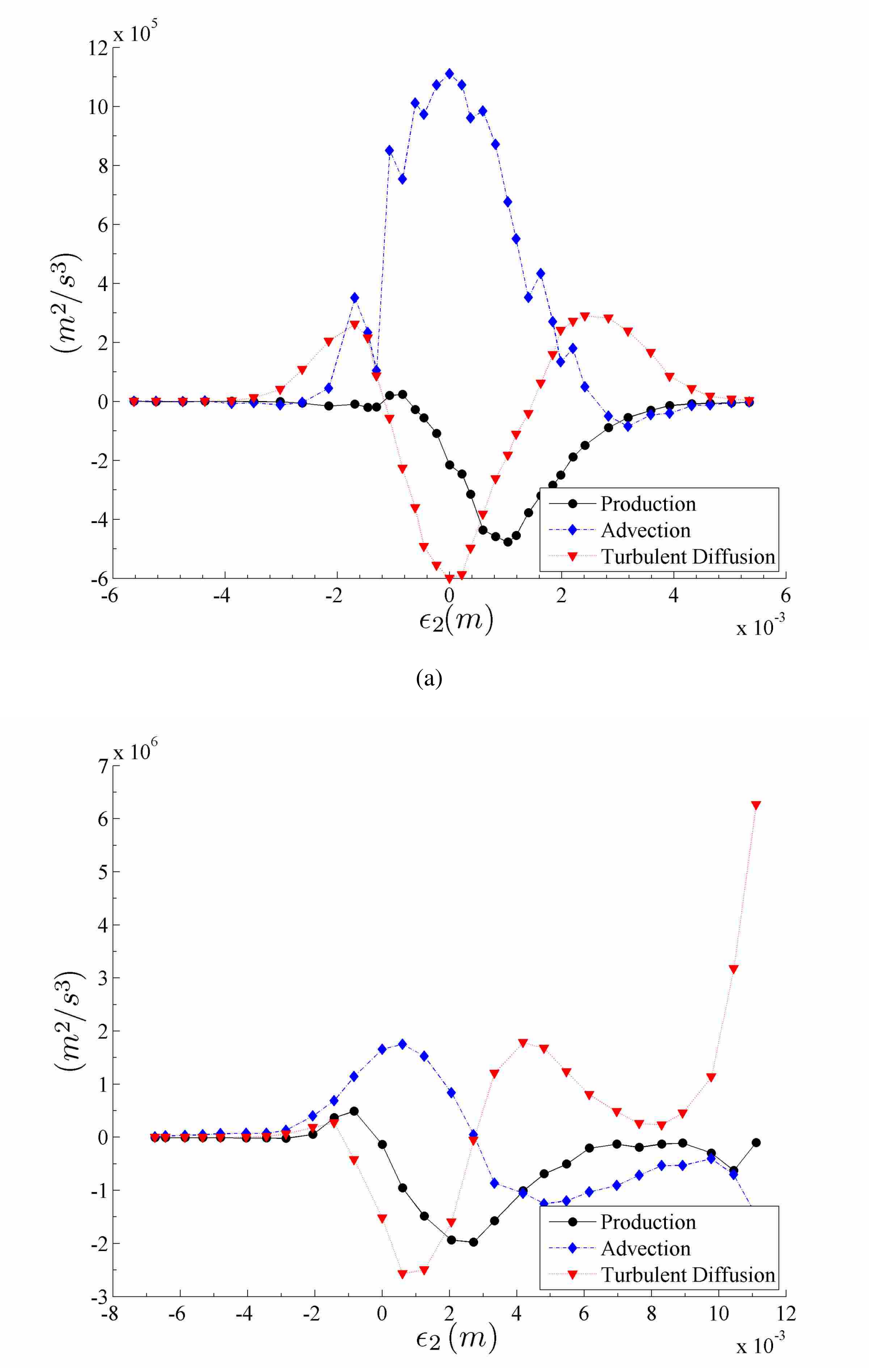

(a)

(b)

Figure 4.34: Terms from the Transport Equation for $\overline{v'^2}$ for (a) the UDNS and (b) the k-ε Data Sets at ε_1/c = 0.667

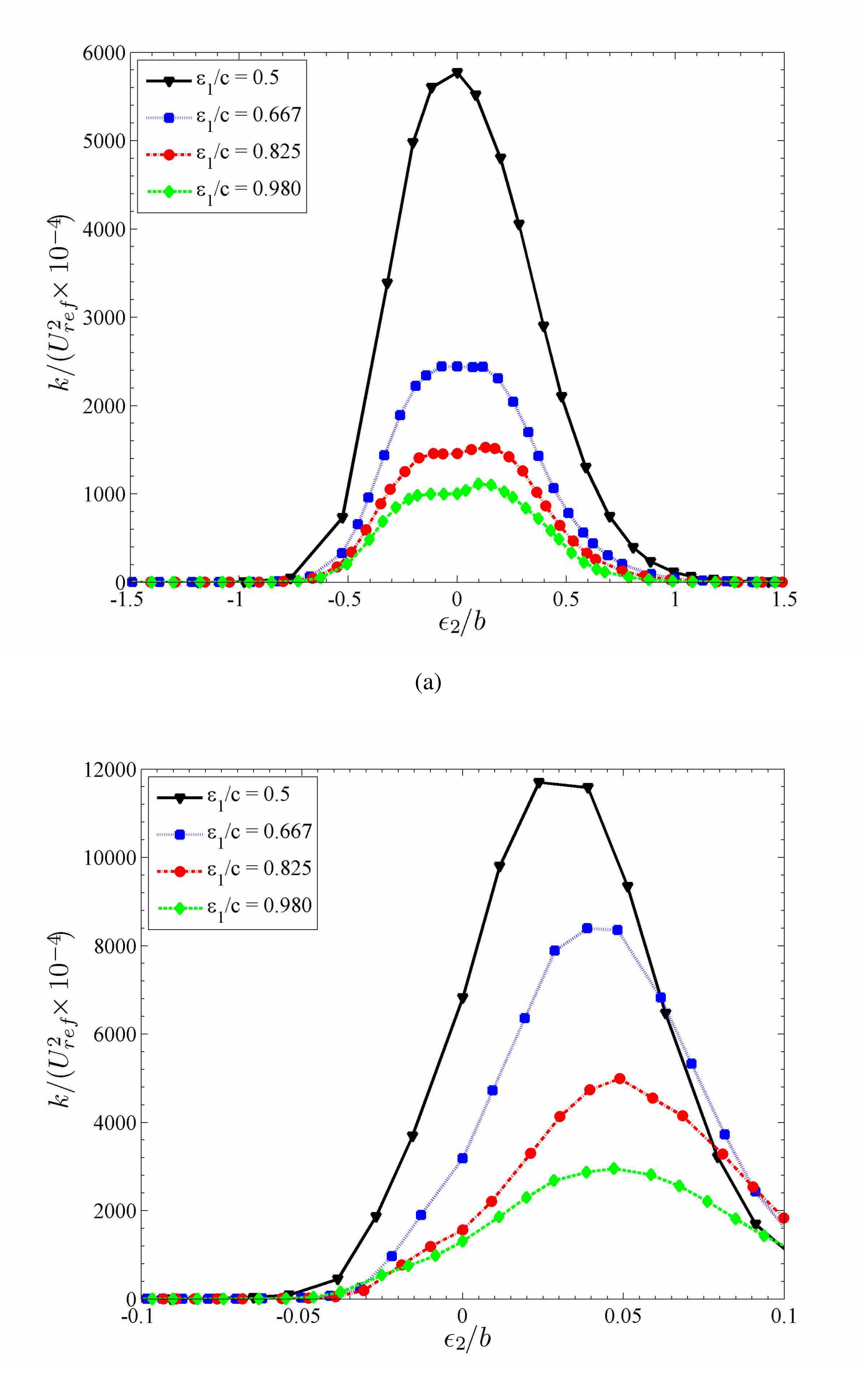

(a)

(b)

Figure 4.35: Lateral Distribution of the Turbulence Kinetic Energy, Normalized by the Reference Velocity, from (a) the UDNS and (b) the k-ε Data Sets

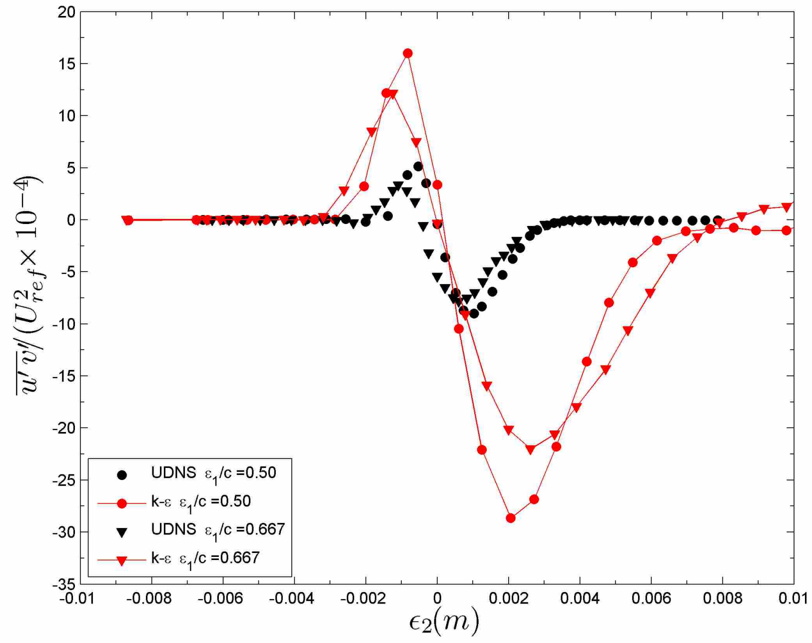

Figure 4.36: Profiles of $\overline{u'v'}$ at ε_1/c = 0.667 from the UDNS and k-ε Data Sets

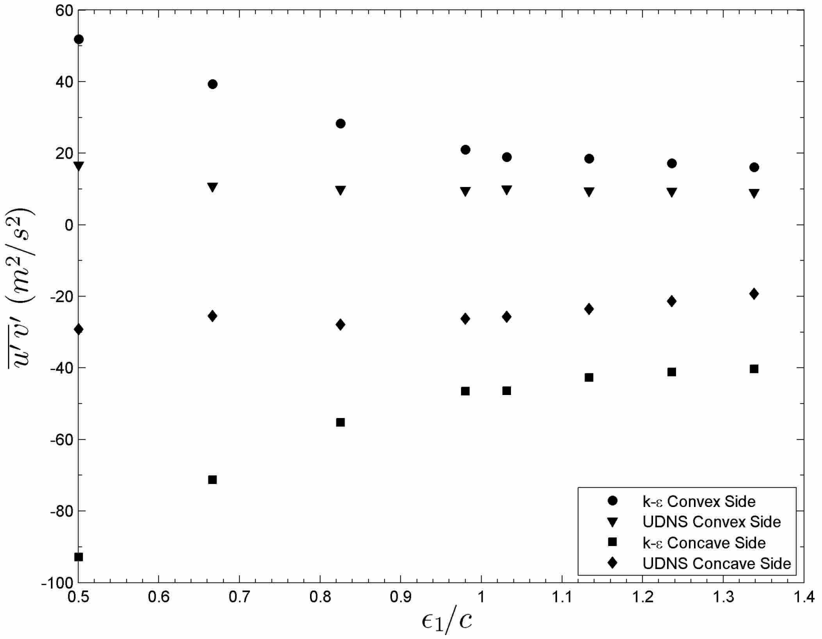

Figure 4.37: Comparison of the Reynolds Shear Stresses from the UDNS and k-ε Data Sets

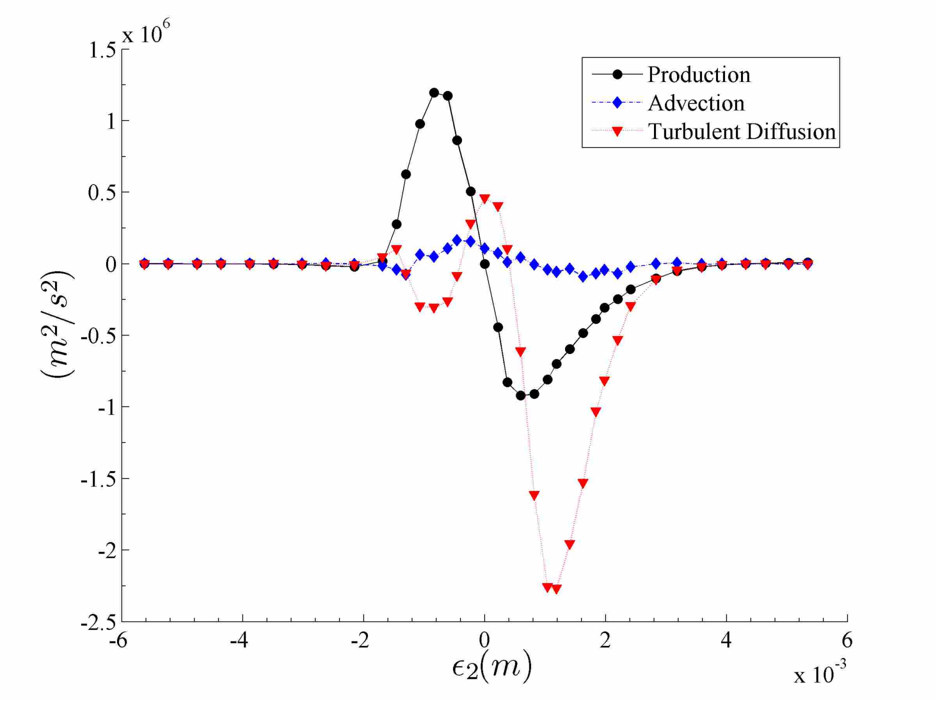

(a)

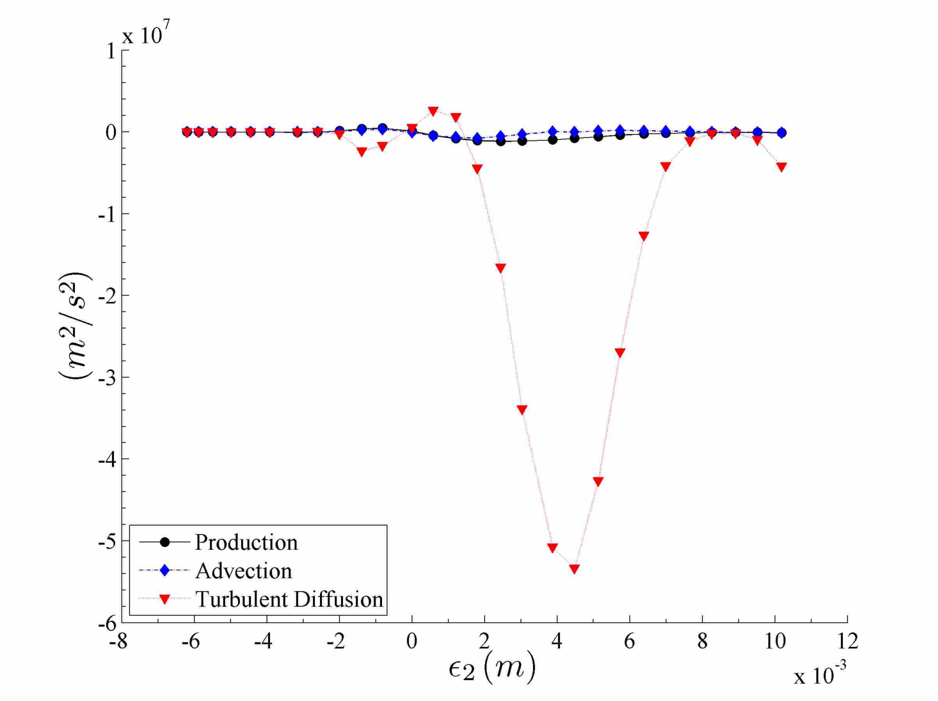

(b)

Figure 4.38: Terms from the Transport Equation for $\overline{u'v'}$ for (a) the UDNS and (b) the k-ε Data Sets at ε_1/c = 0.667

CHAPTER 5. CONCLUSIONS

An under-resolved direct numerical simulation was created to analyze the evolution of a transonic wake as it propagates through an adverse pressure gradient and streamline curvature. By calculating the ratio of $\Delta x/\eta$ it was determined that the simulation was 25 to 70 times too coarse to be considered fully resolved. This is higher fidelity than previous UDNS studies that have successfully calculated freestream properties as well as pressure profiles on blade surface using grids that were 60 to 80 times too coarse. Time averaged quantities such as mean velocity defect and wake width were calculated. The components of the Reynolds stress tensor and turbulence kinetic energy were also considered. These parameters were calculated at eight streamwise positions varying from $\varepsilon_1/c = 0.50$ to 1.334.

An asymmetry in the profiles of time-average velocity was observed with a larger wake width on the concave side of the wake. This asymmetry is possibly due to curvature as well as to the cambered airfoil that generated the wake. With the data extracted, a determination as to what effect each had was impossible. A review of the profiles of the mean velocity defect in similarity variables demonstrate that the wake width is twice as large on the concave side as it is on the convex side. Additionally, the plot of velocity defect in similarity variables show that similarity exists between all eight rake locations.

A transition in the dominant source of turbulence was observed as the turbulence created in the separated boundary layer on the wake generator dissipated, leaving shear production as the primary source of turbulence kinetic energy. At $\varepsilon_1/c = 0.50$ the magnitude of $\overline{v'^2}$ was observed to be double that of $\overline{u'^2}$ indicating the source of turbulence was the separated boundary layer at the trailing edge of the wake generator. This streamwise location was also characterized by large advection and turbulent diffusion terms for the normal Reynolds stress that dwarf the production term. This too indicates that the turbulence being transported in the wake at this streamwise location is not locally produced. Due to the large advection and diffusion terms this turbulence was transported away from the wake. The effects of shear production and curvature then became the driving force behind the wake profile evolution. In the region where shear production was dominant an asymmetric two-peak distribution $\overline{u'^2}$ was the result of a shear dominated production term. The effects of curvature on the asymmetry in the profiles of $\overline{u'^2}$ were observed to be only 20% of those of shear. This differs from the work seen in low speed curved wakes where the source of asymmetry in the turbulent stresses were curvature related production terms. In the region where shear production, and hence curvature, was dominant the peak streamwise normal Reynolds stress and shear stress occurred at the same value of ε_2/b as reported in the studies of an incompressible curved wake behind a cylinder.

The peak tangential Reynolds stress was originally located at the wake center but diverged from incompressible data behind a cylinder by then transitioning to be located close to the wake center on the convex side. Large advection and turbulent diffusion terms quickly decreased the levels of $\overline{v'^2}$ that originated from the wake generator. The shift in location of the peak was determined to be the direct result of positive production near the wake centerline on the convex side and a larger negative production term on the concave side. The production of $\overline{v'^2}$ was driven by curvature effects.

The differences between incompressible and transonic curved wakeflow reside mainly in the location and source of the asymmetry in the Reynolds stresses. In incompressible data the asymmetry in Reynolds stresses arise from new curvature related production terms. In the streamwise Reynolds stress the asymmetry is driven by a shear term in the production. The asymmetry in the shear and tangential stresses is driven by curvature dominated diffusion and production terms. Other compressible flow phenomena were present, the shock wave on the suction side of the second blade row, but were observed to affect the wake only indirectly.

An asymmetry similar to those observed in previous curved wake studies was observed in the Reynolds shear stresses. The magnitude of the peak stresses on the concave side of the wake was determined to be consistently twice that of the peak value on the convex side. This asymmetry in shear stresses is directly linked to the asymmetry observed in the wake width. In previous wake studies, the asymmetry in the Reynolds stresses was the result of new production terms created by curvature with the peak shear stress on the concave side was the result of production. On the concave side in UDNS however, the peak value was observed to be primarily the result of a large negative turbulent diffusion term. This diffusion term is driven by curvature related terms.

In previous wake research, the effects of curvature have been studied behind symmetric geometries. However, curved wakes behind asymmetric geometries, cambered airfoils in particular, have not been explored. This study fills that void in the body of literature. The closest low-speed comparison data set is a curved wake behind a cylinder [1]. The differences enumerated below could be due to the transonic nature of the flow or to the asymmetric geometry used for the wake generator. Greater asymmetry, measured by the ratio of the peak value and the centerline value, was observed in the streamwise Reynolds stresses presented here (1.34 vs. 1.1) than in the comparison data set. The tangential Reynolds stresses however demonstrated less asymmetry (1.04 vs. 1.23) than the low-speed data set [1]. The trend of less asymmetry in the tangential stresses than in the streamwise stresses was observed in the current data set. This trend is opposite of what is presented in the low-speed curved wake behind a cylinder. Additionally, the peak in the tangential Reynolds stresses shifts from the centerline to be located slightly on the convex side. The peak in the same stresses for the comparison low-speed set shifts from the centerline to the location of maximum shear on the concave side [1]. In low-speed wake research the asymmetry in the Reynolds stresses resulted from new curvature related production terms. In the current data set such is the case for $\overline{v'^2}$. The streamwise stresses, $\overline{u'^2}$, however are driven by shear related production and $\overline{u'v'}$ is driven by curvature related diffusion. These differences begin to illustrate the difference in transonic versus low-speed curved wake flow.

Wakes behind cambered airfoils are common in many engineering applications. It is therefore of worth for designers to know how far downstream the effects of the cambered airfoil are still altering the wake structure. Using a NACA 0065 thickness distribution, it was observed that the various components of the Reynolds stress tensor overcame the effects of the airfoil at difference streamwise distances. Production terms in the normal stresses, $\overline{u'^2}$ and $\overline{v'^2}$, became dominant by three-quarters of a chord length downstream. As the shear stresses are the most sensitive to the effects of curvature, the effects of the airfoil did not extend past two-thirds of a chord length.

A Reynolds averaged Navier-Stokes simulation was also created, using a version of the k-ε turbulence model that had been modified for turbomachinery flows, for comparison to the results of the UDNS to illustrate the behavior of that turbulence model in modeling transonic curved shear flow. It was observed that the k-ε turbulence model produces as wider wake with a smaller velocity defect than the UDNS. This increase in wake width was primarily located on the concave side of the wake. The width of the convex side was observed to be similar between the two data sets. The convex side of both sets was also observed to follow a similar trajectory. The k-ε model was observed to overpredict the effects of curvature on the Reynolds stresses resulting in increased magnitudes and in the case of the normal stresses increased asymmetry. The result of the higher levels and increased asymmetry in some stresses was the increased transport of momentum into the wake especially on the concave side. This was manifest in the lower velocity defect and a lack of a clear wake edge on the concave side of the wake in the k-ε data set.

The ratio of peak levels in the tangential normal stresses to the streamwise normal stresses were over predicted by the turbulence model. The levels of $\overline{u'^2}$ predicted by the k-ε model were observed to decay slightly faster than that from the UDNS. As a result the transition in sources of turbulence seen in the data from the UDNS was not observed in the data from the k-ε turbulence model. This indicates that the streamwise distance from the wake generator at which the effects of the cambered airfoil no longer dominate the wake structure is underpredicted by the k-ε turbulence model. The tangential turbulence intensity from the k-ε data set decays at a slower rate than that of the UDNS. As a result, the tangential intensity dominates the calculation of the turbulence kinetic energy. In this way the turbulence model predicts a turbulent structure of the wake that is significantly different from that calculated using UDNS.

The performance of several variants of the k-ε turbulence model on a low-speed curved wake behind a symmetric airfoil has been investigated [2]. The current study expands this knowledge by comparing a transonic curved wake behind a cambered airfoil with this previous data set. Both data sets show that the k-ε model overpredicts the asymmetry in the streamwise stresses. The current study went further however and showed that this is due to the model's overprediction of the effects of curvature on production of this stress. The tangential stresses, however, posed a more significant challenge for the transonic flow behind a cambered airfoil than they did in the low-speed flow around a symmetric airfoil. The transonic k-ε data showed that theses stresses dominated the turbulence kinetic energy whereas the low-speed data set showed TKE being driven by the streamwise stresses (a condition that is supported by the current UDNS data set). The designers of turbulence models can use this information and that above to improve the k-ε model for transonic wake flows.

5.1 Future Work

The work presented in this thesis provide a base for further exploration of several aspects of transonic curved wakes. The first aspect is the quantification of the effect of dissipation of Reynolds stresses (see Equation 5.1). In order to accomplish this, it is necessary to extract time trace data from the four neighboring nodes in the grid for each node where wake data was taken. The second is to evaluate the impact of the radial terms in the transport equations of the Reynolds stresses. Both of these aspects require the extraction of more data from the UDNS data set. A contribution of this work is the data describing Reynolds stress evolution for transonic flow past a cambered airfoil, since Reynolds stress data was previously available for low-speed curved wakes behind a cylinder. Since the comparison of the current body of data and the data previously available entails the combination of a large variety of factors. An effort therefore could be made to separate some of these factors. One way to do this would be to recreate the geometry of previous studies and vary only the Mach number of the flow. This would separate the effects of compressibility from everything else. In terms of the comparison of UDNS data and that from the k-ε model, the profiles of dissipation can be plotted and compared to UDNS data to determine how accurately the k-ε turbulence model captures the transport equation of dissipation. This would give further valuable insight to turbulence model designers in order to improve the model.

$$\varepsilon_{ij} = 2\nu \overline{\left(\frac{\partial u_i}{\partial x_k} \frac{\partial u_j}{\partial x_k} \right)} \tag{5.1}$$

REFERENCES

[1] Schobeiri, M., and John, J., 1996. "Development of a two-dimensional turbulent wake in a curved channel with a positive streamwise pressure gradient." *Transactions of the American Society of Mechanical Engineers,* **118**(2), pp. 292–299. vi, 2, 5, 6, 8, 9, 27, 38, 42, 43, 48, 52, 59, 62, 89

[2] Tulapurkara, E., Ramjee, V., and George, J., 1996. "Prediction of aerofoil wake subjected to the effects of curvature and pressure gradient." *International Journal for Numerical Methods in Fluids,* **22**, pp. 29–41. vi, 2, 6, 11, 38, 52, 59, 70, 72, 73, 90

[3] Gross, A., and Fasel, H., 2006. "Strategies for simulating flow through low-pressure turbine cascade." *Journal of Fluids EngineeringInternational Journal of Rotating Machinery,* **130**. vi, 19, 20

[4] Hill, P., Schaub, U., and Senoo, Y., 1963. "Turbulent wakes in pressure gradients." *Journal of Fluid Mechanics,* **30**(12), pp. 518–524. 2, 5

[5] Nakayama, A., 1986. "Curvature and pressure-gradient effects on a small-defect wake." *Journal of Fluid Mechanics,* **175**, pp. 215–246. 2, 6, 7, 38, 42, 52, 55

[6] Driver, D. M., and Mateer, G. G., 2002. "Wake Flow in Adverse Pressure Gradient." *International Journal of Heat and Fluid Flow,* **23**, pp. 564–571. 5

[7] Schobeiri, M., 2008. "Influence of curvatureand pressure gradient on turbulent wake development in curved channels." *Journal of Fluid Engineering,* **130**. 6, 7, 38

[8] Nichols, R. Turbulence models ans their application to complex flows. 9, 10, 30

[9] Wilcox, D., 2006. *Turbulence Modeling for CFD*. DCW Industries, Inc., La Canada, California. 9, 10, 18, 22, 23

[10] Raj, R., and Lakshminarayana, B., 1973. "Characteristics of the wake behind a cascade of airfoils." *Journal of Fluid Mechanics,* **61**(4), pp. 707–730. 11, 38, 42

[11] Zhang, Q., and Ligrani, P., 2008. "Wake turbulence structure downstream of a cambered airfoil in transonic flow: Effects of surface roughness and freestream turbulence intensity." *International Journal of Rotating Machinery,* **2008**. 12, 38, 40, 42

[12] List, M., 2007. "Quarter annulus simulations of blade row interaction at several gaps and discussion of flow physics." Master of science, University of Cincinnatti. 15, 24

[13] Beach, T., Turner, M., Kamp, M., and Nimersheim, J., 2007. "A turbomachinery gridding system." No. AIAA 2007-18, American Institute of Aeronoautics and Astronautics. 16

[14] Memory, C., Gompertz, K., Chen, J., and Bons, J., 2010. Numerical simulations of vortex generating jets on low pressure turbine blades 48 th AIAA Aerospace Sciences Meeting Including the New Horizons Forum and Aerospace Exposition, January. 19

[15] Michelassi, V., Wissink, R., and Rodi, W., 2002. "Analysis of dns and les of flow in a low pressure turbine cascade with incoming wakes and comparison with experiments." *Flow, Turbulence, and Combustion,* **69**, pp. 295–330. 19

[16] Kalitzin, G., Wu, X., and Durbin, P., 2003. "Dns of fully turbulent flow in a lpt passage." *International Journal of Heat and Fluid Flow,* **24**(4), pp. 636–644. 19

[17] Zaki, T., Durbin, P., Wissink, J., and Rodi, W., 2006. "Direct numerical simulation of by-pass and separation-induced transition in a linear compressor cascade." *Proceedings of GT2006 ASME Turbo Expo 2006: Power for Land, Sea, and Air*(GT2006-90885). 19

[18] Chen, J. P., and Briley, W. R., 2001. "A Parallel Flow Solver for Unsteady Multiple Blade Row Turbomachinery Simulations." ASME Paper 2001-GT-348. 21

[19] Memory, C., 2010. "Turbulent transition behavior in a separated and attached-flow low pressure turbine passage." Doctor of philosophy, The Ohio State University. 21

[20] Frenkiel, N., and Klebanoff, P., 1971. "Statistical properties of velocity derivatives in a turbulent field." *Journal of Fluid Mechanics,* **48**, pp. 183–208. 22

[21] Shabbir, A., Zhu, J., and Celestina, M., 1996. "Assessment of Three Turbulence Models in a Compressor Rotor." *Proceedings og the SME/IGTI Conferencel.* 25

[22] Soranna, F., Chow, Y., Uzol, O., and Katz, J., 2008. "Turbulence Within a Turbomachine Rotor Wake Subject to Nonuniform Contraction." *AIAA Journal,* **46**, pp. 2687–2702. 32, 42

APPENDIX A. TGS INPUT FILE FOR UDNS (DEFAULT DATA)

```
%\section{D} \label{sec:appendixa_figure_example}

//&&&&&&&&&&&&&&&&&&&&&&&&&&&&&&&&&&&&&&&&&&&&&&&&&&&&&&&&&&&&&&&&//
// Swirler and Deswirler
//&&&&&&&&&&&&&&&&&&&&&&&&&&&&&&&&&&&&&&&&&&&&&&&&&&&&&&&&&&&&&&&&//
/ Defaults file
/ Last updated: 22 May 2009

#DEFINE REFL 1.0
#define RGAS 53.348999
#define HREF 116441.500000
#define PREF 27.637011
#define TREF 625.945923
#define GAMMATABLE 1.399230,1.394644
#define TEMPTABLE 625.945923,746.244202
#DEFINE REFD 39.370000

#DEFINE TOLERANCE 0.000001
#DEFINE TOLERANCE2 0.000001

/////////////////////////////////////////////////////
/ Flowpath data files
/////////////////////////////////////////////////////
```

```
#define HUBFILE ../../geometry/hub.dat
#define CASEFILE ../../geometry/case.dat
#define INFILE ../../geometry/in.dat
#define OUTFILE ../../geometry/out_3row.dat
#define OUTFILE2 ../../geometry/out.dat
#define DRGAPLE ../../geometry/in_drgaple.dat
#define DRGAPTE ../../geometry/in_drgapte.dat
#define DRINTRFR ../../geometry/dr_intr_far.dat
#define DRINTRMD ../../geometry/dr_intr_mid.dat
#define INSWINTRCL ../../geometry/inletswrl_intr_close.dat
#define INSWINTRFR ../../geometry/inletswrl_intr_far.dat
#define INSWINTRMD ../../geometry/inletswrl_intr_mid.dat


/////////////////////////////////////////////////////
/ Clearance and geometry information
/////////////////////////////////////////////////////

/***  Data for Blade 1

#define BLADE1FILECL ../../geometry/clo/blade1_clo_80p_0.0s.dat
#define BLADE1FILEMD ../../geometry/mid/blade1_mid_80p_0.0s.dat
#define BLADE1FILEFR ../../geometry/far/blade1_far_80p_0.0s.dat

#DEFINE HUBCELLS1 8
#DEFINE HUBCLEARANCE1 0.011
#DEFINE TIPCELLS1 16
#DEFINE TIPCLEARANCE1 0.01
#DEFINE BLADE1_COUNT 32
```

```
/***  Data for Blade 2

#define BLADE2FILECL ../../geometry/blade2_close.dat
#define BLADE2FILEMD ../../geometry/blade2_mid.dat
#define BLADE2FILEFR ../../geometry/blade2_far.dat

#DEFINE HUBCELLS2 8
#DEFINE HUBCLEARANCE2 0.008
#DEFINE TIPCELLS2 16
#DEFINE TIPCLEARANCE2 0.008
#DEFINE BLADE2_COUNT 32

/////////////////////////////////////////////////////////////////////
/ Default Parameters For Axisymmetric Grid
/////////////////////////////////////////////////////////////////////
#DEFINE PRECISION single

/ Defaults
#DEFINE DZ_HUB_IN -0.1
#DEFINE DZ_HUB_OUT -0.1
#DEFINE DR_HUB_IN 0.0008000
#DEFINE DR_HUB_OUT 0.0008000
#DEFINE DZ_TIP_IN -0.1
#DEFINE DZ_TIP_OUT -0.1
#DEFINE DR_TIP_IN 0.0008000
#DEFINE DR_TIP_OUT 0.0008000
/ Block Fore of blade1
#DEFINE DZ_HUB_IN1 -0.2
#DEFINE DZ_HUB_OUT1 -0.1
```

```
#DEFINE DR_HUB_IN1 0.0010000

#DEFINE DR_HUB_OUT1 0.0010000

#DEFINE DZ_TIP_IN1 -0.2

#DEFINE DZ_TIP_OUT1 -0.1

#DEFINE DR_TIP_IN1 0.0008000

#DEFINE DR_TIP_OUT1 0.0004000


/ Blades 1 and 2

#DEFINE DZ_HUB_IN2 -0.1

#DEFINE DZ_HUB_OUT2 -0.1

#DEFINE DR_HUB_IN2 0.0010000

#DEFINE DR_HUB_OUT2 0.0007000

#DEFINE DZ_TIP_IN2 -0.1

#DEFINE DZ_TIP_OUT2 -0.1

#DEFINE DR_TIP_IN2 0.0004000

#DEFINE DR_TIP_OUT2 0.0002000


/ Block Aft of blade2

#DEFINE DZ_HUB_IN3 -0.05

#DEFINE DZ_HUB_OUT3 -0.05

#DEFINE DR_HUB_IN3 0.0007000

#DEFINE DR_HUB_OUT3 0.000700

#DEFINE DZ_TIP_IN3 -0.05

#DEFINE DZ_TIP_OUT3 -0.05

#DEFINE DR_TIP_IN3 0.0002000

#DEFINE DR_TIP_OUT3 0.00020000



#DEFINE DR_LE 0.002000

#DEFINE DR_TE 0.002000
```

```
#DEFINE NX_I 24

#DEFINE MNXG1 0

#DEFINE MDXG1 2.000000

#DEFINE MARCG1 0.000000


/========================================================================/

/    Swirler and Deswirler parameters

/========================================================================/

#DEFINE NX_INLETCLS 100

#DEFINE NX_INLETMID 70

#DEFINE NX_INLETFAR 375

#DEFINE NX_DROUTMID 100

#DEFINE NX_DROUTFAR 300

1-farspacing


/***   Axi Data for Blade 1


#DEFINE NX_I1 35

#DEFINE NX_B1 40

#DEFINE NX_G1 20

#DEFINE DS_LE_AXI1 0.002000

#DEFINE DS_TE_AXI1 0.002000

#DEFINE OFFSET11 0

#DEFINE OFFSETR11 0.0

#DEFINE OFFSET21 0

#DEFINE OFFSETR21 0.0

#DEFINE ROOFTOP1 0

#DEFINE ROOFSIZE1 0.000000

#DEFINE MNXG2 0

#DEFINE MDXG2 2.000000
```

```
#DEFINE MARCG2 0.500000

/***   Axi Data for Blade 2

#DEFINE NX_B2 40
#DEFINE NX_G2 20
#DEFINE DS_LE_AXI2 0.002000
#DEFINE DS_TE_AXI2 0.002000
#DEFINE OFFSET12 0
#DEFINE OFFSETR12 0.0
#DEFINE OFFSET22 0
#DEFINE OFFSETR22 0.0
#DEFINE ROOFTOP2 0
#DEFINE ROOFSIZE2 0.000000
#DEFINE MNXG3 0
#DEFINE MDXG3 2.000000
#DEFINE MARCG3 0.660000

#define NX_GAP 5

#DEFINE NSPAN 200
#DEFINE NX_O 20



///////////////////////////////////////////////////////////////
/ Default Parameters For 3D Grid
///////////////////////////////////////////////////////////////
/ This section contains variable declarations that are used to generate
/ the 3-D grid.
```

```
/***   Data for Blade 1

#DEFINE DS_LE1 0.001000
#DEFINE DS_TE1 0.000500
#DEFINE BLADE_POINTS1 700
#DEFINE DSIN1 0.0150000
#DEFINE DSOUT1 0.0050
#DEFINE DTIN1 0.000250
#DEFINE DTOUT1 0.000500

#DEFINE WALLSPACING1 0.10000
#DEFINE SPANWISE_3D1 1,11,26,46,56,76,95,116,135,151,165,
                     180,201,221,235,250,265,280,301
#DEFINE CELLS_THETA1 976

#DEFINE NFRONT1 125
#DEFINE NBACK1 150
#DEFINE LEADING_EDGE_POINTS1 20
#DEFINE TRAILING_EDGE_POINTS1 20

#DEFINE TIPCELLS1 16
#DEFINE HUBCELLS1 8
#DEFINE ROOFTOP1 0
#DEFINE ROOFSIZE1 0.000000

#DEFINE A_GRAPE1 0.600000
#DEFINE B_GRAPE1 0.600000
#DEFINE C_GRAPE1 0.600000
#DEFINE D_GRAPE1 0.600000
```

```
#DEFINE DMLE1 0.500000
#DEFINE DMTE1 0.500000
#DEFINE LEOFFSET1 0.050000
#DEFINE TEOFFSET1 0.100000

#DEFINE USE_YPLUS1 NO
#DEFINE CAFDBL1 ../outFile
#DEFINE YPLUS1 30.000000
#DEFINE YPLUSCHORD1 0.3 0.3
#DEFINE YPLUSSPAN1 0.0 1.0

/***   Data for Blade 2

#DEFINE DS_LE2 0.000400
#DEFINE DS_TE2 0.000400
#DEFINE BLADE_POINTS2 1000
#DEFINE DSIN2 0.010000
#DEFINE DSOUT2 0.00750
#DEFINE DTIN2 0.0003500
#DEFINE DTOUT2 0.00035000
#DEFINE WALLSPACING2 0.10000
#DEFINE SPANWISE_3D2 1,11,26,46,56,76,95,116,135,151,165,
                     180,201,221,235,250,265,280,301
#DEFINE CELLS_THETA2 800
#DEFINE NFRONT2 150
#DEFINE NBACK2 150
/#DEFINE NBACK2 125
#DEFINE LEADING_EDGE_POINTS2 15
#DEFINE TRAILING_EDGE_POINTS2 15
```

```
#DEFINE TIPCELLS2 16

#DEFINE HUBCELLS2 8

#DEFINE ROOFTOP2 0

#DEFINE ROOFSIZE2 0.000000

#DEFINE A_GRAPE2 0.600000

#DEFINE B_GRAPE2 0.600000

#DEFINE C_GRAPE2 0.600000

#DEFINE D_GRAPE2 0.600000

#DEFINE DMLE2 0.250000

#DEFINE DMTE2 0.500000

#DEFINE LEOFFSET2 0.350000

#DEFINE TEOFFSET2 0.100000

#DEFINE USE_YPLUS2 NO

#DEFINE CAFDBL2 ../outFile

#DEFINE YPLUS2 30.000000

#DEFINE YPLUSCHORD2 0.3 0.3

#DEFINE YPLUSSPAN2 0.0 1.0
```

APPENDIX B. TGS INPUT FILE FOR URANS (DEFAULT DATA)

```
//&&&&&&&&&&&&&&&&&&&&&&&&&&&&&&&&&&&&&&&&&&&&&&&&&&&&&&&&&&&&&&&&//
// WAKE GENERATOR
//&&&&&&&&&&&&&&&&&&&&&&&&&&&&&&&&&&&&&&&&&&&&&&&&&&&&&&&&&&&&&&&&//
/ Defaults file
/ Last updated: 22 June 2007

#DEFINE REFL 1.0
#define RGAS 53.348999
#define HREF 116441.500000
#define PREF 27.637011
#define TREF 625.945923
#define GAMMATABLE 1.399230,1.394644
#define TEMPTABLE 625.945923,746.244202
#DEFINE REFD 39.370000
#DEFINE TOLERANCE 0.000001
#DEFINE TOLERANCE2 0.000001

/////////////////////////////////////////////////////
/ Flowpath data files
/////////////////////////////////////////////////////

#define HUBFILE ../../geometry/hub.dat
#define CASEFILE ../../geometry/case.dat
#define INFILE ../../geometry/in.dat
```

```
#define OUTFILE ../../geometry/out_3row.dat
#define OUTFILE2 ../../geometry/out.dat
#define DRGAPLE ../../geometry/in_drgaple.dat
#define DRGAPTE ../../geometry/in_drgapte.dat
#define DRINTRFR ../../geometry/dr_intr_far.dat
#define DRINTRMD ../../geometry/dr_intr_mid.dat
#define INSWINTRCL ../../geometry/inletswrl_intr_close.dat
#define INSWINTRFR ../../geometry/inletswrl_intr_far.dat
#define INSWINTRMD ../../geometry/inletswrl_intr_mid.dat

/////////////////////////////////////////////////////
/ Clearance and geometry information
/////////////////////////////////////////////////////

/***  Data for Blade 1

#define BLADE1FILECL ../../geometry/clo/blade1_clo_80p_-3.0s.dat
#define BLADE1FILEMD ../../geometry/mid/blade1_mid_80p_-3.0s.dat
#define BLADE1FILEFR ../../geometry/far/blade1_far_80p_1.5s.dat
#DEFINE HUBCELLS1 4
#DEFINE HUBCLEARANCE1 0.011
#DEFINE TIPCELLS1 8
#DEFINE TIPCLEARANCE1 0.01
#DEFINE BLADE1_COUNT 32

/***  Data for Blade 2

#define BLADE2FILECL ../../geometry/blade2_close.dat
#define BLADE2FILEMD ../../geometry/blade2_mid.dat
#define BLADE2FILEFR ../../geometry/blade2_far.dat
```

```
#DEFINE HUBCELLS2 4
#DEFINE HUBCLEARANCE2 0.008
#DEFINE TIPCELLS2 8
#DEFINE TIPCLEARANCE2 0.008
#DEFINE BLADE2_COUNT 32

//////////////////////////////////////////////////////////////////
/ Default Parameters For Axisymmetric Grid
//////////////////////////////////////////////////////////////////
#DEFINE PRECISION single

/ Defaults
#DEFINE DZ_HUB_IN -0.1
#DEFINE DZ_HUB_OUT -0.1
#DEFINE DR_HUB_IN 0.0008000
#DEFINE DR_HUB_OUT 0.0008000
#DEFINE DZ_TIP_IN -0.1
#DEFINE DZ_TIP_OUT -0.1
#DEFINE DR_TIP_IN 0.0008000
#DEFINE DR_TIP_OUT 0.0008000

/ Block Fore of blade1
#DEFINE DZ_HUB_IN1 -0.2
#DEFINE DZ_HUB_OUT1 -0.1
#DEFINE DR_HUB_IN1 0.0010000
#DEFINE DR_HUB_OUT1 0.0010000
#DEFINE DZ_TIP_IN1 -0.2
#DEFINE DZ_TIP_OUT1 -0.1
#DEFINE DR_TIP_IN1 0.0008000
```

```
#DEFINE DR_TIP_OUT1 0.0004000

/ Blades 1 and 2
#DEFINE DZ_HUB_IN2 -0.1
#DEFINE DZ_HUB_OUT2 -0.1
#DEFINE DR_HUB_IN2 0.0010000
#DEFINE DR_HUB_OUT2 0.0007000
#DEFINE DZ_TIP_IN2 -0.1
#DEFINE DZ_TIP_OUT2 -0.1
#DEFINE DR_TIP_IN2 0.0004000
#DEFINE DR_TIP_OUT2 0.0002000

/ Block Aft of blade2
#DEFINE DZ_HUB_IN3 -0.05
#DEFINE DZ_HUB_OUT3 -0.05
#DEFINE DR_HUB_IN3 0.0007000
#DEFINE DR_HUB_OUT3 0.000700
#DEFINE DZ_TIP_IN3 -0.05
#DEFINE DZ_TIP_OUT3 -0.05
#DEFINE DR_TIP_IN3 0.0002000
#DEFINE DR_TIP_OUT3 0.00020000

#DEFINE DR_LE 0.002000
#DEFINE DR_TE 0.002000
#DEFINE NX_I 24
#DEFINE MNXG1 0
#DEFINE MDXG1 2.000000
#DEFINE MARCG1 0.000000

/========================================================================/
```

```
/    Wake Generator parameters
/=======================================================================/

#DEFINE NX_INLETCLS 100
#DEFINE NX_INLETMID 70
#DEFINE NX_INLETFAR 40
#DEFINE NX_DROUTMID 100
#DEFINE NX_DROUTFAR 200

/***   Axi Data for Blade 1

#DEFINE NX_I1 35
#DEFINE NX_B1 40
#DEFINE NX_G1 20
#DEFINE DS_LE_AXI1 0.002000
#DEFINE DS_TE_AXI1 0.002000
#DEFINE OFFSET11 0
#DEFINE OFFSETR11 0.0
#DEFINE OFFSET21 0
#DEFINE OFFSETR21 0.0
#DEFINE ROOFTOP1 0
#DEFINE ROOFSIZE1 0.000000
#DEFINE MNXG2 0
#DEFINE MDXG2 2.000000
#DEFINE MARCG2 0.500000

/***   Axi Data for Blade 2

#DEFINE NX_B2 40
#DEFINE NX_G2 20
```

```
#DEFINE DS_LE_AXI2 0.002000

#DEFINE DS_TE_AXI2 0.002000

#DEFINE OFFSET12 0

#DEFINE OFFSETR12 0.0

#DEFINE OFFSET22 0

#DEFINE OFFSETR22 0.0

#DEFINE ROOFTOP2 0

#DEFINE ROOFSIZE2 0.000000

#DEFINE MNXG3 0

#DEFINE MDXG3 2.000000

#DEFINE MARCG3 0.660000

#define NX_GAP 5


#DEFINE NSPAN 100

#DEFINE NX_O 20




/////////////////////////////////////////////////////////////////

/ Default Parameters For 3D Grid

/////////////////////////////////////////////////////////////////

/ This section contains variable declarations that are used to generate

/ the 3-D grid.


/***   Data for Blade 1


#DEFINE DS_LE1 0.001000

#DEFINE DS_TE1 0.000500

#DEFINE BLADE_POINTS1 150

#DEFINE DSIN1 0.1400000
```

```
#DEFINE DSOUT1 0.04000
#DEFINE DTIN1 0.010000
#DEFINE DTOUT1 0.010000
#DEFINE WALLSPACING1 0.500000
#DEFINE SPANWISE_3D1 1,11,26,46,56,76,91,101
#DEFINE CELLS_THETA1 150
#DEFINE NFRONT1 32
#DEFINE NBACK1 40
#DEFINE LEADING_EDGE_POINTS1 40
#DEFINE TRAILING_EDGE_POINTS1 50
#DEFINE TIPCELLS1 8
#DEFINE HUBCELLS1 4
#DEFINE ROOFTOP1 0
#DEFINE ROOFSIZE1 0.000000
#DEFINE A_GRAPE1 0.600000
#DEFINE B_GRAPE1 0.600000
#DEFINE C_GRAPE1 0.600000
#DEFINE D_GRAPE1 0.600000
#DEFINE DMLE1 0.500000
#DEFINE DMTE1 0.500000
#DEFINE LEOFFSET1 0.050000
#DEFINE TEOFFSET1 0.100000
#DEFINE USE_YPLUS1 YES
#DEFINE CAFDBL1 ../outFile
#DEFINE YPLUS1 30.000000
#DEFINE YPLUSCHORD1 0.3 0.3
#DEFINE YPLUSSPAN1 0.0 1.0


/***   Data for Blade 2
```

```
#DEFINE DS_LE2 0.000400

#DEFINE DS_TE2 0.000400

#DEFINE BLADE_POINTS2 170

#DEFINE DSIN2 0.040000

#DEFINE DSOUT2 0.020000

#DEFINE DTIN2 0.010000

#DEFINE DTOUT2 0.005000

#DEFINE WALLSPACING2 0.500000

#DEFINE SPANWISE_3D2 1,11,26,46,56,76,91,101

#DEFINE CELLS_THETA2 200

#DEFINE NFRONT2 35

#DEFINE NBACK2 55

/#DEFINE NBACK2 50

#DEFINE LEADING_EDGE_POINTS2 50

#DEFINE TRAILING_EDGE_POINTS2 50


#DEFINE TIPCELLS2 8

#DEFINE HUBCELLS2 4

#DEFINE ROOFTOP2 0

#DEFINE ROOFSIZE2 0.000000


#DEFINE A_GRAPE2 0.600000

#DEFINE B_GRAPE2 0.600000

#DEFINE C_GRAPE2 0.600000

#DEFINE D_GRAPE2 0.600000


#DEFINE DMLE2 0.250000

#DEFINE DMTE2 0.500000

#DEFINE LEOFFSET2 0.350000
```

```
#DEFINE TEOFFSET2 0.100000


#DEFINE USE_YPLUS2 YES

#DEFINE CAFDBL2 ../outFile

#DEFINE YPLUS2 30.000000

#DEFINE YPLUSCHORD2 0.3 0.3

#DEFINE YPLUSSPAN2 0.0 1.0
```

APPENDIX C. PTURBO INPUT FILES FOR UDNS (INPUT00, INPUT01, INPUT02)

```
(input00)
&PARAMETERS
        num_blade_rows=2
        debug=F
        gofast=T/

 &SOLUTION_PARAMETERS
        num_printouts= 2
!       num_printouts= 42
        num_iter_per_printout=1100
!       num_iter_per_printout=160
        jacobian_update=1
        resid_print=1
        max_num_subiter=6
        min_residual=-1.2000
        num_iter_zero_grad_bc=0
        num_iter_first_order=0
        num_iter_infreq_jacobian_update=0
        num_iter_inviscid=0
        num_iter_without_fluxfix=0
        symmetry_factor=32
!       num_iter_restart_write=1100
        num_iter_restart_write=500
        slip_bc_type=1
```

```
       freeze_jacobian=0

       num_sgs_iter=3

       solution_type=1

       turbulence_model=5

       temporal_accuracy=2

       spatial_accuracy=3

       limiter_flag=1

       spatial_scheme=0

       wall_bc_limiter_flag=0

       wall_bc_first_order_i=1

       wall_bc_first_order_j=1

       wall_bc_first_order_k=1

       trap_negative=F

       solution_correct_method=2

       pressure_clip=0.02800000/


&SLIDING_BC

       use_conserve_bc=0/


&INITIAL_CONDITION

       initialize_solution=4

       freestream_mach_num=0.5300

       tangential_angle=0.0000

       radial_angle=0.0000

       thru_ic_flag =1/


&REFERENCE_CONDITIONS

       ref_pressure=101325.0000

       ref_temperature=288.1500

       ref_velocity=287.567
```

```
        ref_gamma=1.401290
        ref_length=1.0
        gamma_table=1.40129 1.40129
        temp_gam_table=288.15 388.15
        gamref_t1=1.40129
                !Mike's Thesis parameters
!       sutherland_const1=110.0000

 &ke_MODEL_PARAMETERS
        kemdl_input_type=0
        kemdl_init_option=0
        inlet_turbulence_intensity=0.0300
        inlet_eddy_viscosity=30.0000
        spatial_accuracy_2eq=3
        temporal_accuracy_2eq=2
        limiter_flag_2eq=1
        use_pgrad_term=F
        use_emut_wall_damping=T
        max_num_subiter_2eq=1
        jacobian_update_2eq=1
        num_sgs_iter_2eq=1
        cmu_clip_max=1.0000
        dmut_clip_max=1.0000/

 &TIME_SHIFT_BC
        use_time_shift_bc=0
        time_shift_bc_factor=0.500
        initialize_time_shift_in_TURBO=F/

 &INLET_BC
```

```
        inlet_bc_type=-2
        num_blade_us=0
        omega_blade_us=0.0000
        num_tangential_cells_us=1/

 &EXIT_BC
        exit_bc_type=24
        back_pressure=78186
!       back_pressure=113600
!        back_pressure=100000
        num_blade_ds=49
        omega_blade_ds=0.0
        num_tangential_cells_ds=1/

 &FLUTTER
        flutter_grid_type=0
        flutter_freq=0.0000
        flutter_phase_angle=0.0000/

 &TIME_STEP
        cfl=0.0000
        use_local_time_step=0
        num_time_steps_per_period=1100
!        omega_ts=-16405
        omega_ts=-16487.025
        num_blds_ts=28/

 &OUTPUT
        output_format=3
        num_iter_per_soln_dump=1
```

```
        num_soln_per_flow_file=1
        num_parallel_writes=500
!       num_parallel_writes=400
        itime_start_anim=65800
        tmavg_output=T/
!       tmavg_output=F/

 &INLET_PROFILE
         span = 0 0.05 0.25 0.5 0.75 0.95 1
         total_pressure = 86614.8 101325 101325
                          101325 101325 101325 87588.8
         total_temperature = 7*288.15
         tangential_angle = 7*0
         radial_angle = 7*0/

&EXIT_PROFILE
        span = 0.0 1.0
        static_pressure = 78187
!       static_pressure = 75000 75000
        exit_mass_flow = 15.35/
!       exit_mass_flow = 14.846/

(input01)
&BLADE_ROW_PARAMETERS
omega_bld = 0.0
num_blades = 32
suction_surface = 1
use_wall_func_i = 1
use_wall_func_j = 1
use_wall_func_k = 1
```

```
transition = 0.1
blade_row_ksym = 32
num_time_steps_stored = -1
num_adjacent_blades = 32
x_start_case_rotation   = 9999.
x_end_case_rotation     = 9999.
x_start_hub_rotation    = -9999.
x_end_hub_rotation      = -9999.
cut_plane_dir = 2
num_cut_plane = 1
cut_plane_global_posi = 98
```

(input02)

```
&BLADE_ROW_PARAMETERS
omega_bld = 0.0
num_blades = 32
suction_surface = 2
use_wall_func_i = 1
use_wall_func_j = 1
use_wall_func_k = 1
transition = 0.1
blade_row_ksym = 32
num_time_steps_stored = -1
num_adjacent_blades = 32
x_start_case_rotation   = 9999.
x_end_case_rotation     = 9999.
x_start_hub_rotation    = -9999.
x_end_hub_rotation      = -9999.
cut_plane_dir = 2
```

```
num_cut_plane = 1

cut_plane_global_posi = 98
```

APPENDIX D. PTURBO INPUT FILES FOR URANS (INPUT00, INPUT01, INPUT02)

(input00)

```
&PARAMETERS
        num_blade_rows=2
        debug=F
        gofast=T/

 &SOLUTION_PARAMETERS
        num_printouts=  4
!       num_printouts = 180
        num_iter_per_printout=180
!       num_iter_per_printout=160
        jacobian_update=1
        resid_print=1
        max_num_subiter=6
        min_residual=-1.2000
        num_iter_zero_grad_bc=0
        num_iter_first_order=0
        num_iter_infreq_jacobian_update=0
        num_iter_inviscid=0
        num_iter_without_fluxfix=0
        symmetry_factor=32
        num_iter_restart_write=360
!       num_iter_restart_write=1120
```

```
        slip_bc_type=1

        freeze_jacobian=0

        num_sgs_iter=3

        solution_type=2

        turbulence_model=5

        temporal_accuracy=2

        spatial_accuracy=3

        limiter_flag=1

        spatial_scheme=0

        wall_bc_limiter_flag=0

        wall_bc_first_order_i=1

        wall_bc_first_order_j=1

        wall_bc_first_order_k=1

        trap_negative=F

        solution_correct_method=2

        pressure_clip=0.02800000/


&SLIDING_BC

        use_conserve_bc=0/


&INITIAL_CONDITION

        initialize_solution=4

        freestream_mach_num=0.5300

        tangential_angle=0.0000

        radial_angle=0.0000

        thru_ic_flag =1/


&REFERENCE_CONDITIONS

        ref_pressure=101325.0000

        ref_temperature=288.1500
```

```
        ref_velocity=287.567
        ref_gamma=1.401290
        ref_length=1.0
        gamma_table=1.40129 1.40129
        temp_gam_table=288.15 388.15
        gamref_t1=1.40129
                !Mike’s Thesis parameters
!       sutherland_const1=110.0000
!       sutherland_const2=110.0000/

 &ke_MODEL_PARAMETERS
        kemdl_input_type=0
        kemdl_init_option=0
        inlet_turbulence_intensity=0.0300
        inlet_eddy_viscosity=30.0000
        spatial_accuracy_2eq=3
        temporal_accuracy_2eq=2
        limiter_flag_2eq=1
        use_pgrad_term=F
        use_emut_wall_damping=T
        max_num_subiter_2eq=1
        jacobian_update_2eq=1
        num_sgs_iter_2eq=1
        cmu_clip_max=1.0000
        dmut_clip_max=1.0000/

 &TIME_SHIFT_BC
        use_time_shift_bc=0
        time_shift_bc_factor=0.500
        initialize_time_shift_in_TURBO=F/
```

```
 &INLET_BC
        inlet_bc_type=-2
        num_blade_us=0
        omega_blade_us=0.0000
        num_tangential_cells_us=1/

 &EXIT_BC
        exit_bc_type=24
        back_pressure=78186
!       back_pressure=113600
!        back_pressure=100000
        num_blade_ds=49
        omega_blade_ds=0.0
        num_tangential_cells_ds=1/

 &FLUTTER
        flutter_grid_type=0
        flutter_freq=0.0000
        flutter_phase_angle=0.0000/

 &TIME_STEP
        cfl=0.0000
        use_local_time_step=0
        num_time_steps_per_period=180
!        omega_ts=-16405
        omega_ts=-16487.025
        num_blds_ts=28/

 &OUTPUT
```

```
        output_format=3
        num_iter_per_soln_dump=2
        num_soln_per_flow_file=1
        num_parallel_writes=300
!       num_parallel_writes=400
        itime_start_anim=102960
        tmavg_output=T/
!       tmavg_output=F/

 &INLET_PROFILE
         span = 0 0.05 0.25 0.5 0.75 0.95 1
         total_pressure = 86614.8 101325 101325
          101325 101325 101325 87588.8
         total_temperature = 7*288.15
         tangential_angle = 7*0
         radial_angle = 7*0/

&EXIT_PROFILE
        span = 0.0 1.0
        static_pressure = 78187
!       static_pressure = 75000 75000
        exit_mass_flow = 15.35/
!       exit_mass_flow = 14.846/



(input01)
&BLADE_ROW_PARAMETERS
omega_bld = 0.0
num_blades = 32
suction_surface = 1
```

```
use_wall_func_i = 1
use_wall_func_j = 1
use_wall_func_k = 1
transition = 0.1
blade_row_ksym = 32
num_time_steps_stored = -1
num_adjacent_blades = 32
x_start_case_rotation   = 9999.
x_end_case_rotation     = 9999.
x_start_hub_rotation    = -9999.
x_end_hub_rotation      = -9999.
cut_plane_dir = 2
num_cut_plane = 1
cut_plane_global_posi = 49

(input02)
&BLADE_ROW_PARAMETERS
omega_bld = 0.0
num_blades = 32
suction_surface = 2
use_wall_func_i = 1
use_wall_func_j = 1
use_wall_func_k = 1
transition = 0.1
blade_row_ksym = 32
num_time_steps_stored = -1
num_adjacent_blades = 32
x_start_case_rotation   = 9999.
x_end_case_rotation     = 9999.
x_start_hub_rotation    = -9999.
```

```
x_end_hub_rotation      = -9999.

cut_plane_dir = 2

num_cut_plane = 1

cut_plane_global_posi = 49
```